

Kinetic, thermodynamic, and structural transitions in order-disorder alloys and bulk metallic glass-forming alloys



Dissertation

zur Erlangung des Grades
Doktors der Naturwissenschaften (Dr. rer. nat.)

der
Naturwissenschaftlich-Technischen Fakultät III Chemie,
Pharmazie und Werkstoffwissenschaften

der
Universität des Saarlandes
Saarbrücken

vorgelegt von

Shuai Wei

February 2014

Tag des Kolloquiums: 29.09.2014

Dekan: Prof. Dr. V. Helms

Berichterstatter: Prof. Dr. R. Busch, Prof. Dr. F.

Mücklich and Prof. Dr. A. Meyer

Vorsitz: Prof. Dr. D. Bähre

Akad. Mitarbeiter: Dr. Dr. A. Jung

I dedicate this thesis to my loving parents...

Acknowledgements

First and foremost, I wish to express my sincerest gratitude to my Ph.D. supervisor Prof. Dr. Ralf Busch for his patience, invaluable guidance and encouragement throughout my Ph.D life. His wisdom, knowledge and insight motivate me and make my Ph.D. experience productive and enjoyable. He gives me the freedom to pursue my own research interests and is always supportive in many ways to achieve research aims. He is the best advisor I could have wished for.

I am very grateful to my great colleagues and friends at the Lehrstuhl für metallische Werkstoffe of Universität des Saarlandes. I would like to thank Dr. Isabella Gallino for her nice mentoring when I entered the lab, kindly support, sharing her expert knowledge on calorimetry and valuable discussions. I want to thank Dr. Zach Evenson for sharing his knowledge, valuable perspectives and discussions as well as nice proof-reading of my manuscripts. I sincerely thank my great office mate Moritz Stolpe. He is one of the smartest people I know. We had many inspiring, valuable and enjoyable talks on and beyond science. I am also thankful to him for helping me translate the abstract of the thesis into German and careful proof-reading my manuscripts. I would like to thank Dr. Jochen Heinrich for thoughtful advices and organizing many fun group activities. I also wish to acknowledge William Hembree for his kindness, always helpful discussions and careful proof-reading my thesis. I enjoyed a lot working together with him. I want to thank Dr. Sanja Stanojevic, Dr. Frank Aubertin, Lin Wang, Oliver Gross, Simon Hechler, Stefan Gärtner, Markus Kelkel, Benedikt Bochtler, Jörg Eiden, Hermann Altermeyer, Martina Stemmler and all else who contribute to create such a great workplace.

I would like to sincerely thank Prof. Dr. C. Austen Angell of Arizona State University for sharing his extensive knowledge and passion for research. He is one of my collaborators for my first research paper and inspires me. He makes an example to me of how a great scientist should be.

I would like to give special thanks to Prof. Dr. Andreas Meyer and Dr. Fan Yang at German Aerospace Center (DLR, Cologne) for their very productive and nice cooperation. I also want to thank Dr. Jozef Bednarcik at DESY (Hamburg), Dr. Ivan Kaban and Dr. Olga Shuleshova at IFW (Dresden) for their help with the synchrotron x-ray scattering experiments.

Many thanks go to Prof. Dr. Frank Mücklich and Dr. Flavio Soldera for my AMASE-Master scholarship program. Without their efforts, my graduate work in Saarbrücken would not have been possible. I acknowledge the financial support during my AMASE-master study provided by Erasmus Mundus Program of European Commission. I wish to thank my friend Joel Andersson for his kindly guidance and always inspiring discussions at Luleå University of Technology.

I would like to express my special thanks to Prof. Dr. Philippe Blanchard of Bielefeld University. He enabled me to make my first foreign country study in Germany as an exchange student at Bielefeld University in my Bachelor program. I want to thank Prof. Dr. Dominik J. Schwarz of Bielefeld University for his timely reference letter for my applications for master programs in Germany. Special thanks go to Dr. Li, Nan and Dr. Dr. Zou, Benteng for their kindly help in physics and mathematics during my stay in Bielefeld.

My deepest thanks go to my mother Li, Juling and my father Wei, Changping for their invaluable love and support. They always support me to make my own decisions and pursue my life goals at any place around the world no matter how far I am from my family.

I would like to thank all my friends in Saarbrücken, especially, Dr. Rui Wang for our fun discussions even on my research topic, and friends in other cities in Europe and in China. With their support and companion, my world is rich and full of love.

At last, I would like to thank my wife Tong, Tong. We got married in the 3rd year of my Ph.D studies. Our marriage is another achievement of my life besides my Ph.D. She is the person who knows every effort I made and every moment I cheered throughout my Ph.D. I express my earnest gratitude for her love, smile and support.

Abstract

The temperature dependence of equilibrium viscosity or relaxation time reflects an intrinsic property of glass-forming liquids known as fragility. The change in viscosity or relaxation time with temperature exhibiting an Arrhenius-like dependence is classified as being "strong"; whereas a non-Arrhenius temperature dependence of viscosity or relaxation time is classified as "fragile". The origin of large differences in fragility of different substances has not been well understood.

This work addresses the following questions about the origin of fragility: how differ strong liquids from fragile liquids, why the fragility of a substance changes under some circumstances, and how the fragility change is related to the changes in thermodynamic properties and structures. First, the glass transitions of the crystalline order-disorder $\text{Fe}_{50}\text{Co}_{50}$ and $(\text{FeCo})_{100-x}\text{Al}_x$ systems are studied. It is found that the thermodynamic and kinetic behaviors of the order-disorder systems mimic an ideal strong liquid with a critical point. With the support from the simulation results for liquid systems, a unified picture of an underlying lambda transition is proposed for understanding strong and fragile classifications. The second approach to understanding fragility is to directly investigate a strong-fragile transition in a strong bulk metallic glass-forming liquid. Electrostatic levitation and the synchrotron X-ray scattering techniques enable the in-situ studies of the structural changes of the metallic liquid over a wide temperature range in the supercooled liquid region. These experimental findings show that the dynamic strong-fragile crossover is associated with sudden structural changes and thermodynamic anomalies, suggesting a weak first-order liquid-liquid transition in the system.

Zusammenfassung

Die Temperaturabhängigkeit der Gleichgewichts-Viskosität bzw. der Relaxationszeit während des strukturellen Einfrierens ist dabei eine intrinsische Eigenschaft, die sogenannte Fragilität, der glas-bildenden Flüssigkeit. Folgt die Änderung der Viskosität bzw. Relaxationszeit als Funktion der Zeit einer Arrhenius-Gleichung wird das glas-bildende System als „stark“ klassifiziert, andernfalls als „fragil“. Die Ursache der beobachteten, großen Fragilitätsunterschiede verschiedener Systeme ist bisher jedoch nicht vollständig verstanden.

Diese Arbeit soll dem Ursprung der Fragilität von Materialien sowie den damit verbundenen kinetischen und thermodynamischen Änderungen nachgehen. Insbesondere sollen hierbei die folgenden Fragen beantwortet werden: Wie unterscheiden sich starke von fragilen Flüssigkeiten? Warum ändert sich die Fragilität einer Substanz unter gewissen Umständen? Wie ist diese Fragilitätsänderung mit Änderungen in den thermodynamischen Eigenschaften und der Struktur verbunden? Dabei wurden zunächst Glasübergänge von Ordnungs-Unordnungs-Übergängen in kristallinen $\text{Fe}_{50}\text{Co}_{50}$ und $(\text{FeCo})_{100-x}\text{Al}_x$ Systemen untersucht. Hierbei wurde festgestellt, dass das thermische und kinetische Verhalten der Ordnungs-Unordnungs-Übergänge dem einer ideal starken Flüssigkeit mit einem kritische Punkt entspricht. Unter Einbeziehung von Simulationsergebnissen an flüssigen Systemen wird als einheitliches Bild für das Verständnis des starken und fragilen Charakters verschiedener Flüssigkeiten ein zugrunde liegender Lambda-Übergang vorgeschlagen. Zusätzlich erfolgte im Rahmen dieser Arbeit eine direkte Untersuchung des Stark-Fragil-Übergangs innerhalb einer starken, Massivglas-bildenden Flüssigkeit. Durch Kombination von Elektrostatischer Levitation und Synchrotron-Röntgenbeugungsexperimenten gelang eine in-situ Untersuchung struktureller Änderung der metallischen Flüssigkeit über einen weiten Temperaturbereich. Hierbei konnte gezeigt werden, dass der dynamische Stark-Fragil-Übergang mit abrupten strukturellen Änderungen und thermodynamischen Anomalien einhergeht. Dies deutet auf einen zugrunde liegenden schwachen Phasenübergangs erster Ordnung hin.

Contributions and publications

For the work in Chapter 4, the author and I. Gallino planned and carried out the experimental work; the author and I. Gallino analyzed the data; C.A. Angell wrote the paper [1] with important literature and diagrammatic input from the author and advice from I. Gallino and R. Busch. In Chapter 5 and 6, the experiments and analysis were carried out by the author. For the work in Chapter 7, the author performed the calorimetric experiments and analyzed the data; F. Yang carried out density measurements. F. Yang, the author, J. Bednarcik and I. Kaban planned and carried out X-rays diffraction experiments; the author, F. Yang, J. Bednarcik, I. Kaban and O. Shuleshova analyzed the diffraction data; the author wrote the paper [2] with input from F. Yang and R. Busch and advice from A. Meyer, J. Bednarcik, I. Kaban and O. Shuleshova.

Here is a list of publications by the time of writing this thesis:

Peer-reviewed journals articles:

- Shuai Wei, Fan Yang, Jozef Bednarcik, Ivan Kaban, Olga Shuleshova, Andreas Meyer and Ralf Busch. Liquid-liquid transition in a strong bulk metallic glass-forming liquid. *Nature Commun.* **4**, (2013). doi:10.1038/ncomms3083
- Shuai Wei, Fan Yang, Jozef Bednarcik, Ivan Kaban, Andreas Meyer and Ralf Busch. Polyamorphous Transformation in Bulk Metallic Glass-forming Liquid and its Implication to Strong Liquids. *AIP Conf. Proc.* 1518, 260 (2013).
- Shuai Wei, Isabella Gallino, Ralf Busch and C. Austen Angell. Glass transition with decreasing correlation length during cooling of Fe₅₀Co₅₀ superlattice and strong liquids. *Nature Phys.* **7**, 178 (2011). doi:10.1038/nphys1823

Book chapters:

- Ralf Busch, Zach Evenson, Isabella Gallino and Shuai Wei. 12. Thermodynamics, Kinetics and Fragility of Bulk Metallic Glass

Forming Liquids *Fragility of Glass-forming Liquids*. Ed. A. L. Greer, K. Kelton and S. Sastry. Hindustan Book Agency, New Delhi, India. 2013.

Articles without peer-review process:

- Shuai Wei. Two liquid states in a strong bulk metallic glass-former. Photon Science 2013 Highlights and Annual Report, Deutsches Elektronen-Synchrotron (DESY). Printing: Heigener Europrint, Hamburg (2014).

The results included in this thesis have contributed to various international academic conferences and workshops:

- Dec. 2013. *2013 MRS Fall Meeting (Materials Research Society)* **Boston, MA, USA**. Oral presentation: Transitions in Liquid Structure, Fragility and Order in Bulk Metallic Glass-Forming Systems.
- Jul. 2013. *ISMAM2013 (The 20th International Symposium on Metastable, Amorphous and Nanostructured Materials)*. **Turin, Italy**. Oral presentation: In situ structural investigations of the strong-fragile transition on the bulk metallic glass-forming liquid Vit.1.
- Nov. 2012. *The 2. Sino-German workshop on bulk metallic glasses*. DLR, MP. **Cologne, Germany**. Oral presentation: Structural crossover in a Zr-based bulk metallic liquid at high temperature: another polyamorphism?
- Dec. 2012. *The 4th International Symposium on Slow Dynamics in Complex Systems*. **Sendai, Japan**. Oral presentation: Polyamorphous Transformation in Bulk Metallic Glass-forming Liquid and its Implication to Strong Liquids.
- Apr. 2011. *International Workshop on Dynamics in Viscous Liquids*. Accademia dei Lincei, **Rome, Italy**. Poster contribution: Chemical disordering of crystals and its relation to liquid-liquid transitions in strong liquids
- Jul. 2010. *ISMAM2010 (The 17th International Symposium on Metastable, Amorphous and Nanostructured Materials)*. **Zurich, Switzerland**. Oral presentation: Thermodynamics and Kinetics of the Glass Transition during Cooling of $\text{Fe}_{50}\text{Co}_{50}$ Superlattice with Respect to Structural Ordering and its Relation to Strong Liquids

- Mar. 2010. *Combined DPG (Deutsche Physikalische Gesellschaft) Spring Meeting of the Section Condensed Matter (SKM). Regensburg, Germany.* Oral presentation: Glass transition during cooling of Fe₅₀Co₅₀ superlattice and strong liquids

Contents

1	Introduction	1
2	State of the art	3
2.1	Metallic glasses	3
2.2	The glass transition	10
2.3	The fragility classification	12
2.4	Specific heat capacity at the glass transition	17
2.5	Two-state model	18
2.6	Energy landscape	21
2.7	Strong-fragile crossover and polyamorphic transition	23
2.8	The liquid-liquid critical point	33
3	Materials and methods	39
3.1	Samples preparations	39
3.2	Measurements of thermodynamic and kinetic properties	40
3.2.1	Differential Scanning Calorimeter (DSC)	40
3.2.2	Measurement of the kinetics of the glass transition	41
3.2.3	Measurement of high-precision heat capacity	42
3.2.4	Differential Thermal Analyzer (DTA)	43
3.2.5	Measurement of high-temperature heat capacity	44
3.3	In-situ synchrotron X-ray scattering on levitated droplets	45
3.3.1	Principles of total X-ray scattering experiments	45
3.3.2	X-ray sources	47
3.3.3	Experimental setup	50
3.3.4	Data analysis methods	50
3.4	Measurement of density	54
4	The glass transition and the order-disorder transition of Fe₅₀Co₅₀ and their relation with strong liquids	56
4.1	Introduction	56
4.2	Kinetics of the glass transition	57

4.3	Specific heat capacity on a long timescale	60
4.4	Lambda transition vs. liquid-liquid transition	64
4.5	Correlation length and strong liquids	68
4.6	Summary	69
5	The relation between the order-disorder transition and the glass transition of $(\text{FeCo})_{100-x}\text{Al}_x$	71
5.1	Introduction	71
5.2	Varying specific heat capacity peaks of glass transitions and order-disorder transitions	73
5.3	Kinetics of the glass transitions	76
5.4	Links between the order-disorder transition, cooperativity and the liquid phase transition in strong liquids	81
5.5	Summary	83
6	Determination of fragility from single DSC-scans	85
6.1	Introduction	85
6.2	Fragility and T_g -scaled slope of DSC scans	87
6.2.1	Comparison with other fragility-related correlations	93
6.3	Summary	96
7	The liquid-liquid transition in Vit.1	98
7.1	Introduction	99
7.2	Specific heat capacity maxima of the liquid	100
7.3	Monitoring the melting process using in-situ synchrotron X-ray diffraction	102
7.4	The relation between specific heat capacity and viscosity	104
7.5	Investigation of the local structure using synchrotron radiation	108
7.6	Real space analysis with pair distribution functions	112
7.7	Liquid volume	115
7.8	First-order liquid-liquid transition by nucleation and growth	116
7.9	Liquid-liquid transition of Vit.1 in a big picture	121
7.10	Interpretation of liquid structure changes	123
7.11	Polyamorphism in other metallic glass-forming systems	124
7.12	Summary	125
8	Summary and conclusions	126
8.1	The glass transition and the fragility of order-disorder alloys	126
8.2	The relation between the fragility, thermodynamics and the structure of a bulk metallic glass-forming liquid	128
	Copyright permissions	130

CONTENTS

Molar mass of substances	131
Abbreviations	132
Bibliography	133

Chapter 1

Introduction

All liquids can be made into glasses if the systems are cooled fast enough and fall out of equilibrium while crystallizations are avoided [3, 4]. The field of glass science encompasses a broad range of temperatures, including studies not only of the glassy and glass transition regime but also of equilibrium liquid behaviors over the entire temperature range from infinitely high temperatures to 0 K.

Transport properties, for example, viscosity η , relaxation time τ and diffusivity D , of most liquids in the temperature range from the glass transition to high temperatures are found to deviate from the Arrhenius law to some extent [5]. Liquids that show Arrhenius-like dependence of the equilibrium viscosity (or relaxation time) on temperature as the glass transition is approached are defined as dynamically "strong" while substances whose equilibrium viscosities deviate much more from the Arrhenius law are classified as "fragile" [6]. The origin of the drastic dynamic slowdown of fragile liquids as approaching the glass transition has been a central topic of the field of molecular, inorganic and polymer glasses as well as metallic glasses.

The studies on the origin of fragility and the fragility-related thermodynamic behavior of various glass-forming liquids suggest that there is a thermodynamic transition hidden below the glass transition in some liquids, and in some other liquids, above the glass transition in the undercooled liquid region [7]. Such a thermodynamic transition is difficult to establish due to experimental difficulties in reaching equilibrium below the glass transition or avoiding crystallization in the undercooled liquid region. The thermodynamic phase transformation is speculated to be a polyamorphic transition between two distinct amorphous or liquid phases. This is reminiscent of the commonly seen polymorphism in crystalline solids, for example, the order-disorder transition in crystalline superlattice $\text{Fe}_{50}\text{Co}_{50}$. Researchers have studied, for years, anomalous phenomena in water and found a polyamorphic transition or a liquid-liquid transition hidden in the experimentally inaccessible regime of the supercooled water [8, 9, 10]. The list

of candidates for polyamorphisms includes network oxide glasses (e.g., silica) and single-component systems (e.g., silicon and germanium) as well as metallic glasses [11, 2]. Polyamorphic transitions are found usually accompanied by crossovers in dynamic properties (i.e., strong-fragile crossover). The link between polyamorphisms and changes in fragility, however, has been not well understood and further experimental and theoretical explorations in various systems are desirable.

Metallic glasses are the relatively members of the glass family. Since the 1960s, amorphous metals have been rapidly developed and intensely studied. The critical casting thickness of metallic glasses has been increasing from $\sim 10\mu\text{m}$ of amorphous Au-Si foils [12] to centimetre scales of bulk metallic glasses (BMG) [13]. The extensive characterizations on bulk metallic glasses not only provide a comprehensive picture of thermodynamics and kinetics of this class of materials but also offer insight into metastable states and non-equilibrium states of liquids and glasses in general. Bulk metallic glasses have a high thermal stability with respect to crystallization. On one hand, the driving force between liquid and crystalline states is small in good glass-formers. On the other hand, the kinetics are sluggish and impede the nucleation and growth of crystals. The liquid equilibrium viscosities of multi-component, Zr-based BMG formers are very high, compared with those of simple metals. The fragilities of Zr-based BMGs are found to be medium-strong in the strong/fragile classification. However, recent high-temperature viscosity measurements show that those Zr-based BMGs may become fragile when the systems are heated far above their melting points. This indicates that fragilities of BMGs may change with temperature, which is reminiscent of the dynamic crossover phenomenon in water and liquid silica that are involved in polyamorphic transitions.

This dissertation is devoted to the understanding of the origin of fragility and the fragility-related thermodynamics and kinetics of glass-formers, especially, those dynamically strong substances, including bulk metallic glasses. Before the experimental results are discussed, a brief literature review is given in Chapter 2. The materials and methods are described in Chapter 3. In Chapter 4, a study of the glass transition during order/disordering of $\text{Fe}_{50}\text{Co}_{50}$ is presented. In the discussion of the results, we propose a unified picture for understanding fragility classification of liquids. As an extension of Chapter 4, we change the compositions of Fe-Co and study the relation between glass transitions and order-disorder transitions in Chapter 5. Chapter 6 presents a correlation between fragilities and the scaled slopes of DSC scans during glass transitions of different metallic glasses. In Chapter 7, the experimental results of thermodynamic and structural investigations on the bulk metallic glass-former $\text{Zr}_{41.2}\text{Ti}_{13.8}\text{Cu}_{12.5}\text{Ni}_{10}\text{Be}_{22.5}$ (Vit.1) are shown. The observed anomalous thermodynamic and structural changes suggest the existence of a weak first-order liquid-liquid transition in the system. At the end, a summary of the work is given in Chapter 8.

Chapter 2

State of the art

The aim of this chapter is to give a brief literature review of the related research done by others on metallic glasses, glass transitions and supercooled liquids.

2.1 Metallic glasses

Metallic glasses are also known as amorphous alloys, which were first discovered in 1959 in the laboratory of Professor Duwez at the California Institute of Technology. Duwez and his coworkers made a thin layer of amorphous alloy $\text{Au}_{75}\text{Si}_{25}$ by splat quenching the liquid as fast as 10^8 K s^{-1} [12]. Since then, metallic glasses have been the focus of extensive studies [14, 13]. Bulk metallic glasses are developed with slower nucleation and growth kinetics and have been processed by slower cooling rates of $< 100 \text{ K s}^{-1}$ [15, 16]. They are available in thicknesses up to a few centimeters with novel properties for potential applications [17, 18]. Furthermore, studies of metallic glasses have advanced the knowledge and fundamental understanding of glasses and liquids.

Metallic glasses are disordered materials. The mechanical properties of bulk metallic glasses are known to be related to their compositions and thermal history. A slightly compositional change may lead to a very different yield strength or ductility of the materials. Bulk metallic glasses usually exhibit high hardness and high yield stresses, close to the theoretical strength (Fig. 2.1) [19]. Moreover, they have high yield strains (the ratio of yield stress to Young modulus) and resiliences [20]. These extraordinary properties make bulk metallic glasses possible to be applied, for instance, in making surgical blades, and in the field of sport products (e.g., tennis rackets, golf clubs) [21]. However, bulk metallic glasses lack tensile ductility [22], although some metallic glasses show good ductility under compression tests [23, 24, 25]. Bulk metallic glasses do not have dislocations and slip-systems that are responsible for plastic deformations in crystalline metals [26].

Upon yielding, shear bands are formed in bulk metallic glasses and plastic flow is highly localized in shear bands [27, 28, 20]. The shear bands are initiated by local strain softening which are caused by an accumulation of free volume due to the inhomogeneity in strain rate. Once shear bands are formed, further localized strain softening is promoted within the shear bands which are preferred initiating sites for crack propagations. The highly localized strain softening in shear bands causes the apparent brittleness of bulk metallic glasses. It is realized that the formation of multiple shear bands distributes strains to more shear bands. This decreases local plastic strains in each shear band. Therefore, it increases overall the fracture strain and toughness of metallic glasses [27, 29, 30]. In an alternative approach, a second crystalline phase is introduced to make composite materials to improve plasticities [31, 32]. For example, the dendritic composites of bulk metallic glasses, in which a ductile dendritic phase is formed in amorphous matrix, achieved high yield strengths and tensile ductility [27]. The dendritic arms intersect shear bands and impede the propagation of shear bands. Therefore, the fracture is delayed and the tensile ductility is improved [25].

Bulk metallic glass-formers are usually multicomponent close-to-eutectic systems with negative heat of mixing and low melting points [33, 16]. Figure 2.2 shows the time-temperature-transformation (TTT) diagram for the crystallization of a typical bulk metallic glass-forming system $\text{Zr}_{41.2}\text{Ti}_{13.8}\text{Cu}_{12.5}\text{Ni}_{10}\text{Be}_{22.5}$ (Vit.1). The increasing driving force for crystallization and decreasing diffusions during undercooling cause the "nose" shape of onsets of crystallization in the TTT diagram. For a good glass former, the supercooled liquid state exhibits a high thermal stability against crystallization. This is reflected in the time interval between 0 s and the time corresponding to the nose for crystallization in the TTT diagram. A larger time interval before crystallization indicates a slow critical cooling rate and a better glass-forming ability. When the liquid is cooled fast enough (e.g., $> 1 \text{ K s}^{-1}$ for Vit.1) to bypass the nose in Fig. 2.2, the crystallization is avoided and the glass is formed [34].

The heat capacities c_p of bulk metallic glass-forming liquids behave differently towards T_g as shown in Fig. 2.3. The lowest line is the c_p of crystals with the typical values of Dulong-Petit law around $3R = 24.94 \text{ J g-atom}^{-1} \text{ K}^{-1}$. The excess specific heat capacity, c_p^{ex} , (difference between the supercooled liquid state and the crystalline state) at T_g show quite different values. The $c_p^{ex}(T_g)$ for Vit.1 and Vit.4 are only about half of that of $\text{Au}_{53.2}\text{Pb}_{27.5}\text{Sb}_{19.2}$. Note that the curves in the supercooled liquid region are interpolated by fitting the data near glass transitions and the data above the melting point.

The kinetics of metallic glass-formers play an important role in determining the glass-forming abilities and relaxation behaviors of glasses. Viscosities reflect atomic mobilities in liquids and are proportional to structural relaxation times [3]. As shown in Fig. 2.4, the viscosities of a number of metallic glass-forming

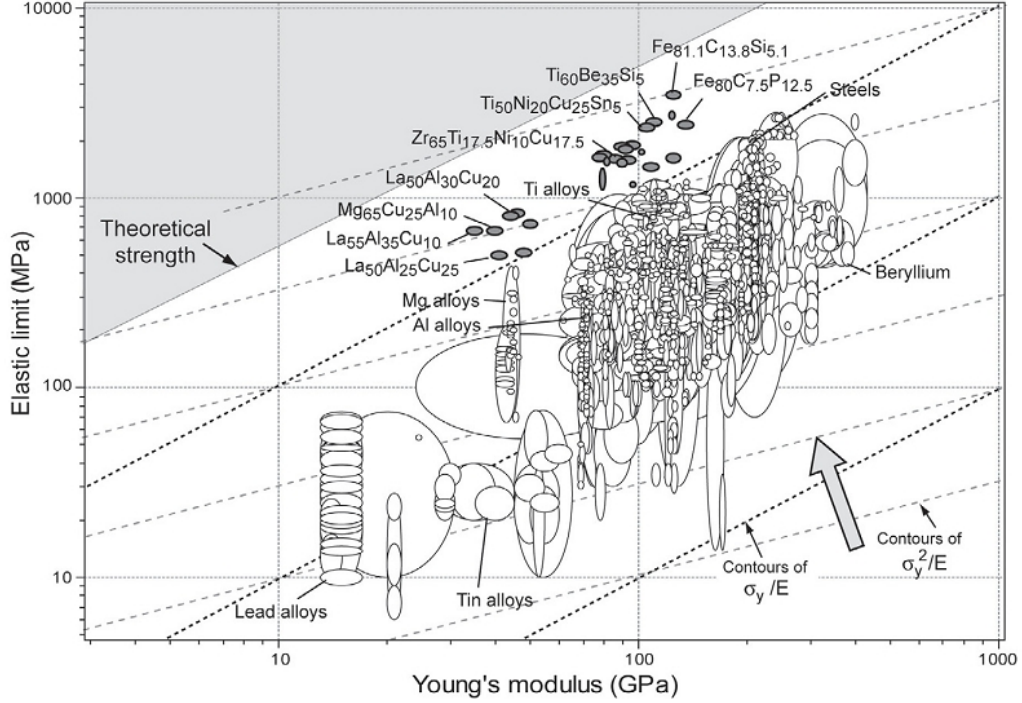


Figure 2.1: Ashby Plot. Elastic limit, σ_y , vs. Young's modulus, E , for metals, alloys, metal matrix composites and metallic glasses (taken from ref. [19]). The contours show the yield strain σ_y/E and the resilience σ_y^2/E . Metallic glasses have a larger yield strain and are able to store more elastic energy per unit volume than most of other metals.

liquids are plotted using a base 10 logarithmic scale against T_g -scaled temperature [16] (also called Angell-plot [6]). These are compared with the viscosities of liquid silica which exhibits an Arrhenius-like behavior and of a non-Arrhenius molecular liquid, *o*-terphenyl [5]. The multicomponent bulk metallic glass-formers show much higher viscosities by orders of magnitude than those of poor glass-formers, because the sluggish kinetics of the bulk metallic glass-formers impede nucleation and growth of crystals [16]. The temperature dependent viscosities of liquids can be described by the Vogel-Fulcher-Tammann (VFT) equation [35, 36]. A detailed description will be given in the Section 2.3.

The structures of metallic glasses determine their properties. Metallic glasses are formed by freezing the supercooled liquid state when crystallization is avoided. Therefore, no long-range order like crystalline lattice structure exists. There is only short-range and/or medium-range order present in liquids or glasses. The short-range order develops on the length scale of the nearest neighbors ($< 5 \text{ \AA}$) and the medium-range order is suggested beyond 1 nm [37, 38].

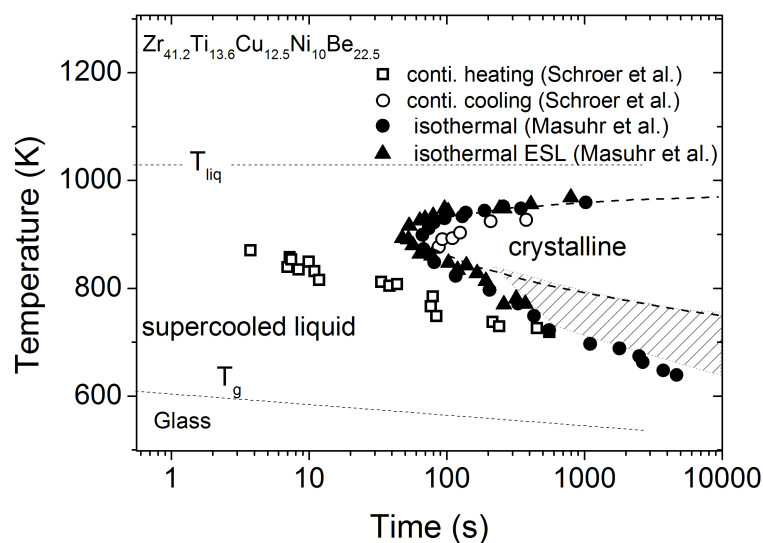


Figure 2.2: Time-temperature-transformation diagram for crystallization of Vit.1. The solid triangles and dots are the data from the electrostatic levitation and the measurement with graphite crucibles, respectively [34]. The open symbols are measured from continuous heating and cooling [22].

The structure of metallic glasses has been investigated with synchrotron X-rays and neutron scattering experiments with assistance of computer simulations in the last decades [37]. Bernal [39] first described the structure as dense random packing of atoms. Following studies, however, suggested that the densely packed atoms are not randomly arranged, because random packing of atoms of different sizes is not efficient [40, 37, 38]. The importance of efficient packing is emphasized, for example, by Miracle’s dense efficient packing model [38, 41]. His model rationalized the compositions of good glass-formers from the topological point of view. Sheng et al. [40] suggested that binary metallic glasses are dense packed solute-centered quasi-equivalent clusters. Bonds tend to form between different atomic species because of large negative enthalpy of mixing. The ratio of the radii of solute atoms to that of solvent atoms determines the number of atoms that can fit into the coordination shells. The coordination numbers in metallic glasses are usually from 8 to 20 [20].

The idea underlying the efficient packing models is that some certain packing schemes are more efficient and more energetically favorable than others [41, 43]. Therefore, such efficiently packed clusters are more stable and may be dominant in liquids and metallic glasses. In the example shown in Fig. 2.5, the simple binary metallic glass $Zr_{84}Pt_{16}$ has Pt atoms as the centered solute and Zr atoms as around solvent atoms. These clusters are densely packed to form the medium-range order on the length scale of a few clusters and fill the three dimensional space. Using

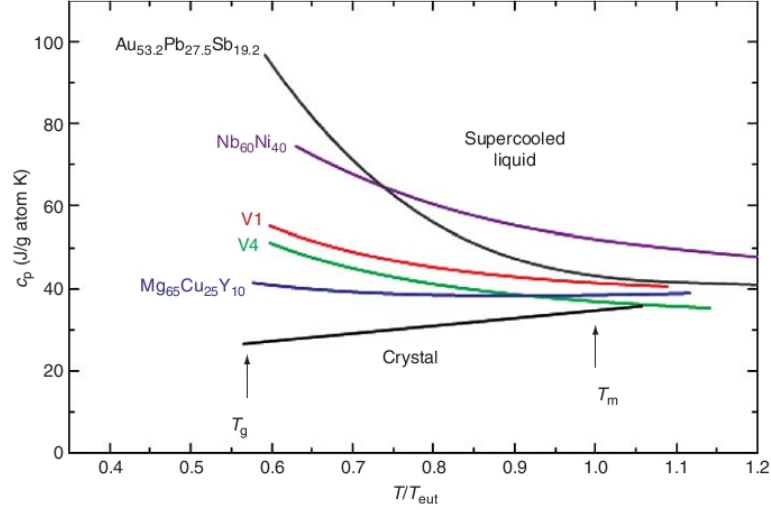


Figure 2.3: Specific heat capacity of metallic glass-forming liquids vs. temperature scaled by eutectic temperatures. Note that the curves in the supercooled liquid regions are calculated lines using the parameters obtained by fitting the data near glass transitions and the data above melting points (taken from ref. [16]).

simulations Cheng et al. [42] showed that icosahedral $\langle 0, 0, 12, 0 \rangle$ order is dominant¹ in metallic liquids and the number of the icosahedral increases sharply as approaching T_g (see Fig. 2.6). The icosahedral order appears to be responsible for the drastic increase in viscosity during cooling and is associated with the anomalous high specific heat capacity near T_g .

¹The local atomic environment is characterized with the Voronoi index $\langle n_3, n_4, n_5, n_6 \rangle$, where n_i denotes the number of i -edged faces of the Voronoi polyhedron and $\sum_i n_i$ is the total coordination number of the solute atom.

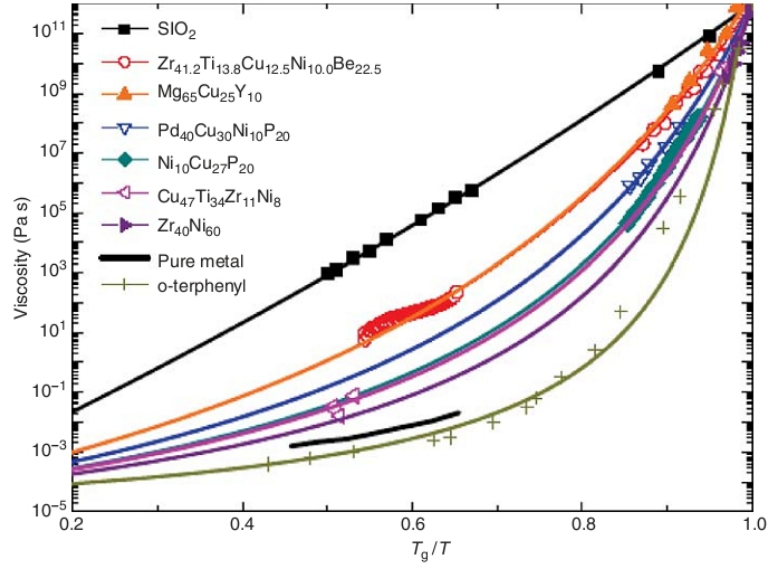


Figure 2.4: Viscosity data of metallic glass-forming liquids compared with the extreme strong silica and the very fragile o-terphenyl. The metallic glass-forming liquids are ranged in the medium-fragility. Vit.1 is the strongest (lowest fragility) liquid in the metallic glasses family (taken from ref. [16]).

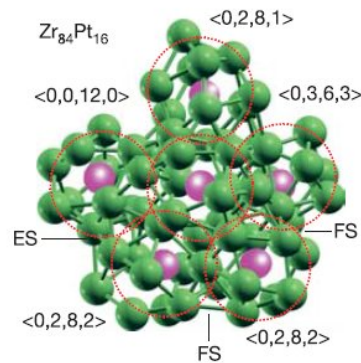


Figure 2.5: Packing of atoms on the short-range order (clusters) and the medium-range order (interlinked clusters) in the $Zr_{84}Pt_{16}$ glass. (taken from ref. [40]).

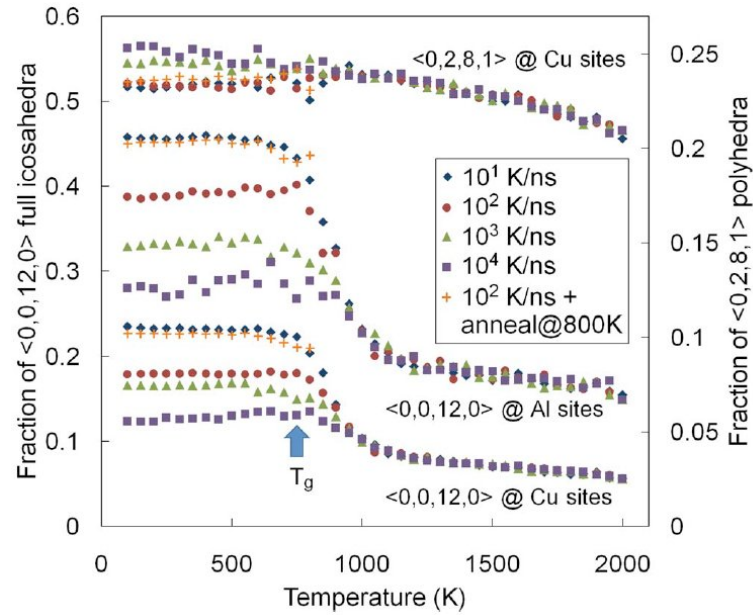


Figure 2.6: Icosahedral ($\langle 0,0,12,0 \rangle$) order increases rapidly with decreasing temperature. As a comparison, the fraction of $\langle 0,2,8,1 \rangle$ polyhedron does not show a significant increase during cooling towards T_g (taken from ref. [42]).

2.2 The glass transition

A glass transition is associated with a structural arrest that occurs during cooling of a liquid. During this transition the system falls out of metastable equilibrium and the structure appears "frozen" on the laboratory timescale (of the order of 100-1000 s) [5, 3, 44], because the atoms or molecules rearrange so slowly that they cannot adequately explore all configurations in the available time allowed by the cooling rate. It is therefore not a transition in the thermodynamic sense. It is, instead, always associated with the crossing of experimental and systems internal time scales (ergodicity breaking or restoring) [3].

As a liquid is cooled, the enthalpy, ΔH , entropy, ΔS and volume ΔV of the system changes are shown schematically in Fig. 2.7. There is a continuous change in ΔH , ΔS and ΔV whereas a sudden change in specific heat capacity, c_p , thermal expansion coefficient, α and compressibility, β , is observed. For a typical example, the specific heat capacity of molecular glass-former glycerol is shown in Fig. 2.8. The bold and thin curves represent the c_p measured during cooling and heating using calorimetry, respectively. The cooling rate is 10 K min^{-1} and the heating rate is kept the same ($q_h = q_c$). By doing so, the onset of the glass transition on heating, $T_{g,onset}$, coincides with the midpoint of the cooling curve, $T_{g,mpc}$, as well as the fictive temperature, T_f [3, 45]. However, the glass transition observed in laboratory is a kinetic freezing-in or unfreezing event, which leads to experimental difficulties in studying the thermodynamic equilibrium below T_g . This raises one of the long-standing questions in the field whether there is a *thermodynamic* transition below the kinetic glass transition temperature, T_g [46]. This is related to another well-known problem, the Kauzmann paradox.

The Kauzmann Paradox

In 1948, Walter Kauzmann published one of the most influential papers in glass science [47] in which the famous Kaumann Paradox was known and became one of the most challenging problems. Figure 2.9 shows the graphical presentation of the Kauzmann Paradox. The difference in entropy between the crystal and liquid state at the melting point, ΔS_m , is used as a scaling parameter [48, 47].

The difference in entropy between the liquid state and its corresponding crystalline state is called excess entropy, ΔS_{ex} , which varies differently during undercooling for different classes of substances. For B_2O_3 , ΔS_{ex} , tends to disappear in the vicinity of 0 K. However, for other liquids, ΔS_{ex} decreases so rapidly that a simple extrapolation from liquid behaviors would lead to zero at about 2/3 of melting temperatures. This means a lower temperature would cause a negative ΔS_{ex} which does not seem to make physical sense since the entropy of the crystalline state should not be greater than the entropy of the liquid state. In the

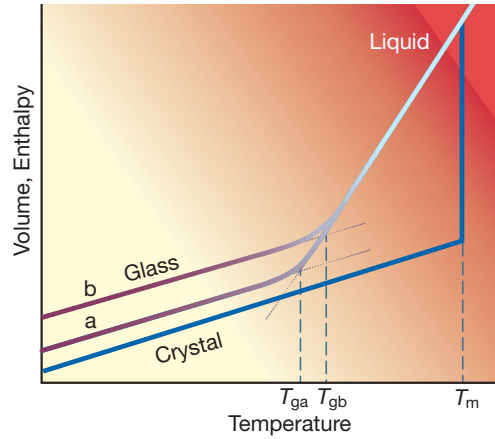


Figure 2.7: Schematic plot of the enthalpy or volume change with decreasing temperature. The enthalpy, entropy and volume change abruptly at the glass transition temperature T_g . Depending on the cooling rate, T_g occurs at different temperatures T_{ga} or T_{gb} and the corresponding glassy state is also different, marked by a and b. (taken from ref. [4])

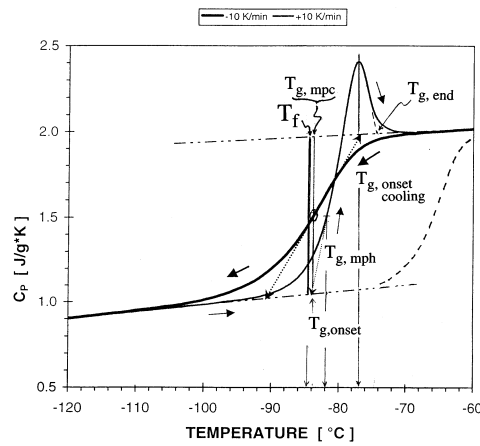


Figure 2.8: The specific heat capacity of glycerol measured using differential scanning calorimeter. The bold and thin curves represent measurements at the same scanning rate during cooling and heating, respectively. The glass transition temperature T_g is commonly defined as $T_{g,onset}$ on the heating curve, which coincides with the fictive temperature T_f and the middle point $T_{g,mpc}$ of the cooling curve. The hysteresis on the cooling and heating curves is a typical glass transition behavior (taken from ref. [3]).

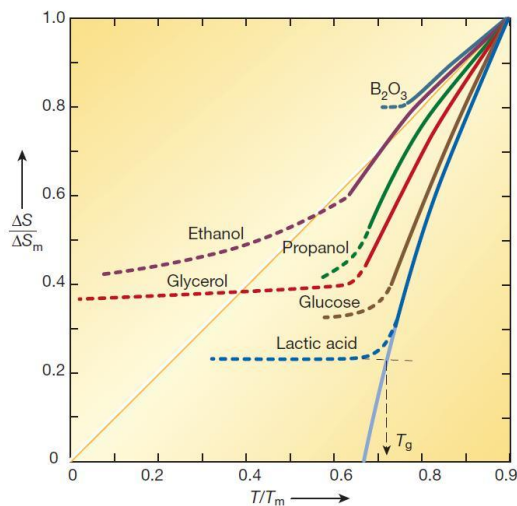


Figure 2.9: The graphical presentation of the Kauzmann Paradox. Temperature dependence of the scaled excess entropy for several undercooled liquids at ambient pressure. The glass transitions always intervene before the vanishing of the excess entropy. (taken from ref. [47, 4]).

reality, a glass transition occurs at a temperature T_g [48, 47] and this negative ΔS_{ex} problem is prevented.

At T_g , increasingly sluggish motions of the particles hamper further configurational changes to more ordered states as the system is further cooled. Therefore, equilibrium cannot be reached at lower temperatures. The thermodynamic crisis (negative ΔS^{ex}) is avoided by a pure kinetic phenomenon. This is the so-called "Kauzmann Paradox"[47].

2.3 The fragility classification

As the glass transition temperature T_g is approached from above, the relaxation times τ (or viscosities η) of liquids change with temperature following different patterns, which leads to the "fragility" classification of liquids. The fragility concept is proposed by Angell [6] to describe different scaling behavior of relaxation times with temperatures.

For fragile liquids (the lower substances, e.g., o-terphenyl, in Fig. 2.10), the changes in viscosity on cooling are much greater than expected from the Arrhenius law as T_g is approached. For strong liquids, such as GeO_2 and SiO_2 , (the upper substances in Fig. 2.10), the viscosities exhibit Arrhenius-like dependence on temperatures.

The fragility determined from kinetic properties is called kinetic fragility. It

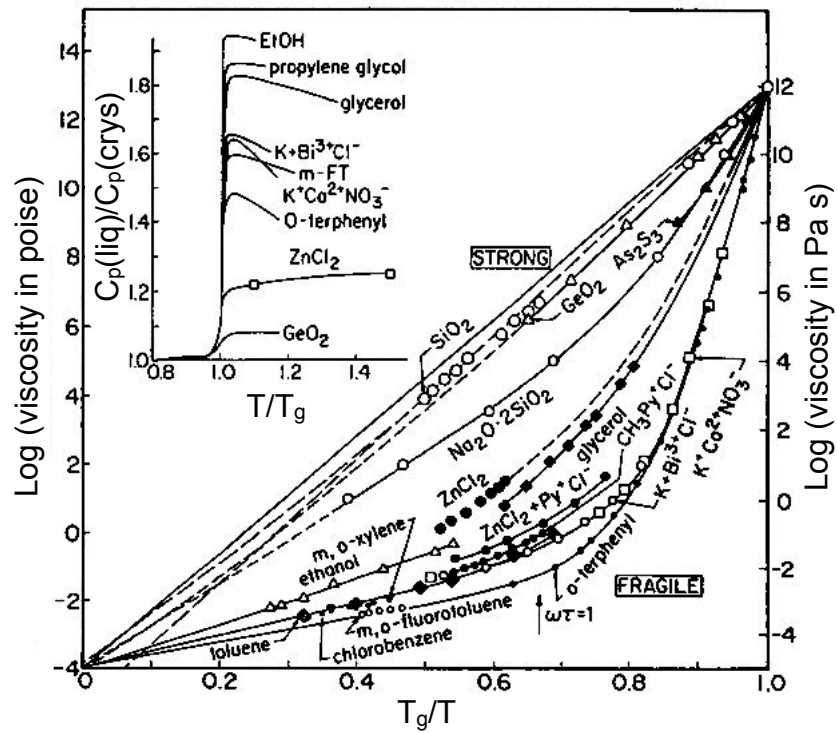


Figure 2.10: Fragility-plot. The fragility concept is proposed to describe how much the viscosity (also relaxation time) deviates from the Arrhenius law from the infinitely high temperature to glass transition temperatures. The liquids in the lower part are fragile, in contrast to strong liquids in the upper part. The inset shows the heat capacities of different liquids, as T_g is approached from above (taken from ref. [6]).

can be described by the steepness index m , which is defined as the slope of $\log_{10}\tau$ vs. T_g/T curve at the glass transition temperature T_g measured in calorimeter at 20 K min^{-1} in the Angell-plot

$$m = \left. \frac{d \log_{10} \tau}{d(T_g/T)} \right|_{T=T_g}, \quad (2.1)$$

where m describes how fast the relaxation time increases as approaching T_g from above. Note that τ can be replaced by viscosity η , as they are proportional to each other according to the Maxwell relation, $\eta = G_\infty \tau$, where G_∞ is the infinite frequency shear modulus [3]. The extreme strong system has the lowest fragility value $m \sim 16$; whereas a more fragile system has a greater value of m up to the maximum value ~ 170 [3].

The temperature dependence of τ can be also described with the Vogel-Fulcher-Tammann (VFT) equation [35, 36]

$$\tau = \tau_0 \exp\left(\frac{D^* T_0}{T - T_0}\right), \quad (2.2)$$

where the pre-exponent τ_0 is the theoretical infinite-temperature limit of the relaxation time, assumed as 1×10^{-14} s for liquid quasi-lattice vibration period [49, 50]. The VFT parameter D^* characterizes also the fragility of a liquid. A greater value of D^* describes more "strong" kinetics of the liquid and corresponds to a smaller value of m . D^* can be related to m via the equation $D^* = 590/(m - 17)$, where the constant 17 is the minimum value of m for the D^* determined from viscosity data; it is 16 for the D^* determined from relaxation time data [51].

There are other equations that account for the deviation of τ or diffusivity from the Arrhenius law. The most widely used is the Adam-Gibbs equation, which provides an important connection between kinetic properties and thermodynamic quantities. It has less fitting parameters than the VFT equation. The Adam-Gibbs equation includes a thermodynamic quantity, configurational entropy S_c [49]

$$\tau = \tau_0 \exp\left(\frac{C}{TS_c}\right), \quad (2.3)$$

where τ_0 is a constant and C is the free energy barrier for cooperative rearrangements. Note that excess entropy S_{ex} is often used as an approximation of the configurational entropy, S_c , when applying the equation for data fitting. However, the approximation has been pointed out to be poor in many cases [52].

The fragility concept was first proposed based on kinetic data (relaxation times or viscosities) [6]. A similar scaling behavior of the excess entropy, S_{ex} , was discovered by Martinez and Angell [53], known as the "thermodynamic fragility".

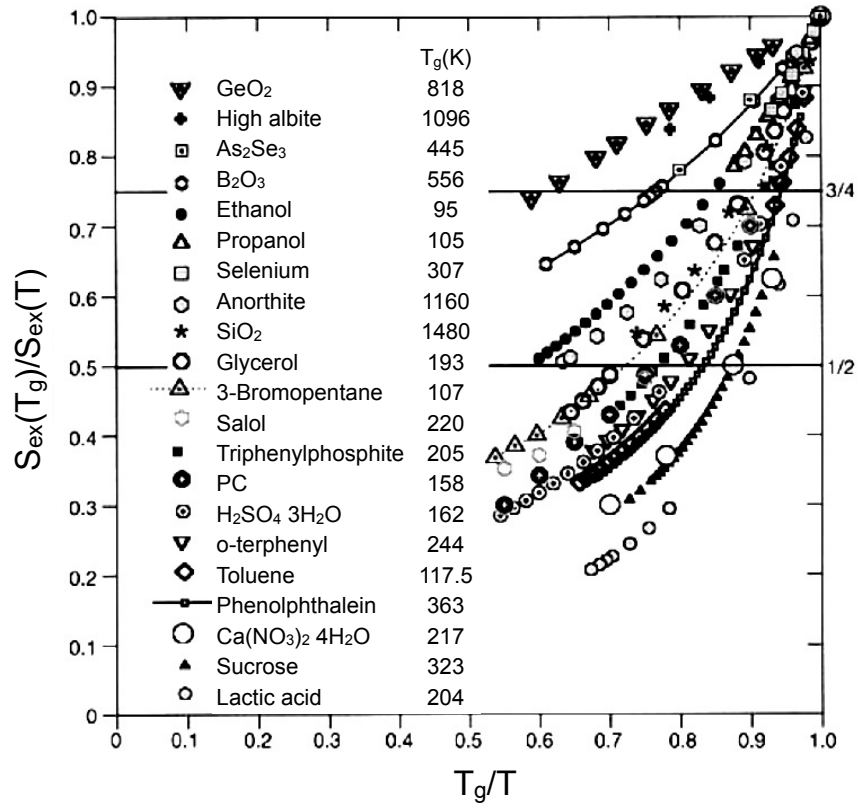


Figure 2.11: Thermodynamic fragility-plot (taken from ref. [53]). The scaled excess entropies of various substances are plotted against the T_g -scaled temperatures. The so-called thermodynamic fragility is consistent with the kinetic fragility obtained from pure kinetic data. This implies a fundamental connection between liquid thermodynamics and kinetics in liquids and glasses.

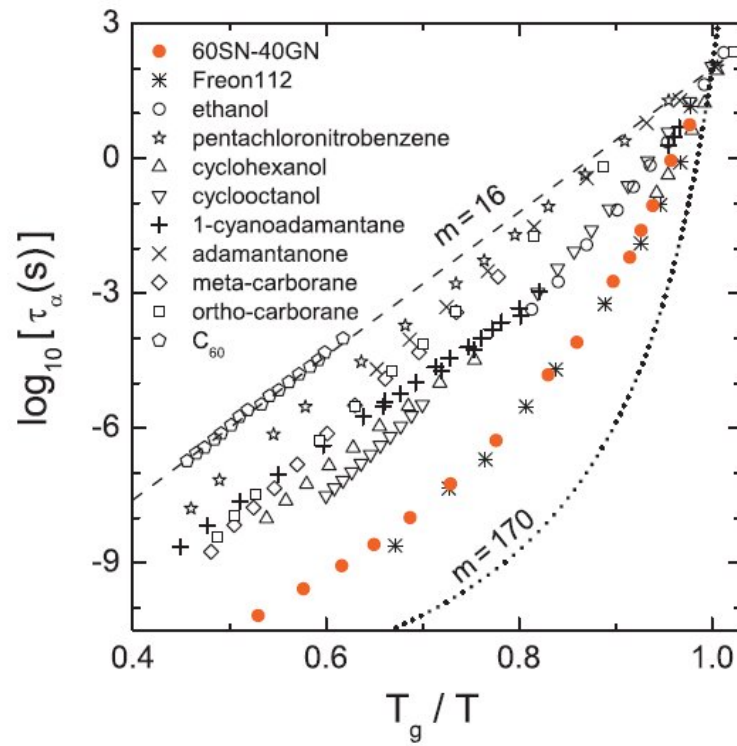


Figure 2.12: Fragility-plot of α relaxation times of various plastic crystals. Most of them show strong behaviors while fragile examples exist in the pattern, for example, Freon112 and 60SN-40GN (taken from ref. [54]).

The scaled excess entropies show a consistent trend with scaled viscosity behaviors in the kinetic fragility. As shown in Fig. 2.11, fragile liquids have more rapid changes of the excess entropy in the liquid state than strong liquids. Like the definition of the kinetic fragility, T_g here is again used as a reference temperature for the thermodynamic fragility, which provides the advantage that fragility is a pure liquid-state quantity [53]. The excess entropy used to define the thermodynamic fragility contains both configurational entropy and vibration-related contributions. Upon heating, the increase of configurational entropy is promoted by the increase in vibrational entropy above T_g due to quasi-lattice bond excitations. How rapid the vibrational entropy is generated depends on the basin shapes in energy landscapes. Martinez and Angell proposed the correlation between the kinetic and thermodynamic fragility originates from the excitation modes in the energy landscapes of liquids [53]. A detailed explanation of how excitation modes affect the fragility is given in the next section.

There is a class of materials called plastic crystals that exhibit the kinetic freezing-in ("glass" transition) of orientational order of molecules while the center of gravity of the molecules stays ordered on a crystalline lattice [5]. Brand et al. [55] and Bauer et al. [54] studied the relaxation dynamics of plastic crystals and compared their temperature dependent α relaxation times, as shown in Fig. 2.12. A strong-fragile pattern also exists in the non-liquid systems. Most plastic crystals are strong. The most fragile behavior is seen in Freon112 with $m = 68$ and 60SN-40GN with a relatively small VFT-parameter $D^* = 12.8$ and $m = 62$ [55, 56].

2.4 Specific heat capacity at the glass transition

The specific heat capacity jump at the glass transition, $\Delta C_p(T_g)$, reflects the access of the system to configurational degrees of freedom in the liquid state above the glass transition [57]. $\Delta C_p(T_g)$ is measured from the specific heat capacity difference between the liquid state and the extrapolation of the glassy state, $\Delta C_p(T_g) = C_p^l(T_g) - C_p^{gl}(T_g)$. For most substances, $\Delta C_p(T_g)$ is approximately equal to the excess specific heat capacity at T_g , $\Delta C_p^{ex}(T_g)$, which is the specific heat capacity difference between the liquid state and crystalline state, $\Delta C_p^{ex}(T_g) = C_p^l(T_g) - C_p^{crys}(T_g)$.

The specific heat capacity of a liquid contains the contributions from the vibrational specific heat capacity and the configurational specific heat capacity. It is found that the specific heat capacity changes of different liquids at the glass transition can differ largely from liquid to liquid because the vibrational and configurational states of a liquid can vary largely at the glass transition. Angell found that the specific heat capacity behavior at the glass transition is related to

the fragility of the substances [5]. He pointed out that the fragile liquids usually have large specific heat capacity jumps, $\Delta C_p(T_g)$; and strong liquids typically show small jumps. The empirical correlation between the fragility and the specific heat capacity jump was explained by Xia et al. with a random first order transition theory of glasses [58]. They showed that the configurational specific heat capacity is inversely related to the VFT-fragility parameter D^* . In the inset of Fig. 2.10, the ratio C_p^l/C_p^{cryst} was shown to be very different for strong and fragile liquids [6]. Huang and McKenna [59] proposed using the ratio C_p^l/C_p^{cryst} as a measure of thermodynamic fragility and examined a large dataset for molecular organic, polymeric and inorganic glass-forming liquids. They found that a positive correlation between C_p^l/C_p^{cryst} and kinetic fragility only exists in inorganic glass-formers. Wang et al. [60] proposed that the specific heat capacity jump should be scaled by the entropy of fusion, $\Delta C_p(T_g)/\Delta S_m$, as a measure of the thermodynamic fragility and they found that it is well correlated with the kinetic fragility for 54 non-polymer glass-forming liquids: The more fragile a liquid is, the larger value $\Delta C_p(T_g)/\Delta S_m$ has.

Besides the magnitude of the specific heat capacity jumps at the glass transition, the trend of changes in specific heat capacity as approaching T_g during cooling was also worth noting for strong and fragile liquids. In fragile liquids, the *excess* specific heat capacity, ΔC_p^{ex} , increases rapidly during cooling and then drops sharply when the glass transition is encountered. In contrast, very strong substances (e.g., network glasses, BeF_2 and SiO_2) show the opposite trend that the specific heat capacity tends to decrease with decreasing temperature towards the glass transition temperature [7].

2.5 Two-state model

The two-state model has been proposed by Angell and Rao [61] to understand the thermodynamics of glass transitions and glass-forming systems. The authors propose that the interacting particles in glasses or liquids can be modeled by a weakly interacting bond lattice. The model supposes that the difference in thermodynamics between supercooled liquid states and solid (vitreous or crystalline) states is that in the liquid the number of excited bonds can change with changing temperature above T_g . The ground state of such a system is known as "ideal glass state" in which all bonds are completely locked and mildly strained [61]. Accordingly, when the system is heated up above T_g , the thermal energy excites these bonds and the bonds are "broken". Each broken bond and a strain-release with local adjustment of centers of atomic vibration are treated by the authors as an elementary configurational excitation of the glass quasi-lattice.

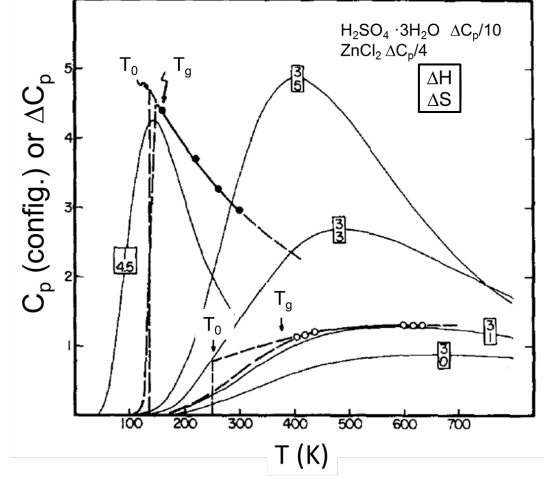


Figure 2.13: Specific heat capacity for non-cooperative two-state model with single excitation energy. The experimental data appropriately scaled down are plotted for ZnCl_2 ($\Delta c_p/4$) and $\text{H}_2\text{SO}_4 \cdot 3\text{H}_2\text{O}$ ($\Delta c_p/10$). The numbers on the curves represent the ΔH^* and ΔS^* , respectively (taken from ref. [61]).

The mole fraction of broken bonds at a temperature T can be written as [61]

$$X_B = [1 + \exp(\Delta G^*/RT)]^{-1}, \quad (2.4)$$

where the Gibbs free energy $\Delta G^* = \Delta H^* - T\Delta S^*$ is the free energy between the ground state and the totally excited state, including the enthalpy difference ΔH^* for excitation and the entropic component $T\Delta S^*$, per mole of broken bonds. R is the ideal gas constant.

The specific heat capacity due to the "bond" breaking is [61]

$$c_p^{conf} = (\partial H/\partial T)_p = R(\Delta H^*/RT)^2 X_B(1 - X_B). \quad (2.5)$$

The bond breaking raises a specific heat capacity bump, the shape of which depends on the values of the excitation enthalpy ΔH^* and the excitation entropy ΔS^* . The maximum value of c_p depends only on ΔS^* ; the temperature of the maximum c_p depends on both parameters, the ratio of $\Delta H^*/\Delta S^*$. The calculated configurational c_p comparing with experimental excess c_p is shown in Fig. 2.13.

In this model, c_p^{conf} does not exhibit any singularity but only a bump-like shape. However, this model does not give rise to sufficiently steep Δc_p as being frequently seen in the excess specific heat capacity of fragile glasses. The reason for such a rapid increase in experimental Δc_p is attributed to the cooperative effects that may produce a singularity associated with a possible liquid-liquid (or polyamorphic) phase transition [61, 62, 63]. Taking the cooperative behavior into account, the bond energy ΔH^* now consists of two terms

$$\Delta H^* = \Delta H_0^* + \Delta H_1^*, \quad (2.6)$$

where ΔH_1^* vanishes cooperatively with varying temperature:

$$\Delta H_1^*(T) = \Delta H_1^*(0) / \{1 + \exp[(T - T_r)/D]\}, \quad (2.7)$$

where T_r and D are adjustable parameters. $\Delta H_1^*(0)$ is the maximum value at $T = 0$ K. In such a cooperative scenario, the specific heat capacity can now be given as any sharpness to simulate the experimental data. Fig. 2.14 shows the enthalpy changes and specific heat capacity curves without and with cooperative behavior.

By introducing the cooperative excitation of lattice bonds, the specific heat capacity shapes are more reminiscent of the realistic specific heat capacity measured for fragile liquids. The two-state model with the correction of the cooperative effect provides a reasonable representation of the real physical systems behaviors. This model suggests a specific heat capacity maximum and, in extreme cases, a singularity or first-order polyamorphic transition in glass-forming liquids [62, 63, 64].

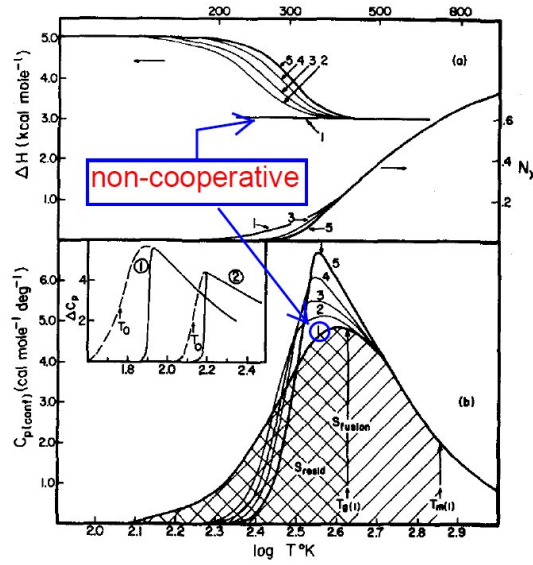


Figure 2.14: Thermodynamic properties of the two-state model with and without cooperative behaviors. Curve (1) represents a non-cooperative case and other curves (2-5) represent the cases with the cooperative effect introduced by modifying the ΔH^* as in Eq. 2.6. N_x is the mole fraction of excited bonds. The inset of (b) is the experimental data [61] of Δc_p vs. $\log T$ (taken from ref. [61]).

2.6 Energy landscape

The different fragilities of substances can be considered in the framework of the energy landscape paradigm, which is a qualitative description of the dynamic behavior of complex systems [65, 50]. In such systems, there are many metastable states that are represented by the minima of a potential energy surface. The landscape topology reflects the kinetics of the system while the average energy of the minima sampled by the system at a temperature T determines thermodynamics [66].

The energy landscape surface has $3N + 1$ dimensions for the simplest case of structureless particles [4], where N is the number of particles. For simplicity, one-dimensional representation is usually used to illustrate complex liquid systems (Fig. 2.15).

In the liquid state, the system can visit a number of minima on the energy surface determined by the temperature. With decreasing temperature, the system "falls" down in the energy landscape and can only visit lower levels of minima. Thus, less possible states are available and the entropy decreases according to the Boltzmann equation, $S = k_b \ln W$, where W is the number of the possible states (accessible minima in the energy landscape) and k_b is the Boltzmann constant. As a glass transition occurs, the system is arrested in one of the energy minima [4, 66].

The strong or fragile behavior of liquids can be explained using the potential energy landscape [65, 53]. Strong liquids are thought to have a flatter homogeneous landscape because the activation energy stays almost the same throughout the entire temperature range from melt to glass. In contrast, fragile liquids are characterized by the large deviation from the Arrhenius law and the effective activation energy changes with the temperature. Therefore, the landscape of fragile liquids are heterogeneous and the shapes of the basins vary with changing temperatures [4].

The topographic difference between the energy landscapes explains the strong and fragile behaviors in different liquid systems. Martinez and Angell [53] proposed that fragilities of liquids originate in their different vibrational heat capacities because of the different topologies of liquid landscapes. Fragile liquids have deep basins at the low temperature and the basins become shallower at higher temperatures. The vibrational excess entropy $S_{ex}(vib)$ increases rapidly above T_g due to the shallower basins. The rapidly increased vibrational entropy drives the enthalpy higher to stay at free energy minima. The rising of enthalpy enables the system to visit higher potential energy surface and more basins. This leads to more configurational entropy. In other words, the increased rate of excitation of vibrational entropy due to the shallower basins promotes the rate of increase in configurational entropy. For strong liquids, the basin shape is nearly uniform

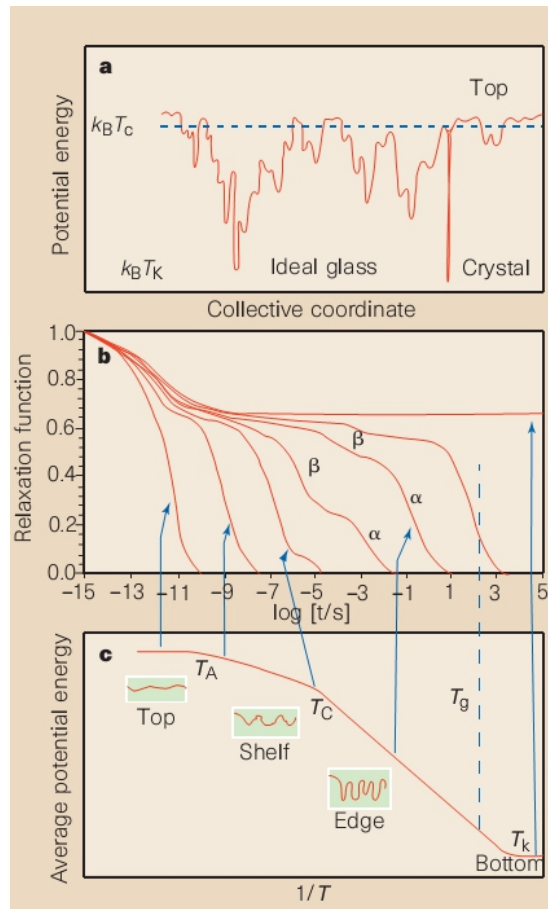


Figure 2.15: Energy landscape determines the kinetic and thermodynamic properties of liquids and glasses. **a**, The potential energy landscape is simplified as an one-dimensional surface. **b**, Relaxation functions at different temperatures. **c**, Average potential energy with the corresponding topology of the landscape (in box) (taken from ref. [66]).

and there is no such extra increase in vibrational entropy. Thus, the excess entropy of strong liquids is considered to approximate the configurational entropy; whereas the excess entropy of fragile liquids consists of the important vibrational component besides the configurational contribution [53].

2.7 Strong-fragile crossover and polyamorphic transition

In the fragility plot (Fig. 2.10), the behavior of the viscosity can be described by the VFT equation or the Adam-Gibbs equation. The fragility of a substance is an equilibrium physical property and, normally, does not depend on temperature or pressure. However, recent experimental and simulation studies revealed anomalous phenomena in the temperature dependence of viscosity (or diffusivity), which changes between non-Arrhenius and Arrhenius-like behavior with changing temperature or pressure. In other words, the fragility of a substance changes from fragile to strong. Such a kinetic transition is also known as strong-fragile (or fragile-strong) crossover.

Strong-fragile crossovers have been suggested in a number of glass-forming liquids [67, 68, 69]. The most well-known example is water. In a thermodynamic approach, Ito et al. [8] studied the anomalously small jump in excess specific heat capacity of water at T_g and showed that water is a strong liquid near T_g , although it is one of the most fragile liquids near the melting temperature, T_m . A strong-fragile transition was suggested between these two temperatures. Molecular dynamic simulations for water also showed a strong-fragile transition by calculating the diffusivities using ST2 and TIP5P models [70]. Liquid SiO_2 is a very strong glass-former. A dynamic crossover was reported above T_m using simulations [71]. A similar behavior was also reported in liquid BeF_2 [72]. Recently, in metallic glasses, a strong-fragile transition was observed directly in viscosity measurements of Vit.1 (see Fig. 2.16) and suggested for several Zr-based bulk metallic glass-forming liquids (Fig. 2.17).

It is realized that strong-fragile crossovers are related to a thermodynamic liquid-liquid (or polyamorphic) transition [67, 70]. A polyamorphic transition refers to a phase transformation between two liquid (or solid amorphous) phases having identical chemical composition but different structures and physical properties (e.g., density, entropy and kinetics). A polyamorphic transition in the stable or metastable liquid state is known as a liquid-liquid transition. The polyamorphic transition in a glassy state was first observed in water by Mishima et al. [9]. It was followed by extensive studies of the transitions between two distinct liquid states in the supercooled water [73, 8, 74]. The evidence of a liquid-liquid transition in a molecular liquid triphenyl phosphite was reported by Tanaka and

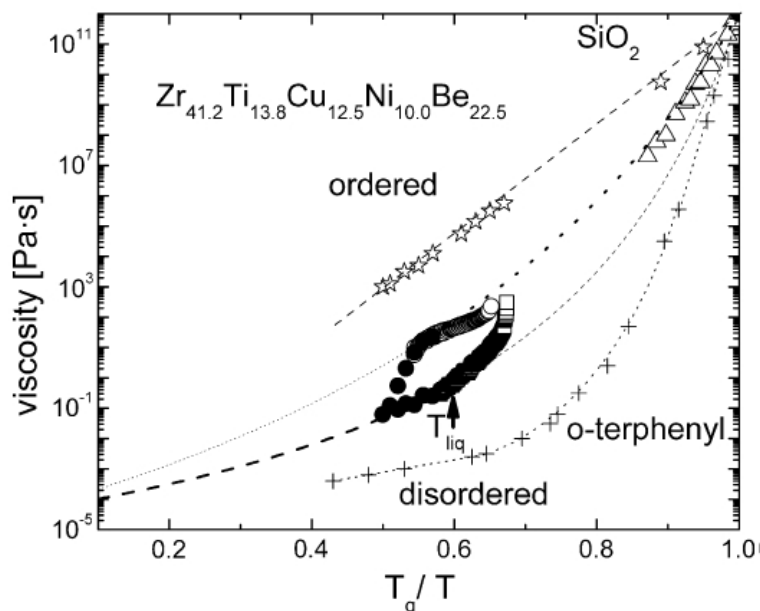


Figure 2.16: Fragility plot of the viscosity data of the bulk metallic glass-forming liquid Vit.1. The temperature dependence of viscosity exhibits a hysteresis upon the temperature. The sudden changes in viscosity on heating around 1100-1200 K ($T_g/T \sim 0.5$) and during cooling around 900 K ($T_g/T \sim 0.7$) indicate the strong-fragile crossover of the liquid dynamics. The dashed curves represent the strong and fragile liquid states characterized by the VFT equation (taken from ref. [68]).

coworkers [75]. A temperature-induced liquid-liquid transition in the supercooled liquid $\text{Y}_2\text{O}_3\text{-Al}_2\text{O}_3$ was suggested by Aasland and McMillan [76] and observed in-situ by Greaves et al. [77]. The pressure-induced polyamorphic transition in the Ce-Al metallic glasses was observed by Sheng et al. [11] and Zeng et al. [78]. In the stable liquid state, a pressure-induced liquid-liquid transition in molten phosphorus (P) was reported by Katayama et al. [79]. Using simulations, a liquid-liquid transition has been also suggested in Si [80], SiO_2 [81], BeF_2 [72], Ge [82]. A polyamorphic transition is important not only for explanations for many anomalous phenomena in liquids but also for the technological applications of glasses, because the two different amorphous (liquid) phases may have different densities, local structures, thermodynamic, rheological properties, electronic conductivities and mechanical properties. However, the polyamorphic transition and even its very existence have been much debated due to crystallization problems that hamper experiments performed in the desired supercooled regime, or the transition is located at high temperatures or pressures beyond the experimentally accessible range.

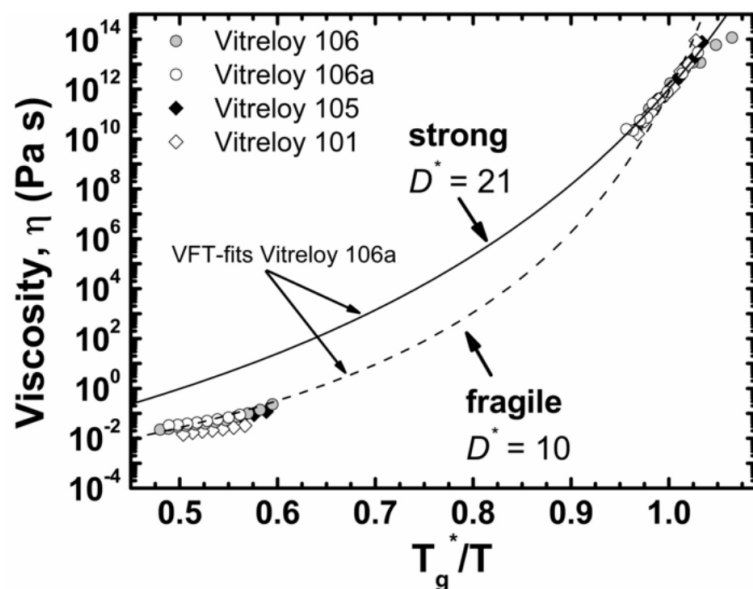


Figure 2.17: Viscosity discrepancy of Zr-based bulk metallic glass-forming liquids over the entire temperature range. The low-temperature equilibrium viscosities were measured isothermally using three-point beam-bending. The high-temperature viscosities were measured in a Couette viscometer. The VFT fits to high and low temperature data give different fragility parameters D^* . This discrepancy suggests a strong-fragile transition to occur in the supercooled liquid region. For example, Vit.106a has a stronger kinetics with $D^* = 21$ in the vicinity of T_g ; whereas it exhibits fragile behavior above the liquidus temperature with $D^* = 10$ (taken from ref. [69]).

Evidence from experiments and simulations

In the following, important experimental observations and results from simulations for a few polyamorphic systems are briefly reviewed.

Water

Mishima and coworkers [9] show that by increasing the temperature at ambient pressure, a low-density amorphous water can be obtained. By compression at lower temperature, the high-density amorphous water is achieved. The results are supported by molecular dynamic simulations using ST2 pair potential [83]. When the high and low density states of amorphous water are projected on the liquid states, water has two different liquid forms, the high- and low-density phases.

Figure 2.18 shows the P – T phase diagram of water based on experimental and

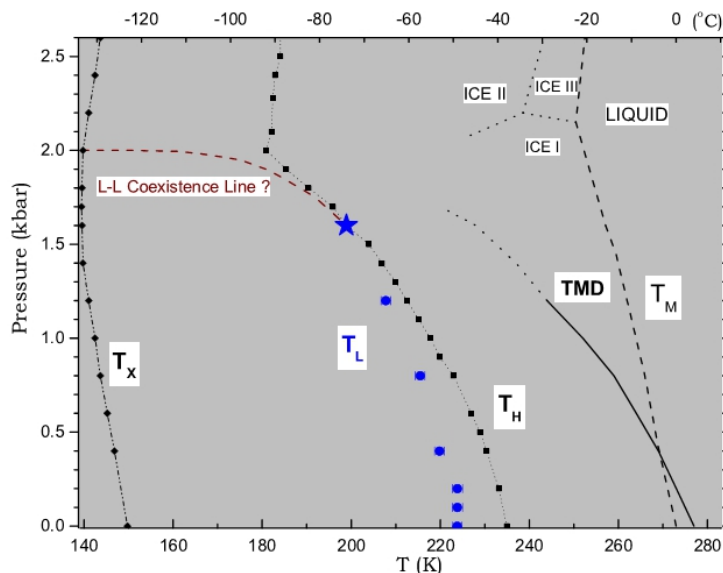


Figure 2.18: Water’s P-T phase diagram (reproduced from ref. [84]). The solid blue dots represent the strong-fragile transition at T_L . The homogeneous nucleation temperature is denoted as T_H and crystallization temperature is T_x . TMD indicates the temperature with maximum density. The dashed line from the hypothesized liquid-liquid critical point (star symbol) is the assumed coexistence line.

simulation results [84]. Below the melting temperature (T_m) line, there is a liquid-liquid critical point (star symbol) in the supercooled liquid region. At the critical point, the two liquid phases become identical. The liquid-liquid coexistence line has a negative slope above the critical pressure. Below the critical pressure, the blue dots indicate the occurrence of the strong-fragile transition, which was found by Xu et al. [70] to be associated with the so-called Widom line, which is an extension of the liquid-liquid coexistence line beyond the critical point. Moreover, the results of the simulation showed that the specific heat capacity exhibits a maximum when crossing the Widom line.

Silica (SiO_2)

SiO_2 has a high glass transition temperature, T_g , of 1470 K. It is therefore difficult to experimentally study the liquid SiO_2 in a wide temperature range above T_g . Thus, molecular dynamic simulations are often employed to explore the possible liquid-liquid critical point in the SiO_2 system. The Woodcock-Angell-Cheeseman (WAC) [85] and Beest-Kramer-Santen (BKS) potentials [86] are commonly used for SiO_2 . The simulation results from Saika-Voivod et al. suggest that there exists a critical point at 4000 K for the WAC system and 2000 K for the BKS

system [81]. In a very recent study of the WAC system, Hemmati and Angell [56] pinpointed the critical point by observing the flattening of the pressure-volume isotherm profiles, which are located at $T_c = 3500 - 4000$ K and $P_c = 6.5$ GPa. The authors showed two different shapes of specific heat capacities during the glass transitions. At ambient pressure, the specific heat capacity jump at T_g of SiO_2 is small. In contrast, the high-pressure SiO_2 liquid displays a large specific heat capacity jump at T_g which has the characteristic shape of the specific heat capacity of fragile liquids [56]. This observation is in accordance with the transport properties studies on the strong-fragile crossover of simulated SiO_2 at ambient pressure. These studies showed that the strong SiO_2 liquid becomes fragile at high pressure and high temperature. The liquid-liquid transition of SiO_2 may be encountered in reality when the silica glass optical fiber suffers a failure phenomenon called "optical fuse", [56] where the temperature and pressure may reach temperatures and pressures above 5500 K and 7 GPa, respectively, in the region, in which a liquid-liquid transition is expected to happen. The studies on the phenomenon of optical fuse of silica glasses may bring further insight into the liquid-liquid transition of SiO_2 [56].

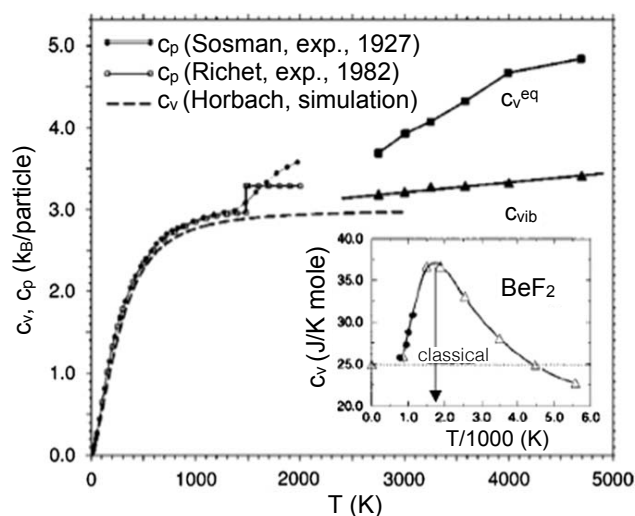


Figure 2.19: The specific heat capacity data of amorphous (or liquid) SiO_2 (main panel) and amorphous (or liquid) BeF_2 (Inset) obtained from experiments and simulations. The simulation data show specific heat capacity maxima at high temperature around 5000 K for SiO_2 [87] and at around 2000 K for BeF_2 (taken from ref. [7, 72]).

BeF₂

Hemmati et al. [72] carried out ion dynamics simulation of BeF₂ and obtained diffusivity data, which showed a highly anomalous fragile region just above the experimentally accessible temperature range. A rising of the specific heat capacity above T_g was observed in experiments (see inset of Fig. 2.19). A specific heat capacity maximum at around 2000 K was found using simulations, which suggested a continuous liquid-liquid transition, similar to the case of liquid SiO₂.

Silicon (Si)

McMillan et al. [88, 89] show experimental evidence for the existence of a density-driven polyamorphic transition between two different forms of solid amorphous silicon. The authors performed molecular dynamics simulations with the Stillinger-Weber potential and the behavior of the polyamorphic transition of solid is mapped onto a first-order low-density liquid (LDL)/high-density liquid (HDL) phase transition in the supercooled liquid state.

They load the amorphous silicon samples into a diamond anvil cell (DAC) using argon as a pressurization medium. During the compression and decompression, the electrical resistance and the Raman spectra are measured simultaneously. A large resistivity hysteresis is observed during several pressure cycles, as shown in Fig. 2.20 [88]. With increasing pressure, there is a sudden drop of resistivity around 10-12 GPa, indicating a transformation from low-density amorphous (LDA) to high-density amorphous (HDA) phase. During decompression, the resistivity retains its low value until the reverse transition from the HDA to LDA state around 4-5 GPa. A similar hysteresis is also observed in the Raman spectra. Both observations strongly suggest the existence of a first-order polyamorphic phase transition.

Using a two-state model, the MD simulations determine the liquid-liquid transition coexistence line for Si (see Fig. 2.21), which terminates at a liquid-liquid critical point at $P = 1$ atm and $T = 1060$ K. The spinodal boundaries for the first-order liquid-liquid transition are calculated (green curves), indicating the mechanical stability limits of the LDL and HDL phases. In the region between the two spinodal lines, the liquid phase is metastable with respect to the other. Thus, the triggering pressure to transform into the other phase can be different during compression and decompression. This is why a large hysteresis was observed in the experiments (see Fig. 2.20).

Y₂O₃-Al₂O₃

Greaves et al. [77] report a liquid-liquid transition in the multicomponent system Y₂O₃-Al₂O₃. Although a chemical decomposition could occur, the dominant

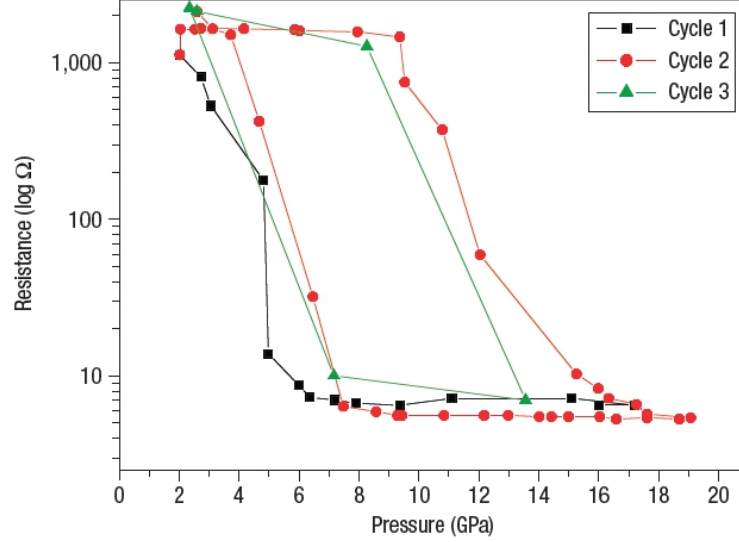


Figure 2.20: Electrical resistance of amorphous Si measured during pressure cycles in the DAC. The large hysteresis of the resistance indicates the polyamorphic transition between a high-density and a low-density amorphous phase (taken from ref. [88]).

order parameters for the liquid-liquid transition are density and entropy of the liquid. Both liquids coexist and can be quenched into the glassy state. They show a demixing of the liquid on the nanoscale as revealed by small angle X-ray scattering (SAXS) and the related reversible shifts in polyhedral packing on the atomic length scale using wide angle X-ray scattering (WAXS). The authors claimed that the yttria-alumina melt undergoes a first-order liquid-liquid transition in the supercooled region with an underlying critical point at $T_{LL}^c=1804$ K and $P_{LL}^c = -0.31$ GPa. The reported entropy change for the liquid-liquid transition is around $19 \text{ J mol}^{-1} \text{ K}^{-1}$, which is about half of the entropy of fusion.

Ce-Al

In amorphous alloys, using in-situ X-ray diffractions, a pressure-induced transition occurs between two distinct amorphous phases in $\text{Ce}_{55}\text{Al}_{45}$ and $\text{Ce}_{75}\text{Al}_{25}$ metallic glasses [11, 78]. An abrupt change of the first diffraction peak position Q_1 of $\text{Ce}_{55}\text{Al}_{45}$ was observed during decompression, as shown in Fig. 2.22, indicating a transformation from a high-density state with shortened Ce-Ce bonds to a low-density state with lengthened Ce-Ce bonds. These pressure-induced polyamorphisms were attributed to the f-electron localization or delocalization, which leads to the length change in the nearest Ce-Ce bonds.

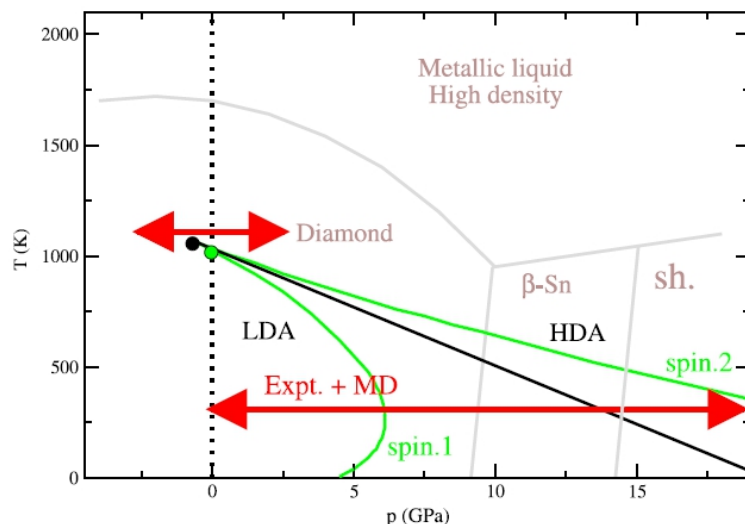


Figure 2.21: Temperature-pressure metastable phase diagram for supercooled silicon. The liquid-liquid transition coexistence line (solid black line) is calculated using a two-state (excitation) model. The liquid-liquid critical point is determined at $T_c = 1060$ K and $P_c = -1$ GPa. The two spinodal lines illustrate the limits of the stability of the LDL (spin 1) and HDL (spin 2) phases. The red arrow at $T = 300$ K shows the isotherm path of the resistivity experiments and simulations carried out by McMillan et al. (taken from ref. [89]).

Liquid-liquid transitions and two-state models

Density- or entropy-driven liquid-liquid transitions have been predicted from two-state models. A two-state model was first proposed from the analysis of anomalous melting curves of some substances including water. In general, the entropy of a system increases upon melting (i.e., $\Delta S_m > 0$). The corresponding volume is usually expected to increase as well ($\Delta V_m > 0$). According to the Clausius-Clapeyron relation,

$$\frac{dT_m}{dP} = \frac{\Delta V_m}{\Delta S_m}, \quad (2.8)$$

the melting curve (dT_m/dP) has a positive slope. Although positive melting curves are found in most systems, there are some systems, for example, water, that were observed to have negative initial melting slopes. It is well-known that liquid water is more dense than crystalline solid water ($\Delta V_m < 0$). Rapoport [90] suggested that liquid water might contain distinct structural states or domains, depending upon the presence or absence of H-bonding between the H_2O molecules. High-density densely packed and low-density loosely packed domains were assumed to exist in the liquid. The two kinds of domains inter-convert

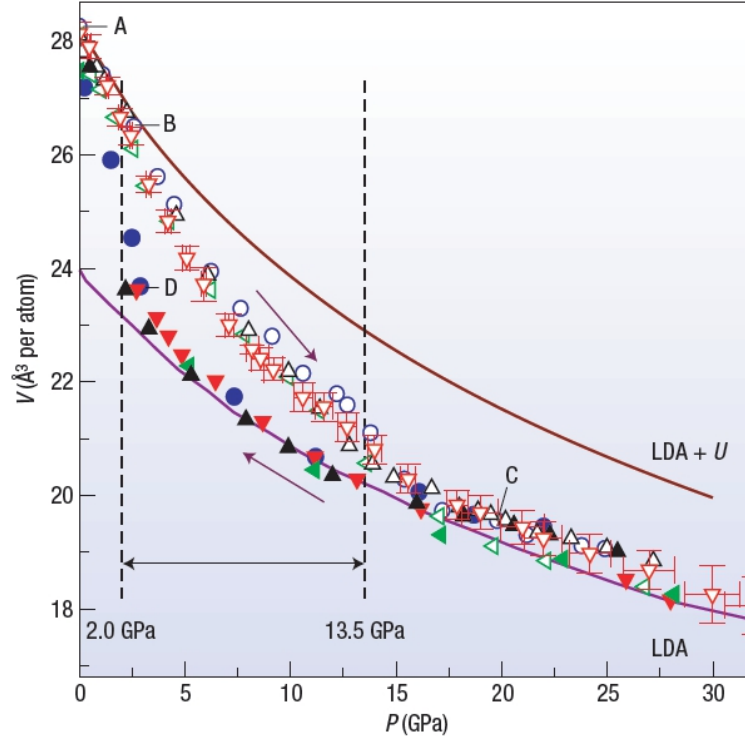


Figure 2.22: Specific volume vs. pressure for amorphous $\text{Ce}_{55}\text{Al}_{45}$. The solid symbols represent the data obtained during decompression and open symbols are compression. There is an abrupt change during the decompression process. The volume hysteresis indicates a polyamorphic transition driven by pressure (taken from ref. [11]).

rapidly, but the averaged proportion stays stable at a constant pressure and a constant temperature. With changing pressures or temperatures, the relative proportion of the domains changes due to intermolecular bonding changes. In some circumstances, the liquid has a higher density than the corresponding crystal. This two-domain or two-state model explains why the melting curve of liquid water has a maximum. The two-state model was also applied on other systems with a negative melting curve ($dT_m/dP < 0$). In the two-state model, the high-density domain and low-density domain may contribute to the Gibbs free energy due to mixing. Applying the regular solution mixing model, the overall Gibbs free energy for the mixing of a high-density liquid (A) and a low-density liquid (B) is,

$$G = X_A G_A + X_B G_B, \quad (2.9)$$

where X_i is the molar fraction of liquid i and G_i is the Gibbs free energy for liquid i , which is defined in terms of the specific volume contribution,

$$G_A = G_A^0 + V_A^0(P - P_0) + RT \ln X_A + W(1 - X_A)^2 \quad (2.10)$$

$$G_B = G_B^0 + V_B^0(P - P_0) + RT \ln X_B + W(1 - X_B)^2 \quad (2.11)$$

where G_i^0 is the standard state molar free energy associated with the liquid i . V_i^0 is the standard state molar volume and P_0 is the standard state molar pressure. R is the gas constant. W is the regular solution interaction parameter associated with the contribution of enthalpy of mixing of two liquids. Then, the excess Gibbs energy of mixing for a two-state liquid is

$$\Delta G_{mix} = RT[X_A \ln X_A + (1 - X_A) \ln(1 - X_A)] + P[X_A V_A + (1 - X_A) V_B] + X_A(1 - X_A)W. \quad (2.12)$$

When $W/kT > 2$, the ΔG_{mix} develops double minima. In the two-state model, the double minima correspond to the same chemical composition but different densities or entropies. So, the liquid can separate into a high-density liquid phase and a low-density liquid phase in the coexistence region of polyamorphic liquids. This two-state model results in a "critical point" and a line of a first-order liquid-liquid transition in the $P - T$ phase diagram [91].

Angell and Moynihan [64] proposed a bond-lattice excitation model, which is similar to the two-state model to explain the polyamorphic behavior of glass-forming liquids. They treat the liquid structure using weakly interacting lattice bonds. The excitations of the liquid are described as the temperature-induced bonds breaking or excitations. Then the liquid can have two species: the excited state and the ground state. The mixing of two states is treated with the regular solution mixing model like the formulism described above. With increasing temperature, more and more lattice bonds are excited. When the excitations of bond-lattice are cooperative, the excitation of liquids can lead to a critical or first-order liquid-liquid transition between two liquids with different excited states.

On one hand, the critical temperature of the liquid-liquid transition depends on the excitation enthalpy and the excitation entropy, more precisely, the ratio of $\Delta H^*/\Delta S^*$. On the other hand, the fragility of a liquid is determined by the excitation entropy ΔS^* . If the cooperative excitation is small, the excitation entropy is small and the liquid is strong. In contrast, more cooperative excitations give raise to a larger excitation entropy and the liquid is fragile [64]. This gives a plausible explanation for why liquid-liquid transitions for SiO_2 and BeF_2 happen above T_m but for water, Si and Ge they are below T_m .

SiO_2 and BeF_2 are strong liquids with less cooperative excitations and small excitation entropies. Therefore, they have the transitions at high temperatures

above the melting point [71, 72]. In the cases of more fragile liquid Si and Ge, the bond-breaking processes are much more cooperative than in SiO_2 and BeF_2 due to lack of network bridges in Si and Ge. Therefore, the excitation entropies are large and the liquid-liquid transitions of Si and Ge are located in the supercooled liquid region being close to glass transitions [80, 82].

2.8 The liquid-liquid critical point

The liquid-liquid critical point (LLCP) is proposed to be the origin of liquid-liquid transitions and the strong-fragile crossovers. A critical point in a pressure-temperature (P - T) diagram is the point where all physical properties of two phases become identical. For example, by changing pressure and/or temperature to reach the liquid-gas critical point, the liquid and its vapor cannot be distinguished anymore. The phase transition at a critical point is a continuous second order transition rather than a first-order transition. These second order transitions include, e.g., transitions from ferro-magnetism to para-magnetism, and the order-disorder transition in $\text{Fe}_{50}\text{Co}_{50}$. Near a critical point, phase transitions show anomalies, usually called critical phenomena, which are related to the occurrences of very large fluctuations in the system when one approaches the critical point. The large fluctuations of density, energy, magnetization are reflected by the maxima in thermodynamic derivatives (e.g., compressibility, heat capacities and susceptibilities). The LLCP is a critical point in the liquid state. As crossing the LLCP, a continuous liquid-liquid transition occurs between two liquid phases having the same composition but with different structures and properties. Such a LLCP is assumed to underly the anomalies in water, SiO_2 , Si, BeF_2 and $\text{Y}_2\text{O}_3\text{-Al}_2\text{O}_3$.

The Jagla model

The liquid-liquid transition behavior can be described by the simple Jagla model, which assumes that the particles interact via a spherical and symmetric two-scale potential with both repulsive and attractive ramps, as shown in Fig. 2.23a. The Jagla model possesses a liquid-liquid critical point (see the black dots in Fig. 2.24). The two liquid phases are separated by the first-order transition (the coexistence line in $P-T$ phase diagram), terminating at the critical point. Along the extension of the liquid-liquid coexistence line beyond the critical point, there is the Widom line, the loci of the maximum correlation length and c_p maxima. When crossing the Widom line, a continuous transition occurs. The two liquid phases involved in the liquid-liquid phase transition have rather different physical properties. In the low-temperature phase, the liquid is strong as the diffusivity

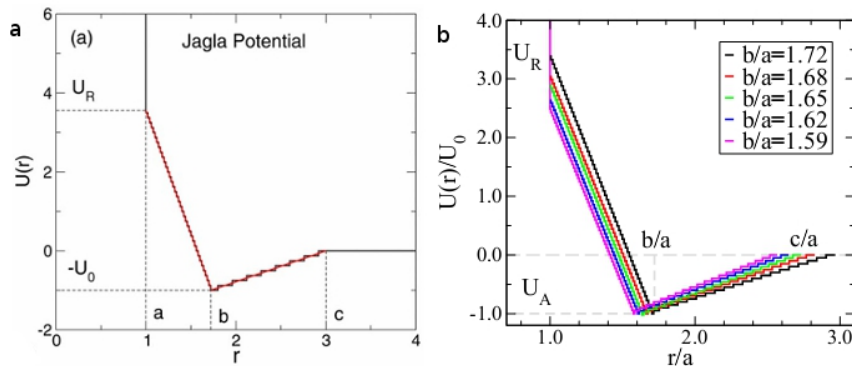


Figure 2.23: (a) Two-length-scale Jagla potential with a hard core diameter $r = a$, a soft core diameter $r = b$ and a long range cutoff $r = c$ (taken from ref. [92]). (b) Modified Jagla potentials with different $b/a, c/a$ ratios and varying hard core potentials U_R (taken from ref. [93]).

follows closely the Arrhenius law. The high-temperature phase is fragile as the diffusivity deviates much from the Arrhenius law. Such a dynamic strong-fragile crossover is, as discussed earlier, seen in water, SiO_2 and BeF_2 . Note that the coexistence line for water has a negative slope which is opposite to the positive slope for the Jagla model.

When the Widom line is crossed in the phase diagram, a c_p maximum is found in simulations, indicating a continuous transition, which is correlated with the strong-fragile crossover found in diffusivity simulations [70, 92]. The specific heat capacity peak for the continuous transition is very sharp and displays a lambda-like shape when the system is close to the critical point. With increasing pressure, the system departs from its critical point and, therefore, the specific heat capacity peak becomes smeared out. The specific heat capacity behavior predicted from this model is analogous with the specific heat capacity maxima found in the simulations and experiments of SiO_2 [87] and BeF_2 [72]. Both have smeared out c_p maxima as well as a strong-fragile crossover, located above T_m .

The coexistence line of a liquid-liquid phase transition can have a positive, zero, or negative slope, depending on how the parameters are selected for the Jagla model. Luo et al. [93] modified the Jagla model to investigate response functions near the LLCP as coexistence lines change slopes from positive to zero. The authors studied various Jagla potentials with different parameters, as shown in Fig. 2.23b. By changing the hard-core distance $r = a$, soft-core distance $r = b$ and the long range cutoff $r = c$, they found that the LLCP shifts to lower temperatures and higher pressures. The slopes of the liquid-liquid phase transition coexistence lines decrease from positive to almost zero, as the ratio b/a decreases from 1.72 to 1.59. Simultaneously, the specific heat capacity can be

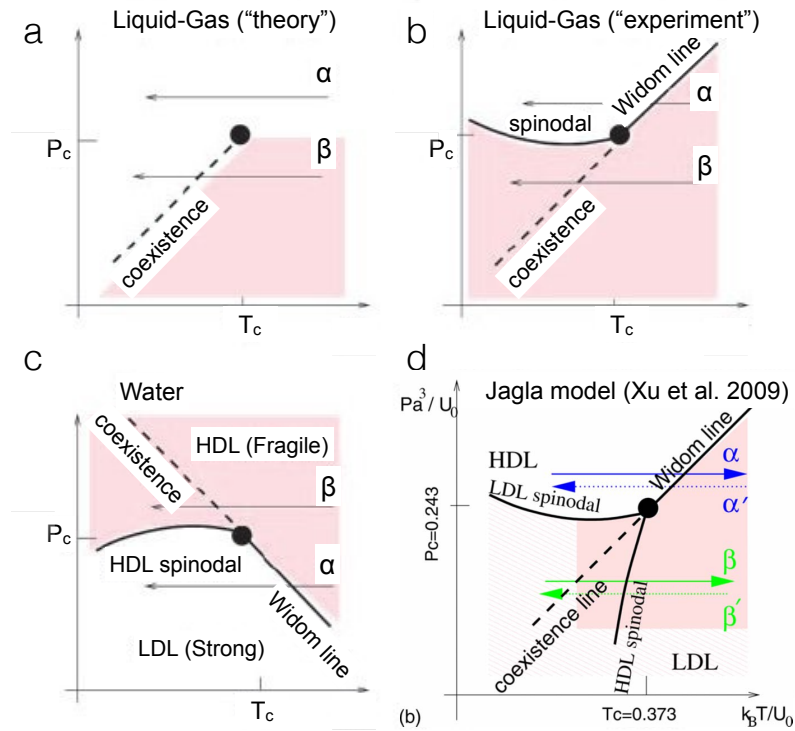


Figure 2.24: Schematic $P - T$ phase diagrams for the liquid-gas (a, b), the simulated water (c) and the Jagla model (d). At the liquid-gas critical point (a,b), the liquid and gas become identical. When crossing the coexistence line, a first-order liquid-gas transition occurs, which can be also considered as a polyamorphic transition. The phase diagram for water (c) has a negative slope of the coexistence line, while the Jagla model (d) has a positive slope of the coexistence line. A so-called Widom line is defined by the locus of the maximum heat capacity beyond the critical point. These lines with the critical point separate the liquid into the low-temperature strong liquid and the high-temperature fragile liquid with different density or entropy. HDL and LDL stand for the high and low density liquid. A spinodal line represents the locus of the metastable limit of one liquid phase (taken from ref. [70, 92]).

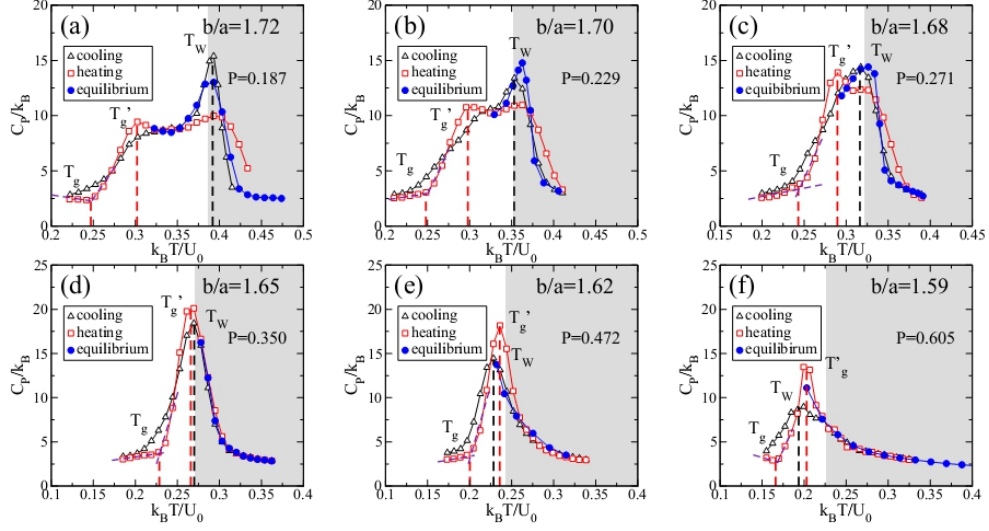


Figure 2.25: Heat capacity peaks of liquid-liquid transitions and glass transitions in the Jagla model. (a-f) show the changes of c_p peak shapes with decreasing Jagla potential distances, b/a (taken from ref. [93]).

calculated along an isobaric path at pressures slightly above P_c . In Fig. 2.25, a comparison of c_p upon cooling and heating at the same rate for different b/a ratios is shown. There are two c_p peaks. The low-temperature peak corresponds to the glass transition zone marked by T_g and T'_g . The high-temperature peak at T_W corresponds to the crossing of Widom line that originates from the LLC. It was noticed that when b/a decreases, the c_p peak of Widom line is pushed to lower temperature and closer to T_g . For $b/a \leq 1.65$, the two peaks overlap and only one peak of the glass transition is observable. It is also noted that the specific heat capacity maxima of the liquid-liquid transition become less pronounced with decreasing slopes of the coexistence lines.

Luo et al.'s study [93] shows that the c_p maxima near the LLC can be readily observed only when the slope of the coexistence line is strongly positive or negative, as shown in the case of Fig. 2.26a. For the slope close to zero (Fig. 2.26b), the the specific heat capacity maximum cannot be observed before glass transition or crystallization because the difference in enthalpy ΔH between LDL and HDL is zero when the coexistence line is horizontal, according to the Clausius-Clapeyron equation, $dP/dT = \Delta H/(T\Delta V)$. In this case, only the density change (or compressibility K_T) is the dominant term in the liquid phase change.

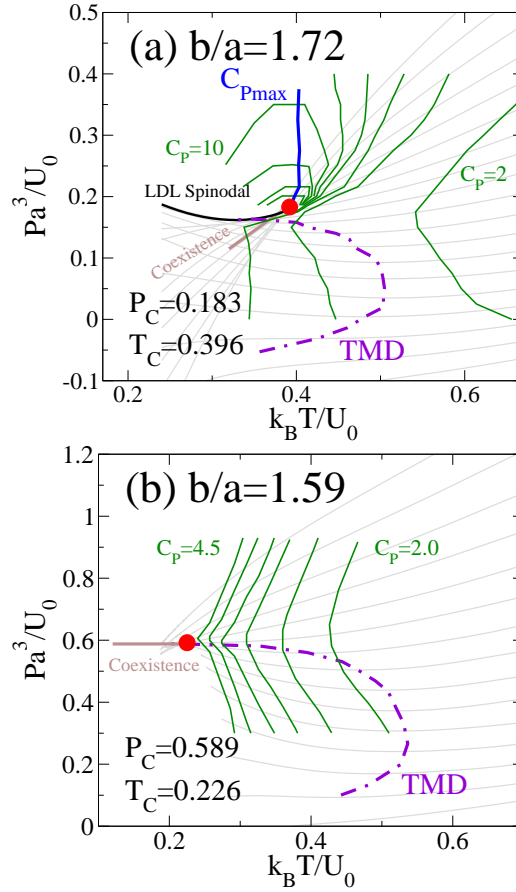


Figure 2.26: (a) Phase diagram with specific heat capacity C_p for positively sloped coexistence line case ($b/a = 1.72$). Solid dot is the LLCPC. The lines of equal C_p (solid green) change from $C_p = 2$ far away from the LLCPC to $C_p = 10$ close to the LLCPC. The C_p maximum is observed at the blue line in the supercritical region. TMD is the temperature of maximum density. (b) The case of the horizontal coexistence line ($b/a = 1.59$). No C_p maximum can be observed before the glass transition or crystallization. (taken from ref. [93]).

Chapter 3

Materials and methods

3.1 Samples preparations

Crystalline $\text{Fe}_{50}\text{Co}_{50}$ and $(\text{FeCo})_{100-x}\text{Al}_x$ alloys were prepared by arc melting of the elemental metals with purities ranging from 99.99% to 99.999%. The alloys were subsequently re-melted in an arc melter in a copper water-chill mold under high-purity argon and cast in the form of cylinders, that have a diameter of 5 mm and a length of about 20 mm. The as-cast cylinders were cut into 1.2 mm thick disks for the calorimetric measurements.

The master alloy of the $\text{Zr}_{58.5}\text{Cu}_{15.6}\text{Ni}_{12.8}\text{Al}_{10.3}\text{Nb}_{2.8}$ (Vit.106a) was prepared by arc-melting elements with purities ranging from 99.9 to 99.999 at. % under a high-purity argon, Ti-gettered atmosphere. Then the master alloy was re-melted in an arc melter and suction cast into a water-cooled copper mold to form the amorphous rods.

Amorphous $\text{Au}_{49}\text{Cu}_{26.9}\text{Si}_{16.3}\text{Ag}_{5.5}\text{Pd}_{2.3}$ was prepared by first inductively heating the pure elements in an Al_2O_3 crucible inside of a high-purity argon-flushed atmosphere and tilt-casting into a water-cooled copper mold. The $\text{Pd}_{43}\text{Ni}_{10}\text{Cu}_{27}\text{P}_{20}$ alloy was prepared by arc-melting the mixture of the high-purity elements. The alloy was subsequently melted in evacuated quartz tubes with an induction furnace and quenched in water to obtain amorphous samples. Boron oxide was added into the quartz tube as a flux to retard crystallization.

Fully amorphous $\text{Zr}_{41.2}\text{Ti}_{13.8}\text{Cu}_{12.5}\text{Ni}_{10}\text{Be}_{22.5}$ (Vit.1), $\text{Zr}_{44}\text{Ti}_{11}\text{Ni}_{10}\text{Cu}_{10}\text{Be}_{25}$ (Vit.1b) and $\text{Zr}_{46.75}\text{Ti}_{8.25}\text{Cu}_{7.5}\text{Ni}_{10}\text{Be}_{27.5}$ (Vit.4) were supplied by Liquidmetal©Technologies. Amorphous B_2O_3 and GeO_2 was made by heating crystalline samples from Alfa Aesar© well above their respective melting points and cooling with a fast cooling rate ($\sim 50 \text{ K min}^{-1}$) in air in a Differential Thermal Analyser (DTA) (NETZSCH STA 449C) furnace.

The sample rods were cut into disks with a mass of about 60 mg to ensure good signals obtained from the calorimeter. For experiments in an electrostatic

levitator, the Vit.1 samples were re-melted in the arc melter to form spherical samples with the mass around 60 mg.

3.2 Measurements of thermodynamic and kinetic properties

The measurement of changes of heat flow during a process is known as the *calorimetric* method. Important thermodynamic quantities such as specific heat capacity and enthalpy as well as kinetic properties like relaxation times can be determined using calorimetry. Differential Scanning Calorimetry (DSC) and DTA are the most commonly used calorimetric methods. The power compensation DSC is the most advanced technique to measure the heat changes quantitatively with a high accuracy. A DTA measures the temperature difference between a sample and a reference as a function of time or temperature, which is used to determine the heat being exchanged qualitatively. A DTA is usually used as a qualitative technique for the identification of a phase transition or a chemical reaction. In the present work, the calorimetric studies were carried out using the power compensation Perkin-Elmer Diamond DSC and Netzsch STA 449/C/6/MFC/G Jupiter.

3.2.1 Differential Scanning Calorimeter (DSC)

The power compensation of the DSC features two DSC furnaces. A sample and a reference are separately placed in two furnaces and each has an individual heater and temperature sensor (Fig. 3.1). When a temperature difference evolves between the sample and the reference, a differential electrical power is provided to the heaters to eliminate the temperature difference and keep the sample temperature at the program value. Thus, the DSC output is the differential thermal power [94].

The DSC output signals of a power compensated DSC are the heat flows between the sample and the thermal energy source, denoted as $\dot{Q} = dQ/dt$. Gray [95] derived an equation for the DSC heat flow

$$dQ/dt = -dh/dt + (C_s - C_r)dT/dt - RC_s d^2Q/dt^2, \quad (3.1)$$

where dh/dt is the heat evolution from chemical reactions of the sample and $dh/dt = 0$ for the inert sample. The second term is the heat capacity displacement $(C_s - C_r)dT/dt$, in which C_s is the heat capacity of the sample and its crucible; C_r is the heat capacity of the reference and its crucible; and dT/dt is the heating rate. The second term is the basis of determination of heat capacity. The last

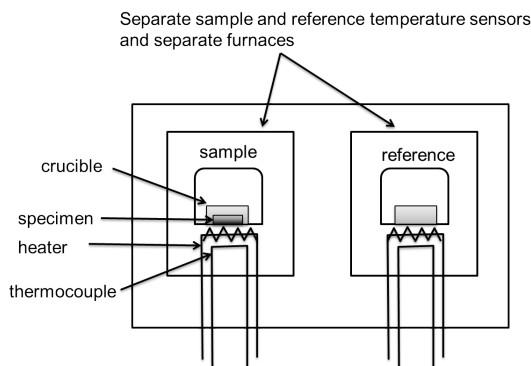


Figure 3.1: Sketch of the furnaces of the power compensation DSC.

term $RC_s d^2Q/dt^2$ represents a thermal lag, in which R is the thermal impedance between the sample and the heat source and between the reference and the heat source. The thermal lag should be reduced as much as possible, for example, by using a thin sample, better contact between the sample and the crucible, and slow heating rates. In a real experiment, the correct heat flow has the relation with the experimental heat flow [95]

$$dQ/dt = \kappa(dQ/dt)_{exp}, \quad (3.2)$$

where κ is the calibration constant. Assuming that the crucibles are identical for the sample and the reference, $C_r = 0$ when using an empty crucible as the reference. Then, the heat capacity of the sample is [95]

$$C_s(dT/dt) = \kappa(dQ/dt)_{exp} + RC_s d^2Q/dt^2. \quad (3.3)$$

It is seen that the experimental value of the DSC thermal signal divided by the heating rate, $(dQ/dt)_{exp}/(dT/dt)$, is proportional to the heat capacity of the sample, C_s , when the thermal lag can be ignored [95].

3.2.2 Measurement of the kinetics of the glass transition

The kinetic properties of the glass transition can be determined using a DSC. The behavior of the glass transition upon upscans depends on the thermal history. Therefore, a controlled down-scan from the supercooled liquid region is performed with a selected cooling rate before an up-scan is carried out with the same heating rate. Such a up-scan allows to determine the onset of the glass transition, T_g^{onset} , as the glass transition temperature T_g , which is approximately equal to the fictive temperature T_f for the glassy state from the cooling rate [3]. The structural relaxation time τ at T_g can be defined by the glass transition width $\Delta T_g = T_g^{end} - T_g^{onset}$ divided by the heating/cooling rate $q_h = q_c$ [96]

$$\tau = \frac{\Delta T_g}{q_h}. \quad (3.4)$$

The temperature dependence of the structural relaxation time τ can be described by the VFT equation ($\tau = \tau_0 \exp(D^*T_0/(T - T_0))$). A data fit of the relaxation times yields the VFT fragility parameter, D^* , that indicates the deviation of dynamics from the Arrhenius law. Evenson et al. [97] showed that the kinetic fragility determined by the above method is consistent with the values obtained from viscosity measurements.

Alternatively, the cooling rate dependence of the fictive temperatures, T_f , can be determined with the method of Wang et al. [98] and the fragility steepness index m can be derived. An amorphous sample is cooled from the supercooled liquid region at various cooling rates, q_c . A subsequent up-scan is carried out at a fixed heating rate of 20 K min⁻¹ after the previous cooling treatment. Using the area matching method [98], the fictive temperature can be determined for each cooling rate. Then, the scaled cooling rates are plotted against the scaled fictive temperatures and the value of m is obtained from the slope of the fitted linear function given by Wang et al. [98]

$$\log\left(\frac{q_c}{q_c^s}\right) = m - m\frac{T_f^s}{T_f}, \quad (3.5)$$

where the standard cooling rate is $q_c^s = 20$ K min⁻¹ and the standard fictive temperature T_f^s is the fictive temperature measured with the standard cooling rate.

3.2.3 Measurement of high-precision heat capacity

High-precision values of specific heat capacity below 1000 K are determined using DSC in reference to the specific heat capacity of a standard sapphire with step-wise heating of the sample. The sample is sealed in a sample container (pan) and heated up in steps of 20 K at 0.333 K s⁻¹ and hold isothermally 180 s for every step from room temperature to the desired temperature below the upper limit of 1000 K in the DSC. The same procedure is followed by the measurement of the same empty gold pan as well as the standard sapphire. The specific heat capacity c_p is calculated according to the following equation [96]

$$c_p(T)_{\text{sample}} = \frac{\dot{Q}_{\text{sample}}^{\text{step}}}{\dot{Q}_{\text{sapphire}}^{\text{step}}} \cdot \frac{m_{\text{sapphire}} \cdot \mu_{\text{sample}}}{\mu_{\text{sapphire}} \cdot m_{\text{sample}}} \cdot c_p(T)_{\text{sapphire}}, \quad (3.6)$$

where m is the mass, μ the atomic weight. $c_p(T)_{\text{sapphire}}$ is the standard value of the specific heat capacity of sapphire, given by the literature. $\dot{Q}_{\text{sample}}^{\text{step}}$ and $\dot{Q}_{\text{sapphire}}^{\text{step}}$

(mW) are the changes in heat flow corresponding to each step of increase in temperature, which can be obtained by the equations

$$\dot{Q}_{sample}^{step} = (\dot{Q}_{sample\&pan} - \dot{Q}_{pan})_{\dot{T} \neq 0} - (\dot{Q}_{sample\&pan} - \dot{Q}_{pan})_{\dot{T} = 0} \quad (3.7)$$

and

$$\dot{Q}_{sapphire}^{step} = (\dot{Q}_{sapphire\&pan} - \dot{Q}_{pan})_{\dot{T} \neq 0} - (\dot{Q}_{sapphire\&pan} - \dot{Q}_{pan})_{\dot{T} = 0}. \quad (3.8)$$

$(\dot{Q}_{sample\&pan} - \dot{Q}_{pan})_{\dot{T} \neq 0}$ is the power that is needed to heat the sample to a certain temperature. $(\dot{Q}_{sample\&pan} - \dot{Q}_{pan})_{\dot{T} = 0}$ is the power to keep the sample at a constant temperature [96]. Likewise, $(\dot{Q}_{sapphire\&pan} - \dot{Q}_{pan})_{\dot{T} \neq 0}$ is the power that is needed to heat the sapphire to a certain temperature. $(\dot{Q}_{sapphire\&pan} - \dot{Q}_{pan})_{\dot{T} = 0}$ is the power to keep the sapphire at a constant temperature. Therefore, for each temperature step, we obtain a \dot{Q}_{sample}^{step} and a $\dot{Q}_{sapphire}^{step}$, respectively. As a result, the $c_p(T)_{sample}$ can be calculated according to Eq. 3.6.

The specific heat capacity of Fe₅₀Co₅₀ (Chapter 4) on a long time scale below the calorimetric glass transition is determined by long time enthalpy relaxation and recovery experiments [99]. The as-cast sample, with a mass of about 40-120 mg, is heated up at a rate of 1 K s⁻¹ to 1000 K (the upper limit of the DSC) and cooled at 1 K s⁻¹. This treatment is performed for each sample to ensure the same initial enthalpy state. Then, the sample is heated at a rate of 0.025 K s⁻¹ to a selected temperature below T_g and held isothermally for a certain time to allow a complete relaxation. After isothermal annealing the sample is cooled and subsequently re-heated at a constant heating rate of 1 K s⁻¹ up to 1000 K. During the up-scan the recovered enthalpy is measured, that is equal to the previously released enthalpy during relaxation. Likewise, isothermal annealing is performed at different temperatures and the corresponding enthalpy relaxation can be determined. Next, the released enthalpies are converted into the specific heat capacity difference between the frozen-in state and the relaxed state [99]. Accordingly, the heat capacity on a long time scale can be calculated using the converted heat capacity difference and the measured frozen-in heat capacity. The long timescale specific heat capacity is equal to the heat capacity in the equilibrium state, when the sample would be cooled with a very small rate.

3.2.4 Differential Thermal Analyzer (DTA)

In contrast to DSC, the signal of a DTA is proportional to the temperature difference between the sample and an inert reference which are both subjected to the same temperature program. A single furnace with separate temperature sensors is used in the DTA (see Fig. 3.2). A modern quantitative DTA has a

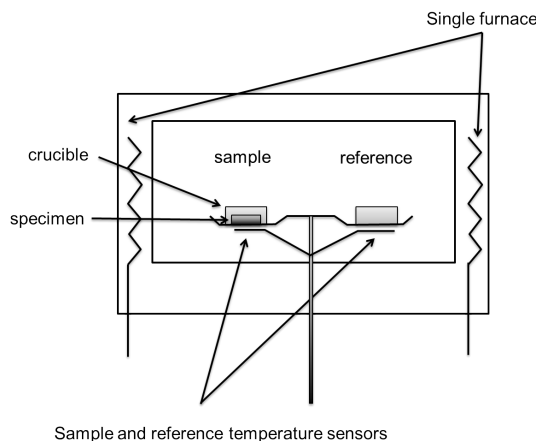


Figure 3.2: Sketch of the furnace of a DTA (or heat flux DSC). Note that a single furnace is used for both the sample and the reference.

modified design of the furnace and temperature sensors. It contains the algorithm for conversion of the measured DTA signal into the differential heat flow according to appropriate calibrations [94]. Therefore, it is also called *heat flux* DSC. A heat flux DSC can be used for high-temperature measurements where the power compensation DSC sensor is not applicable.

3.2.5 Measurement of high-temperature heat capacity

The high-temperature heat capacity was measured in reference to standard sapphire using graphite crucibles, in a high-purity argon atmosphere, with Netzsch STA 449/C/6/MFC/G Jupiter DSC/TG mode with a DSC-Cp sample holder. Before measurements, graphite crucibles were annealed in high-vacuum at 1000 C for 10 hours to remove impurities from the crucibles. The c_p values were determined according to the equation

$$c_p(T)_{sample} = \frac{m_{sapphire}}{m_{sample}} \cdot \frac{\dot{Q}_{sample} - \dot{Q}_{baseline}}{\dot{Q}_{sapphire} - \dot{Q}_{baseline}} \cdot c_p(T)_{sapphire}, \quad (3.9)$$

where \dot{Q} is the measured thermal signal, which is calibrated for the sample holder and automatically converted to the heat flow (mW) by the algorithm contained in the instrument software. Note that the high-temperature heat capacity measurements were carried out upon continuous heating rather than step-wise heating which was applied for the high-precision heat capacity measurements (below 1000 K) in the power compensation DSC.

First, a measurement of a empty graphite crucible was performed. Then a standard sapphire with the same crucible was measured. Finally, a sample

with the similar mass of reference was sealed in the same crucible and measured with the same program. During these measurements, all experimental parameters were kept constant, such as argon flux, initial temperature, temperature program, masses and positions of the crucibles. All three measurements were done on the same day to ensure the same experimental environment.

3.3 In-situ synchrotron X-ray scattering on levitated droplets

3.3.1 Principles of total X-ray scattering experiments

The *sample scattering amplitude* is the basis of scattering theory. It is the wave amplitude that is scattered by an assembly of scattering atoms [100]

$$\Psi(\mathbf{Q}) = \frac{1}{\langle b \rangle} \sum_v b_v e^{i\mathbf{Q}\mathbf{R}_v}, \quad (3.10)$$

where b_v is the scattering amplitude of the atom v , which is the atomic form factor for X-ray scattering, and \mathbf{R}_v is the position of the atom v . \mathbf{Q} is the scattering vector, defined as

$$\mathbf{Q} = \mathbf{k}_{init} - \mathbf{k}_{final}, \quad (3.11)$$

where $\mathbf{k} = 2\pi/\lambda$ is the wave-vector of the incoming (init) and scattered (final) beam. For elastic scattering, $Q = 4\pi\sin\theta/\lambda$. Note that $\Psi(\mathbf{Q})$ is the Fourier transform of the atomic position \mathbf{R}_v . Therefore, if we know the scattering amplitude of a sample, we can determine the atomic positions or sample structure via the inverse Fourier transformation of $\Psi(\mathbf{Q})$. However, one cannot measure the scattering amplitude directly. Rather, one only measures the intensity $I(\mathbf{Q})$ of the scattered wave, which is related to $|\Psi(\mathbf{Q})|^2$ via (see ref.[100])

$$I(\mathbf{Q}) = \frac{\langle b \rangle^2}{N} |\Psi(\mathbf{Q})|^2 + \langle b \rangle^2 - \langle b^2 \rangle, \quad (3.12)$$

where $\langle b \rangle^2 - \langle b^2 \rangle$ is the Laue monotonic scattering (Laue term). Here by normalizing $I(Q)$ with respect to $\langle b \rangle^2$, we obtain

$$S(\mathbf{Q}) := \frac{I(\mathbf{Q})}{\langle b \rangle^2} = \frac{1}{N} \cdot |\Psi(\mathbf{Q})|^2 + \frac{\langle b \rangle^2 - \langle b^2 \rangle}{\langle b \rangle^2}, \quad (3.13)$$

where $S(\mathbf{Q})$ is called the *total scattering structure function* or *structure function*, or sometimes also *structure factor*, which converges to unity at large \mathbf{Q} . The $S(\mathbf{Q})$ is a continuous function of the scattering vector \mathbf{Q} . If the scattering is

3. Chapter: Materials and methods

isotropic, such as in gases, liquids and glasses, $S(\mathbf{Q})$ only depends on the magnitude of the scattering vector, Q , rather than its direction. $S(\mathbf{Q})$ contains the local structural information in the reciprocal-space and can be measured in X-ray scattering experiments.

A direct Fourier transform of structure function $S(Q)$ yields the *reduced pair distribution function PDF*, $G(r)$, via the equation [100]

$$G(r) = 4\pi r(\rho(r) - \rho_0) = 4\pi r\rho_0(g(r) - 1) = \frac{2}{\pi} \int_0^\infty Q[S(Q) - 1] \sin(Qr) dQ, \quad (3.14)$$

where ρ_0 is the average number density; ρ is atomic number density and r is the distance to the reference atom. The PDF is an important physical quantity that provides structural information in the real space. It directly reflects the distribution of the relative atomic positions. It represents the probability of finding an atom at the distance r relative to the reference atom.

Comparing the *atomic pair distribution function*, $g(r)$, and the pair density distribution function, $\rho(r) = \rho_0 g(r)$, the main advantage of using $G(r)$ is that it is directly obtained from the Fourier transform of the measured data of $S(Q)$ and there is no need to assume a value of the average number density ρ_0 . Furthermore, the uncertainties on $G(r)$ are constant with r . This is unlike the function $g(r)$ and $\rho(r)$ where the uncertainties fall off as $1/r$ which emphasizes the structural information at low- r values [100].

The PDF can be reversely transformed into $S(Q)$ as a function of $G(r)$ using

$$S(Q) = 1 + \frac{1}{Q} \int_0^\infty G(r) \sin(Qr) dr. \quad (3.15)$$

The materials structure can be studied by analysis of $S(Q)$ in reciprocal-space or $g(r)$ in real-space.

Another useful function is the radial distribution function (RDF), $R(r)$, which is related to the pair distribution function $g(r)$

$$R(r) = 4\pi r^2 \rho_0 g(r). \quad (3.16)$$

The coordination number of atoms on the coordination shell between the distance r_1 and r_2 can be calculated by

$$N_c = \int_{r_1}^{r_2} R(r) dr. \quad (3.17)$$

Direct information from PDF without structural modeling [100]

1. The peak positions provide the information about atomic pair separations. The PDF is a linear superposition of the local environment of all the atoms involved in the scattering measurement. On short range length scales, the nearest-neighbor atomic distance is very similar for each atomic pair. Thus, the first peak position reflects the nearest-neighbor distance or bond length directly. Similarly, the 2nd or nth peak position gives the information about the distance of the atoms on the 2nd or nth coordination shell, although these peaks at larger r will be less well-defined and broader in disordered or liquid materials [100].
2. The integrated area under the peak corresponds the coordination number within a certain distance [100].
3. The peak width provides the information about the atomic pair probability distribution. Wider PDF peaks indicate more disordered atomic arrangements or more atomic positions deviating from the average position. The PDF width as a function of inter-atomic spacing (e.g., nearest-neighbor distance r_1) discloses the information about atomic potentials [100].

Information from PDF using structural modeling

More quantitative structural information can be extracted by fitting the experimental data with structural models or comparing the data with calculated PDF from models [100]. So far the modeling methods have been only applied to the simple binary or ternary systems such as Cu-Zr-Al [101]. It has been proven difficult to model complicated four- or five-component metallic glass systems.

3.3.2 X-ray sources

The commonly used X-rays in the laboratory are generated by a X-ray tube including a cathode to generate an electron beam and an anode as a target to collect electrons. For example, a X-ray tube with a copper anode generates the characteristic K_α X-rays with the wavelength of 1.544 Å [100].

With the most advanced technique, X-rays are from synchrotron X-ray sources. The synchrotron radiation is produced in a so-called storage ring, which is a ring-shape particle accelerator (see Fig. 3.3). Electrons or positrons are accelerated as fast as 99.99... % the speed of light. When the particles are deflected by the magnetic fields through the magnetic insertion devices (e.g., bending magnets, undulator), parts of the energy of the particles are emitted in the form of intense, collimated and brilliant beams of light, known as the synchrotron radiation [103].

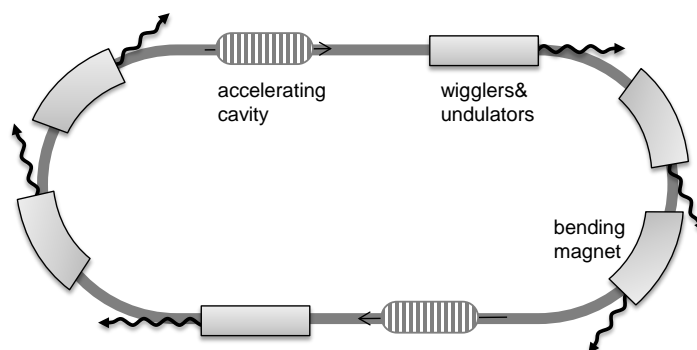


Figure 3.3: Sketch of a synchrotron radiation storage ring. Electrons travel through a closed system with evacuated tubes and magnetic devices. The synchrotron light is generated when the electrons pass the bending magnets or other magnetic insertions (e.g., wigglers or undulators).

Due to the loss of kinetic energy of the particles via synchrotron radiation, the particles have to be re-accelerated every turn going through the accelerating cavity.

Synchrotron radiation is widely used for high resolution and accurate measurements due to the unique properties of the synchrotron light [103]. The synchrotron light has high brilliance (or brightness of photon flux). The light is extremely intense and highly collimated. Brilliance is one of the most important benchmarks of the quality of a light source. It is a measure of the number of photons generated in a certain wavelength range. It also indicates how tightly the beam is collimated. The higher brilliance enables more possibilities of high-quality measurements and reduces measurement time. Figure 3.4 shows the average brilliance of several light sources as functions of photon energies. For example, the DORIS III is more intense than that from conventional x-ray tubes by ~ 10 orders of magnitude. The synchrotron light has a wide energy spectrum and is tuneable. The energy of photons emitted from a synchrotron source can be ranging from infrared light to high-energy X-rays. It is possible to make use of an intense beam of any selected wavelength. The synchrotron light is also highly polarized radiation. The synchrotron source can generate ultra short pulses of the light, which enables time-resolved studies.

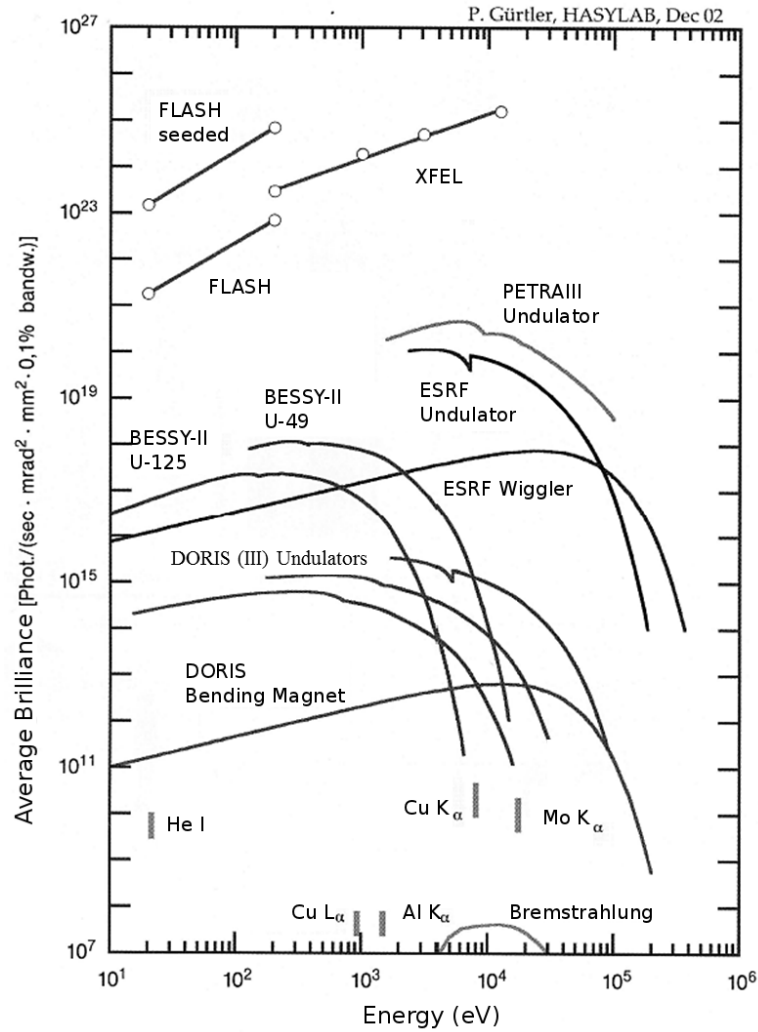


Figure 3.4: Brilliance of different X-ray sources from synchrotron radiation storage rings at DESY in Hamburg. Note that the peak brilliance of DORIS III is several orders of magnitude higher than that of conventional X-ray tubes ranged from around 10^6 to 10^{12} [Photons/(s mrad² mm² 0.1%BW)] (taken from ref. [102]).

3.3.3 Experimental setup

Diffraction and detection

The in-situ X-ray-scattering experiments were carried out on the beamline BW5 at HASYLAB/DESY in Hamburg. The beam size was $0.5 \times 0.5 \text{ mm}^2$ and the X-ray wavelength was 0.124 \AA (100 keV). Diffraction was performed in transmission mode using a Perkin Elmer 1621 AN/CN Digital X-ray detector with 2048×2048 pixels and a pixel size of $200 \times 200 \text{ \mu m}^2$. The advantage of a flat panel detector (FPD) is to have a real-time read-out process with one frame per second, which is highly productive and makes it possible to observe the local structural changes dynamically.

Electrostatic levitation (ESL)

Electrostatic levitation [104] experiments were carried out in collaboration with the Institute of Materials Physics in Space at German Aerospace Center (DLR). The levitation chamber utilizes the electrostatic force generated by high voltage amplifiers to levitate samples against gravity under high vacuum (in the range of $\sim 10^{-7}$ mbar) conditions (see Fig. 3.5).

An electrically charged sample (S) is levitated in the electric field of two vertically arranged electrodes (TE, GE) supplied with a high voltage (HV) and the horizontal sample position is actively controlled by two pairs of side high-voltage electrodes (SEs). The sample position is monitored by the positionsensitive photodetectors (PSDs) that detect the shadow of the sample casted by two crossed expanded laser beams (BEs). The position signal is the input for an algorithm for sample position control, which adjusts the voltage supplied to the electrodes every 2 ms [104].

Heating of the sample is achieved by two 75 W infrared fiber coupled diode lasers with a wavelength of 808 nm, which is able to melt the metals with high melting temperatures above 2000 K. The sample is cooled continuously by switching off the laser power. Temperature of the sample is measured using two fiber coupled two-color pyrometers for contactless measurement. The typical sample size is in the range of ~ 10 -100 mg for both density and in-situ X-ray diffraction experiments.

3.3.4 Data analysis methods

After measuring with the in-situ synchrotron XRD, the raw data include two dimensional (2D) images of the XRD patterns and the time/temperature information. In practice, the data analysis of the XRD measurements can be divided into five stages.

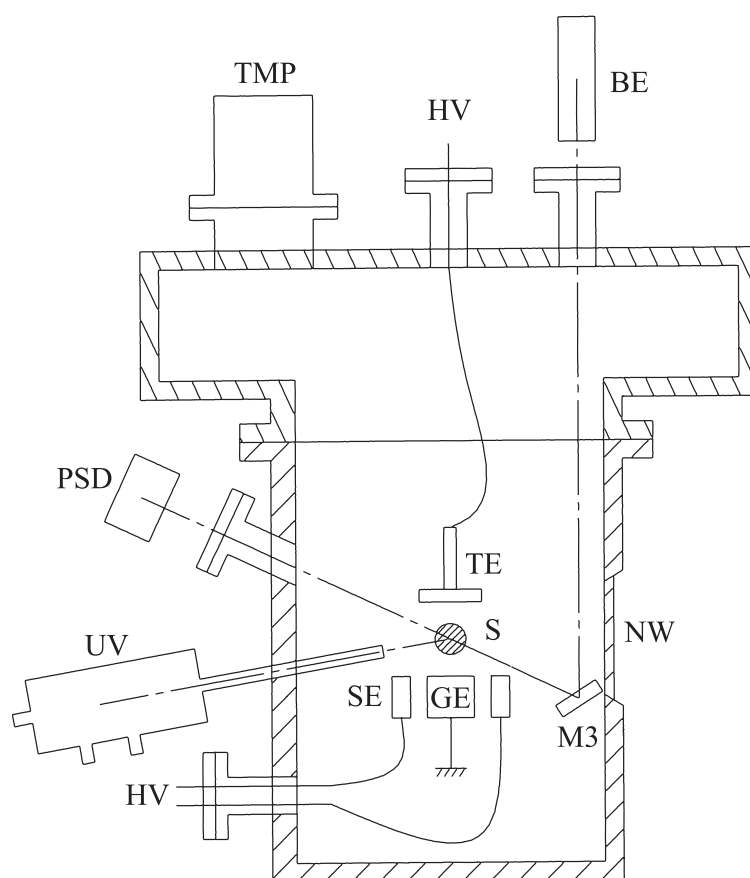


Figure 3.5: Schematic drawing of the electrostatic levitation chamber by Kordel et al. [104]. TE: Top electrode; GE: ground electrode; SE: side electrode; S: sample; PSD: position sensitive detector; TMP: turbo molecular pump; UV: UV lamp; NW: neutron/X-ray window in vacuum chamber; HV: high voltage feedthrough; M3: mirror; BE: beam expander for laser. (taken from ref. [104]).

First, the 2D images of XRD patterns need to be calibrated and the dead pixels are masked using the program Fit2D provided by European Synchrotron Research Facility [105, 106]. One dimensional patterns, i.e., intensity vs. scattering vector Q are obtained by the integral of the 2D images. Second, the XRD patterns are correlated with the temperature which is usually measured by pyrometers or thermal couples. A temperature calibration is necessary for the temperature measured by pyrometers. Third, a preliminary analysis of the raw intensity data is sometimes helpful for the further analysis at later stages. Fourth, the raw intensity data are corrected and the structure functions $S(Q)$ and the reduced pair distribution functions $G(r)$ are calculated using PDFgetX2 [107]. A detailed description on how to obtain structure function $S(Q)$ will be given in the next section. At last, the qualitative and quantitative structural information can be obtained from the structure functions and pair distribution functions.

3.3.4.1 From measured intensity data $I(Q)$ to structure function $S(Q)$

The measured intensity data need to be corrected to obtain the total structural function $S(Q)$ and pair distribution function $G(r)$. The central equation is the desired $S(Q)$ as a function of coherent single scattering sample cross-section, $d\sigma^s/d\Omega$, [100]

$$S(Q) = \frac{1}{\langle f(Q) \rangle^2} \left(\frac{d\sigma^s}{d\Omega} \right) + \left(\frac{\langle f(Q) \rangle^2 - \langle f(Q)^2 \rangle}{\langle f(Q) \rangle^2} \right). \quad (3.18)$$

The cross-section is the probability that a photon is scattered by a given volume element in a given direction [100]. $f(Q)$ is the atomic form factor and the brackets $\langle \dots \rangle$ refer to a compositional average.

The scattering processes can be characterized as elastic or inelastic and coherent vs. incoherent. Elastic scattering refers to the event where the scattering particle has no energy exchange with the system. During inelastic scattering, there is an exchange of energy between the particle and the system. In coherent scattering, there is wave interference because the scattered waves have a definite phase relation. The resulted waves interfere constructively or destructively and the intensity is the square of the sum of the wave amplitude. In contrast, in incoherent scattering, there is no interference between the scattered waves. The resulting intensity is the sum of the intensity of the individual waves. Table 3.1 lists the common scattering processes that occur, most of the time, simultaneously in materials. In addition, the nature of the respective process is listed. Note that the structural information is contained in the wave interference. Thus, the coherent scattering is of interest for structural investigations [100].

Scattering processes	Nature of the process
Bragg scattering	elastic and coherent
Thermal diffuse scattering	inelastic and coherent
Laue monotonic scattering	elastic and incoherent
Nuclear scattering ¹	elastic and incoherent
Compton scattering	inelastic and incoherent
all coherent scattering at high enough Q	incoherent due to Debye-Waller effects

Table 3.1: The nature of the scattering processes [100].

3.3.4.2 Data corrections

The following factors should be considered to correct the measured XRD data [100].

Detector dark counts and deadtime corrections. Even when X-ray is absent, counts are still detected due to thermal excitation in the detector and noise in the electronics. Therefore, these dark counts should be measured with electronics on but X-ray off. The dark counts should be taken periodically throughout the experiments to ensure the stability in detector and electronics setup. These dark counts can be subtracted during the data recording process using the data taking software. The detector needs some time to reset after one photon is detected to be able to detect the next event (for a 2D detector, at the same spot). This period of time is known as deadtime, in which the photons are not counted. Therefore, deadtime corrections should be taken into account for the total counts [100].

Absorption and multiple scattering corrections. The sample absorbs the intensity that is scattered in the sample container (e.g., ESL). Therefore, this absorption should be taken into account when determining the scattering cross-section of the sample [100]. The multiple scattering refers to the photons scattered more than once, which yields featureless background signals without useful structural information. Therefore, the multiple scattering should be removed. The contribution of the multiple scattering to the intensity is usually small especially for very thin samples, for which the multiple scattering correction can be omitted. The absorption and multiple scattering corrections can be performed within the data analysis programs (e.g., PDFgetX2).

Polarization corrections. If the radiation is unpolarized, the scattering

process leads to X-ray polarization which makes the measured intensity depend on the scattering angle. This should be corrected, before obtaining the structure function $S(Q)$. If the synchrotron X-ray radiation is fully polarized, no correction is needed [100].

Compton scattering corrections. Some electrons are weakly bound and stay at rest before the collision with X-ray photons. After the photons collide with these electrons, the electrons at rest start to move and energy exchange occurs. This process is inelastic and incoherent, known as Compton scattering, which is often referred as "inelastic scattering" by the X-ray scattering community. Compton scattering does not contain structural information and thus should be subtracted [100]. For the measurements performed with high energy X-ray at higher scattering angles (or high-Q values), the Compton cross-section increases while the elastic scattering cross-section decreases. The former can be considerably larger than the latter at high-Q values. One approach suggested by Ruland [108] is to subtract the theoretical Compton scattering at low-Q data and discriminate the Compton scattering away at high-Q data. An empirical function for the proportion of Compton scattering is proposed by Ruland and has been frequently used in practice. However, it was pointed out that the Ruland function is not very satisfactory in many cases [109].

3.3.4.3 Error analysis

There are three main errors that may result in artifacts or noise in the converted PDF. The Fourier transform of $S(Q)$ must have an integration range of Q . In other words, the integration is terminated at a chosen maximum scattering vector in Q -space, Q_{max} , that leads to oscillations (ripples) of the PDF. This error is known as *termination error*, depending on the value of chosen Q_{max} . A large enough Q_{max} will minimize the termination error in PDF [100]. However, a large Q_{max} for the integration will lead to another problem, more noise. The *statistical errors* are increased with a larger Q_{max} [100]. Therefore, it is always a difficult task to choose an appropriate Q_{max} to terminate to obtain a best PDF. A high Q -resolution is also important to obtain an accurate PDF, especially for informations at larger r values [100]. Note that the Q -resolution is independent of Q for synchrotron X-ray monochromatic beam scattering measurements [100].

3.4 Measurement of density

Density measurements were performed in the electrostatic levitator [104] by recording back-lighted sample images during continuous cooling and heating of the sample using a high speed camera with 200 frames per second. The volume of the

3. Chapter: Materials and methods

sample was then calculated according to the area of its shadow assuming rotational symmetry and calibrated with standard spheres with known volumes. For each data point an average over 20 images was taken. The sample temperature was assumed to be constant during the time (0.1 s), over which the frames were taken [2].

Chapter 4

The glass transition and the order-disorder transition of $\text{Fe}_{50}\text{Co}_{50}$ and their relation with strong liquids

In this Chapter, the non-liquid crystalline system $\text{Fe}_{50}\text{Co}_{50}$ is studied. The thermodynamics and kinetics of the (un)freezing-in processes during chemical or structural ordering/disordering are investigated. The experimental results are compared with computer simulations for critical phenomena in liquids. It is, therefore, argued that the dynamic and specific heat capacity anomalies found in strong liquids are the consequences of an underlying order-disorder transition in the liquid state. This work has been partially presented in Shuai Wei's master thesis and published in ref. [1].

4.1 Introduction

Liquids can be classified according to their kinetic properties such as relaxation time or viscosity as a function of temperature. The temperature dependence of the relaxation time of many liquids shows non-Arrhenius behavior. These liquids are known as fragile liquids [6]. The origin of the non-Arrhenius kinetics has been studied and debated extensively in the last decades [53, 110, 111]. Recent studies suggested that the drastic slowdown in fragile liquids is associated with an increasing dynamic or static correlation length as T_g is approached from above [112, 113].

Less attention has been devoted to the so-called strong liquids, which are characterized by the Arrhenius-like dynamic behavior and are the opposite extreme

4. Chapter: The glass transition and the order-disorder transition of $\text{Fe}_{50}\text{Co}_{50}$ and their relation with strong liquids

of the fragile liquids. It is natural to ask why some liquids are fragile while others are strong. How are strong liquids related to fragile liquids? How do strong liquids differ from fragile liquids?

The strong and fragile behavior is closely related to the specific heat capacity changes during the glass transition [6]. An interesting "glass" transition phenomenon has been revisited by Angell [7] in order-disorder transition systems such as plastic crystals and superlattice alloys. A structural arrest occurs in these alloys during cooling below the order-disorder temperature. The structural arrest is a kinetic freezing-in of the orientational or chemical order during the ordering process. The freezing-in event is a timescale crossover of the experimental and the system internal timescales. In this sense, it is, thus, also a "glass" transition (ergodicity breaking or restoring). Such a phenomenon was observed in 1940s by Kaya and Sato [114] as a sudden change in the λ shape specific heat capacity peak during up-scanning the annealed $\text{Fe}_{50}\text{Co}_{50}$ alloys.

In an early review article of Nix and Shockley in 1938 [115], they noted anomalous kinks (ergodicity-restoring) in the specific heat capacity during disordering of Cu_3Au and β -brasses. In 1970s, Gschwend et al. [116, 117] studied the heating rate dependence of "subpeak" in the specific heat capacity of Mg_3Cd below the order-disorder transition and explained it as a relaxation phenomenon. The glass transition phenomena in these systems can be compared with the liquid glass-forming systems and provide insight into the strong-fragile behavior.

In this work, we carry out a systematic study of the glass transition during ordering/disordering of the non-liquid superlattice $\text{Fe}_{50}\text{Co}_{50}$ system. The similarities in kinetic and thermodynamic properties between the glass transitions of $\text{Fe}_{50}\text{Co}_{50}$ and of strong liquids are discussed. This work presents an experimental approach to the understanding of the strong-fragile classification in various classes of substances.

4.2 Kinetics of the glass transition

Figure 4.1 shows a DTA trace of an as-cast sample of $\text{Fe}_{50}\text{Co}_{50}$ at a heating rate of 20 K min^{-1} . At around 800 K, an exothermic dip in the heat flow is observed, indicating an enthalpy relaxation event during the up-scan. With increasing temperature, the heat flow jumps up at around 850 K as the system restores its thermodynamic equilibrium state. A λ shape specific heat capacity peak at around 1003 K indicates that an order-disorder (λ) transition occurs. In this case, it is a 2^{nd} order phase transition with a critical point at $T_\lambda = 1003 \text{ K}$ and $P = 1 \text{ atm}$.

The system from 700 to 900 K experiences an unfreezing process of the partially frozen-in disordered state due to the previous freezing. Before the sample

4. Chapter: The glass transition and the order-disorder transition of $\text{Fe}_{50}\text{Co}_{50}$ and their relation with strong liquids

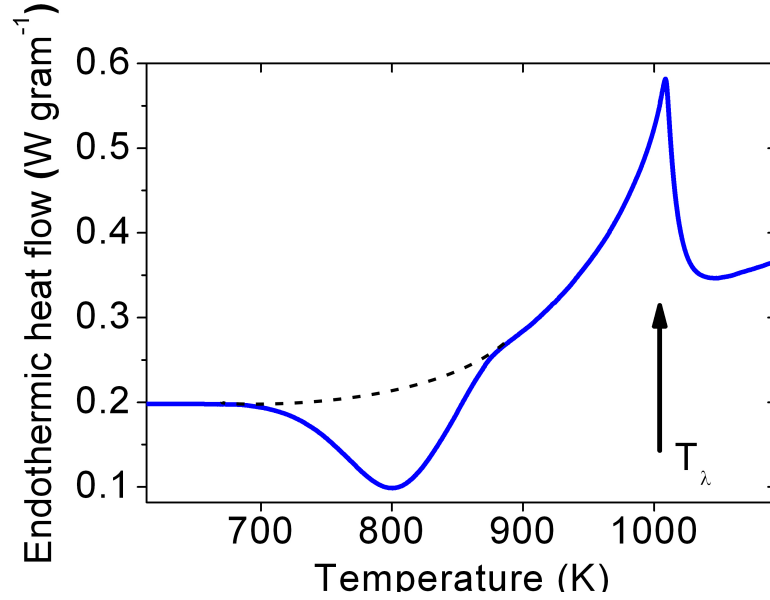


Figure 4.1: A DTA upscan of an as-cast sample of $\text{Fe}_{50}\text{Co}_{50}$.

is up-scanned in the calorimeter, it is rapidly cooled from a highly disordered state (1003 K), ordering proceeded until the kinetics is too slow to keep the equilibrium at around 900 K. As a result, the ordering is frozen-in (ergodicity-breaking). Therefore, during the up-scan shown in Fig. 4.1, the reverse process occurs, that is, ergodicity-restoring. This kinetic transition event is nothing but the experimental timescale crossing with the system internal timescale, which is the definition of a glass transition.

A characteristic feature of a glass transition is the cooling rate dependence of the glass transition temperature, T_g . To quantify this dependence, the sample is scanned in the DSC at various heating/cooling rates and the results are shown in Figure 4.2. The signature of the glass transitions is a jump in specific heat capacity during reheating to regain the equilibrium state. The calorimetric T_g is defined as the onset of the observed glass transition during the reheating, T_g^{onset} . T_g shifted to higher temperature by about 50 K as the heating/cooling rate increased by 1 order of magnitude. T_g depends on the cooling rate or time.

The inset of Figure 4.2 shows an Arrhenius plot of the relaxation times as a function of inverse temperature. The relaxation times are approximated by normalizing the width of the glass transition region ΔT_g with the heating rate q_h ($q_h = q_c$) (Eq. 3.4), [118]

$$\tau = \frac{\Delta T_g}{q_h}.$$

The relaxation times as a function of temperature are fitted well with the

4. Chapter: The glass transition and the order-disorder transition of $\text{Fe}_{50}\text{Co}_{50}$ and their relation with strong liquids

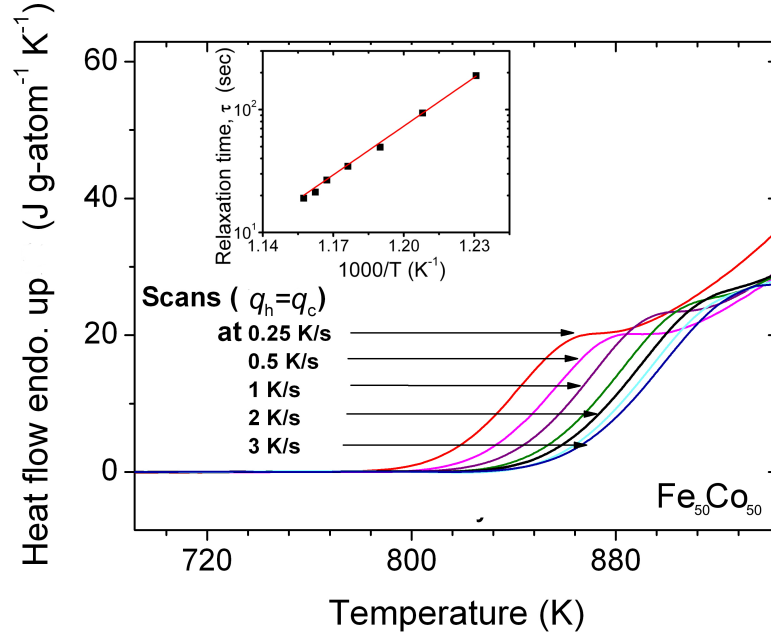


Figure 4.2: $\text{Fe}_{50}\text{Co}_{50}$ is scanned in the DSC throughout the glass transition region at the various heating rate (q_h) which is kept the same as the preceding cooling rate (q_c) [97] ($q_h = q_c$). The measured heat flow is divided by q_h . The heat flow curves shift to higher temperatures as the heating/cooling rates increase. The inset shows an Arrhenius plot for the relaxation times, τ , (squares) of the $\text{Fe}_{50}\text{Co}_{50}$, which are obtained from the Eq. 3.4. The data are plotted with the Arrhenius equation and the VFT equation, respectively [1].

Arrhenius law

$$\tau = \tau_0 \exp\left(\frac{E}{k_B T}\right),$$

with an activation energy $E \approx 2.7$ eV, a pre-exponential factor of $\tau_0 \approx 1 \cdot 10^{-15}$ s and k_B the Boltzmann constant.

The data are also fitted with the Vogel-Fulcher-Tammann (VFT) equation [35, 36],

$$\tau = \tau_0 \exp\left(\frac{D^* T_0}{T - T_0}\right),$$

where the pre-exponent is assumed $\tau_0 \approx 10^{-15}$ s, the fitting yields a fragility parameter $D^* \gg 100$ and $T_0 \sim 0$ K.

An alternative approach to determine the fragility is to measure the fictive temperatures for different cooling rates as the method proposed by Wang et al.

4. Chapter: The glass transition and the order-disorder transition of $\text{Fe}_{50}\text{Co}_{50}$ and their relation with strong liquids

[60]. Figure 4.4 shows the DSC up-scans at 20 K min^{-1} after cooling at different rates, q . Figure 4.3 shows the "area-match" method to determine the standard fictive temperature, T_f^s , that is, the fictive temperature for the "standard" scan (i.e., heating at $q_s = 20 \text{ K min}^{-1}$ after cooling at $q_s = 20 \text{ K min}^{-1}$). The fictive temperature, $T_f(q)$, for a given cooling rate q is obtained by

$$\Delta H(q) = \int_{T_f^s}^{T_f(q)} \Delta c_p^{excess} dT,$$

where $\Delta H(q)$ is the difference in area between the standard scan and non-standard scans. Δc_p^{excess} is the difference in heat flow between the equilibrium state and the frozen-in state.

With the area-match, the fictive temperatures and the cooling rates are plotted on a logarithmic scale, as $\log(q/q_s)$ versus T_f^s/T_f , as shown in Figure 4.4. The fragility index m is determined from the slope of the fitted straight line according to the equation [98]

$$\log \frac{q}{q_s} = m - m \frac{T_f^s}{T_f}.$$

The fitting yields the fragility steepness index $m \approx 16$, which is extremely strong in terms of fragility. This value is consistent with the fragility ($D^* > 100$) obtained from the VFT fitting.

4.3 Specific heat capacity on a long timescale

Figure 4.5 shows the specific heat capacity c_p of $\text{Fe}_{50}\text{Co}_{50}$. The specific heat capacity can be attributed to two parts - the vibrational contribution $3R$ (Dulong-Petit law where R is gas constant) and configurational contribution. The measured specific heat capacity values (open squares and solid dots) from room temperature to the glass transition temperature, T_g , correspond to the frozen-in (non-equilibrium) state. The value for the equilibrium state below T_g cannot be measured directly in the DSC, because the timescale for the system to be equilibrated is much larger than the laboratory time scale. The values of c_p on a long timescale (half open circles with error bars) are obtained from the enthalpy recovery experiment (see Fig. 4.6 and Eq. 4.2). Above the glass transition region, the system reached equilibrium and the ergodicity is restored.

The c_p data are compared to the thermodynamic theories for order-disorder transition, i.e. the Kirkwood [119, 120] 2^{nd} order approximation and the Bragg-Williams theory [121, 120], as shown in Fig. 4.5. The Kirkwood approximation matches the data of the equilibrium state much better than the Bragg-Williams

4. Chapter: The glass transition and the order-disorder transition of $\text{Fe}_{50}\text{Co}_{50}$ and their relation with strong liquids

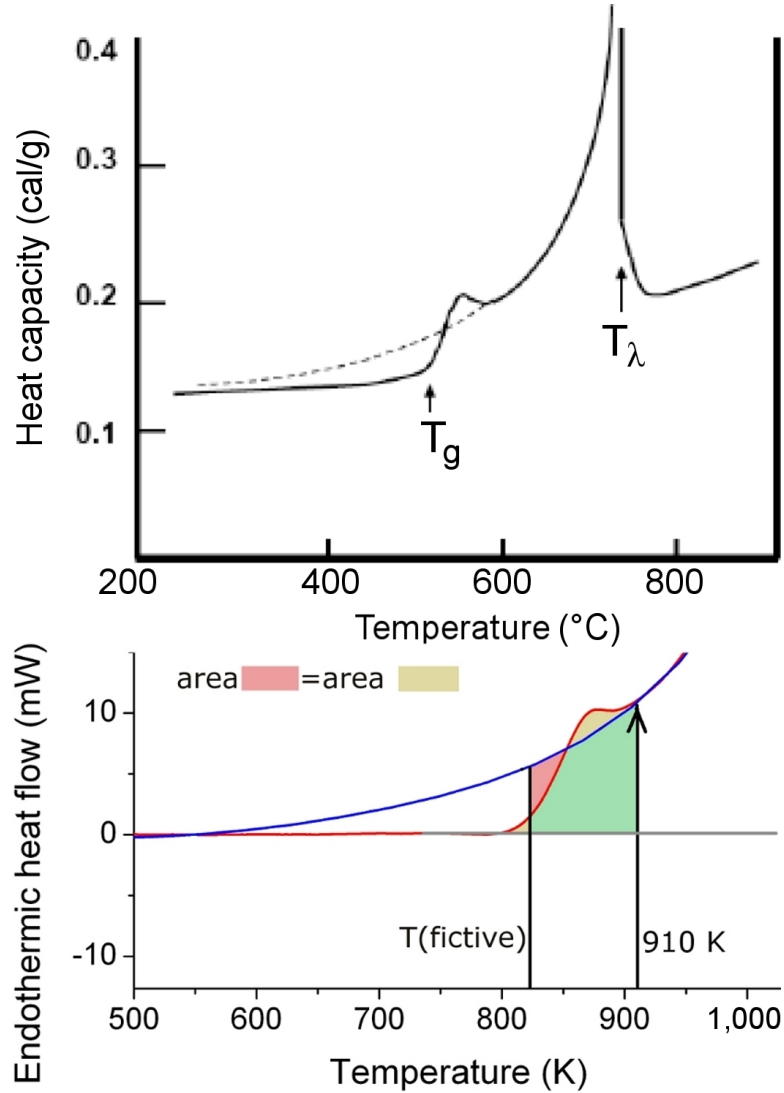


Figure 4.3: (Upper panel) Specific heat capacity of the "glass" transition during the order-disorder transition of superlattice $\text{Fe}_{50}\text{Co}_{50}$, reproduced from ref. [114]. During cooling, the ordering of Fe and Co onto their respective simple cubic lattices is arrested by the glass transition with a large drop in specific heat capacity. On heating, the order-disorder transition ($\text{B2} \leftrightarrow \text{BCC}$) happens with a lambda peak at 730 C and the glass transition (ergodicity-restoring) starts at about 500 C. (Lower panel) A new DSC scan with the definition of the fictive temperature applied to $\text{Fe}_{50}\text{Co}_{50}$. "Area-match" method is applied to determine the fictive temperature of the system at the standard scan (heating at 20 K min^{-1} after cooling at 20 K min^{-1}). Since in the $\text{Fe}_{50}\text{Co}_{50}$ system the equilibrium state represented by the blue curve is not a constant, or a simple extrapolation, we obtain the curve from theoretically predicted specific heat capacity by the Kirkwood 2nd order approximation (see the Fig. 4.5).

4. Chapter: The glass transition and the order-disorder transition of $\text{Fe}_{50}\text{Co}_{50}$ and their relation with strong liquids

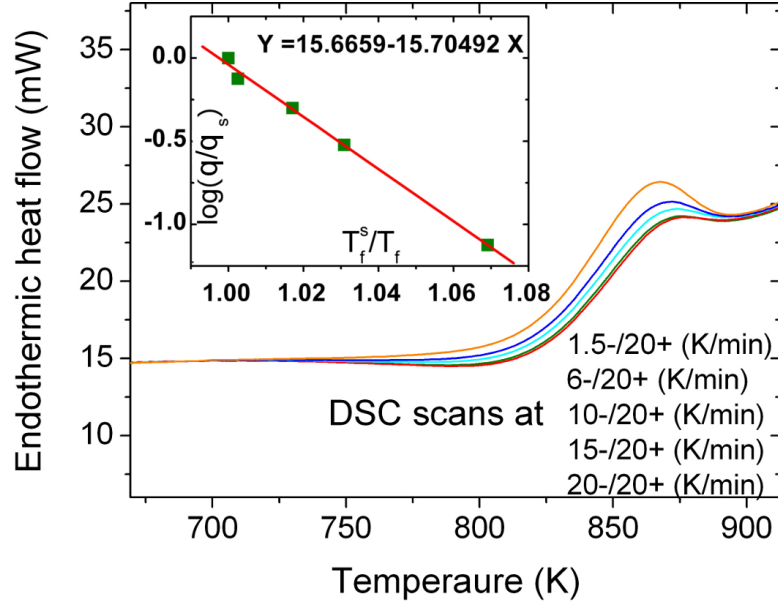


Figure 4.4: DSC upscans at a heating rate of 20 K min^{-1} after cooling at 1.5 K min^{-1} , 6 K min^{-1} , 10 K min^{-1} , 15 K min^{-1} and 20 K min^{-1} , respectively. Inset: Wang-Velikov Arrhenius plot, in which the ratio of the sample cooling rate (q) to the standard cooling rate ($q_s = 20 \text{ K min}^{-1}$) is plotted on a logarithmic scale against the ratio of the standard fictive temperature (T_f^s) vs. the fictive temperature (T_f), the latter being determined by the Fig. 4.3 construction for the chosen cooling rate. The Wang-Velikov method captures the kinetics of the glass relaxation process. The slope and intercept of the fitted line indicates the value of fragility m (taken from ref. [1]).

theory. However, as the critical temperature, $T_\lambda = 1003 \text{ K}$, is approached, the Kirkwood approximation also fails to describe the experiments. The Inset shows the specific heat capacity behavior of typical strong and fragile glass-formers in the glass transition region.

Figure 4.6 shows the DSC upscans of the enthalpy recovery measurements in the glass transition region after the isothermal enthalpy relaxation. The isothermal relaxation temperatures are selected below T_g at 740 K , 750 K , 760 K , 770 K , 780 K , 790 K and 800 K , respectively. During the relaxation, the enthalpy state is changed ("relaxed") from the frozen-in state to the equilibrium state. The up-scans with large endothermic overshoots indicate the amount of enthalpy that is recovered. As a reference, the "unrelaxed" sample (without isothermal relaxation) does not exhibit this overshoot.

The area between the curve for the "unrelaxed" sample and the curve for a "relaxed" sample is equal to the amount of the recovered enthalpy. This amount of recovered enthalpy during the DSC scan is equal to the released enthalpy

4. Chapter: The glass transition and the order-disorder transition of $\text{Fe}_{50}\text{Co}_{50}$ and their relation with strong liquids

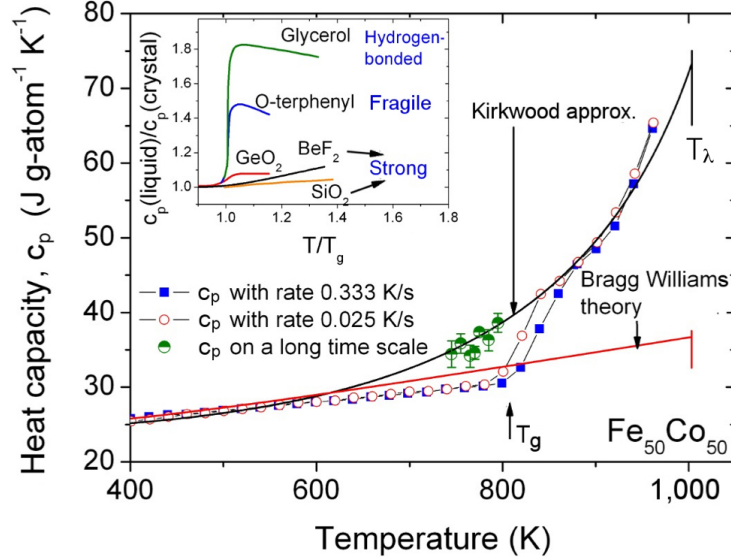


Figure 4.5: The specific heat capacity c_p values measured at different heating rates. The c_p on a long time scale (half-open circles with error bars) is obtained from the enthalpy recovery experiment (see Fig. 4.6 and Eq. 4.2). T_g and T_λ represent the glass transition temperature and the order-disorder transition critical temperature, respectively. The theoretically predicted specific heat capacity by the Kirkwood approximation and the Bragg-Williams theory are compared to the experimental data, respectively. The inset displays the specific heat capacity of strong, fragile and hydrogen-bonded liquids approaching their glass transitions. (taken from ref. [1])

during the preceding relaxation, i.e. $\Delta H^{recovery} = \Delta H^{relaxed}$. The difference in specific heat capacity between the frozen-in (unrelaxed) state and the equilibrium (relaxed) state is obtained as $\Delta H^{eq-fr}(T_i) = \Delta H^{relaxed}(T_i) = \Delta H^{recovery}(T_i)$, where T_i is an isothermal relaxation temperature. Accordingly, the difference in specific heat capacity between the equilibrium state and the frozen-in state, at the temperature $T_{12} = T_1 + (T_2 - T_1)/2$ is calculated as [99]

$$\Delta c_p^{eq-fr}(T_{12}) = \frac{\Delta H^{eq-fr}(T_1) - \Delta H^{eq-fr}(T_2)}{T_2 - T_1}. \quad (4.1)$$

Thus, the absolute specific heat capacity for the equilibrium state, i.e. c_p on a long time scale, below T_g is

$$c_p^{eq} = c_p^{fr} + \Delta c_p^{eq-fr}, \quad (4.2)$$

where c_p^{fr} is the measured values in the laboratory. The resulting c_p on a long time scale (half-open circles) is plotted in Figure 4.5.

4. Chapter: The glass transition and the order-disorder transition of $\text{Fe}_{50}\text{Co}_{50}$ and their relation with strong liquids

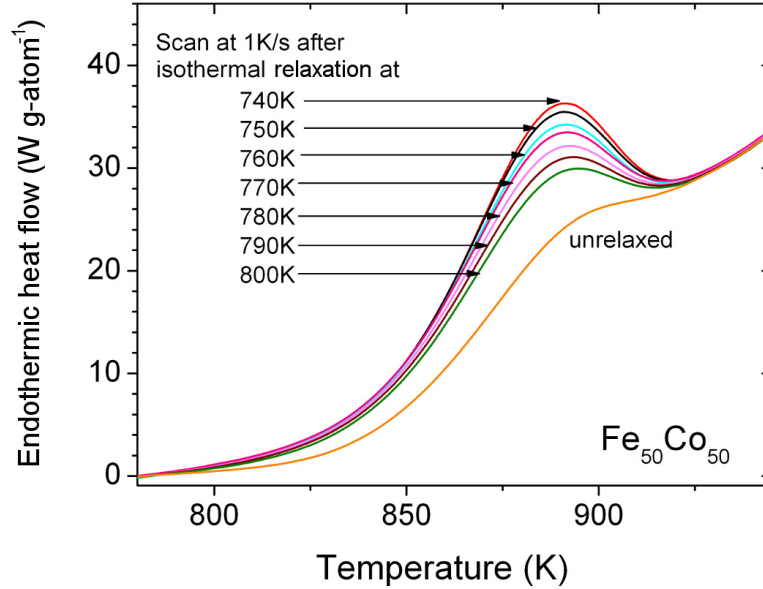


Figure 4.6: The enthalpy recovery up-scans in the DSC after isothermal relaxations towards equilibrium at selected temperatures below T_g . The c_p on a long time scale is obtained from the enthalpy difference between these recovery scans and the difference of their equilibration temperatures (taken from ref. [1]).

4.4 Lambda transition vs. liquid-liquid transition

The glass transition with respect to ordering of $\text{Fe}_{50}\text{Co}_{50}$ was characterized by the "quench and scan" experiment. As $\text{Fe}_{50}\text{Co}_{50}$ is fast cooled from highly disordered state, the system proceeds the ordering process until the temperature drops to a certain degree at which the atoms do not have enough time to diffuse to their energy favorable locations. The system meets a glass transition (ergodicity-breaking) during which the degree of order, the enthalpy and the entropy are frozen-in. The glass transition detected during heating in Fig. 4.2 is the ergodicity-restoring process [67]. Like all liquid-glass transformations, glass transitions observed in the laboratory are kinetic events.

The cooling rate dependence of the glass transition temperature of $\text{Fe}_{50}\text{Co}_{50}$ reflects the change of the relaxation time with temperature. As shown in Fig. 4.2, the relaxation time shows Arrhenius behavior, which is known as strong kinetics in the sense of fragility [6]. The concept of fragility is originally proposed to describe how much the behavior of the relaxation time of a liquid deviates from the Arrhenius law. Many liquids, however, exhibit drastic slowdown approaching T_g during cooling and their relaxation processes are largely non-Arrhenius, so-

4. Chapter: The glass transition and the order-disorder transition of $\text{Fe}_{50}\text{Co}_{50}$ and their relation with strong liquids

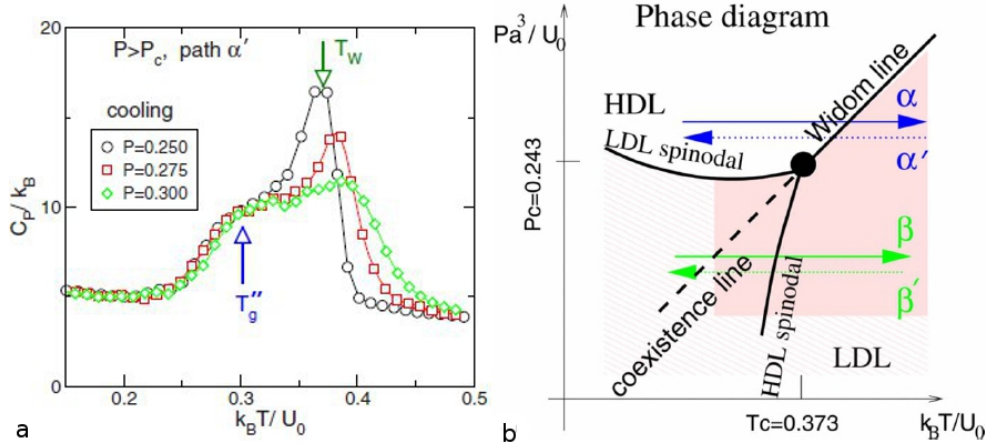


Figure 4.7: (a) Specific heat capacity of simulated liquids using Jagla potential by Xu et al. [92]. The pronounced peaks reflect liquid-liquid transitions. The kinks below the specific heat capacity peaks indicate glass transitions, T_g'' . The pressures for the C_p curves are above the critical pressure. (b) $P - T$ phase diagram. The specific heat capacity maxima correspond to crossing the Widom line along the α' -arrow. The black dot indicates the liquid-liquid critical point. (taken from ref. [92]).

called fragile kinetics.

In many aspects, the glass transition in $\text{Fe}_{50}\text{Co}_{50}$ is reminiscent of a simulated liquid system with two-scale Jagla interaction potentials (see Fig. 2.23a). In a series of simulation studies [70, 122, 92], the Jagla model was used to reproduce the liquid-liquid phase transition phenomenon. A liquid-liquid transition is a polyamorphic transition in liquid states between two liquid phases with the same composition but different entropy and/or density. Such a transition is suggested in the supercooled water and a number of other substances [123], although the nature of liquid-liquid transition is debated due to experimental difficulties in avoiding crystallization. Therefore, numerical simulations are often employed to understand liquid-liquid transitions.

Figure 4.7 shows the specific heat capacities of simulated liquids using the Jagla potential. The three curves represent the heat capacities obtained at different pressures. The specific heat capacity peaks are associated with liquid-liquid transitions in the system. Below the transition temperature, the system is in a phase with high-density and strong kinetics. Above the transition temperature, the liquid phase has a low-density and is fragile. There is a bump below the specific heat capacity peak, marked by T_g . This is the glass transition during cooling. The shape of the specific heat capacity peak at $P = 0.25$ is similar to the lambda peak of $\text{Fe}_{50}\text{Co}_{50}$. In both cases, the glass transition appears as a

4. Chapter: The glass transition and the order-disorder transition of $\text{Fe}_{50}\text{Co}_{50}$ and their relation with strong liquids

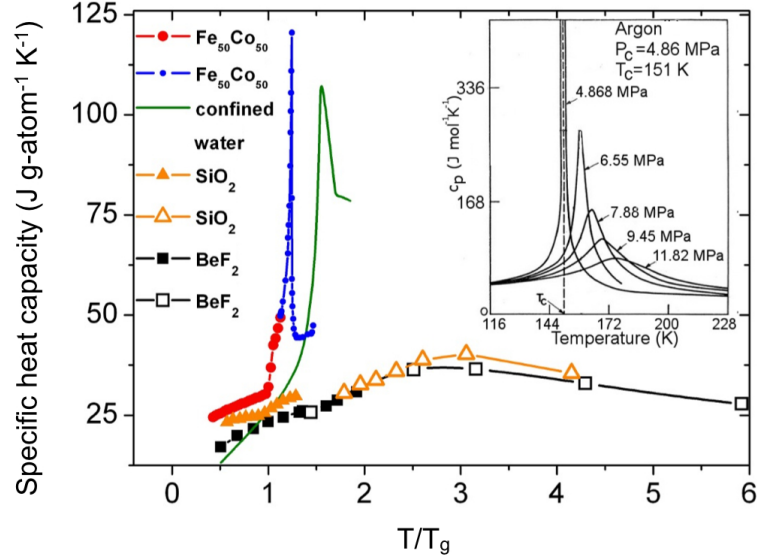


Figure 4.8: Specific heat capacity vs. T_g -scaled temperature for $\text{Fe}_{50}\text{Co}_{50}$, SiO_2 , BeF_2 and water compared to argon near its liquid-gas critical point (Inset). The lambda peak of $\text{Fe}_{50}\text{Co}_{50}$ is sharp; whereas the c_p peaks of SiO_2 and BeF_2 are smeared out for strong-fragile transitions as crossing the Widom lines [1], similar to argon above its critical pressure. The anomalies in specific heat capacity and dynamic behavior of network glassformers are understood as off-critical phenomenology. [1]

cut-off the tail of the lambda peak. In the Jagla model, there is a liquid-liquid critical point in the $P - T$ phase diagram (Fig. 4.7b). At the critical point, both liquid phases become identical and the phase transition is of the 2^{nd} order. In the case of $\text{Fe}_{50}\text{Co}_{50}$, the order-disorder transition is of the 2^{nd} order due to a critical point at ambient pressure and 1003 K.

The order-disorder transition of $\text{Fe}_{50}\text{Co}_{50}$ is an example for the case of a critical point in the superlattice system and it is thus a lambda transition. A lambda transition in a system that does not have lattice to support the structures (e.g., liquid) reflects a liquid-liquid critical point [56], which is the origin of a liquid-liquid transition, that can be observed in the laboratory.

Note that an order-disorder transition can be also a first-order or a continuous smeared out transition, when the pressure is off its critical pressure. Such cases are called underlying lambda transitions. The manifestation of the underlying lambda transition is seen in different shapes of the specific heat capacity peak for the liquid-liquid transitions in the Jagla model. At the pressure slightly above the critical point in the Jagla model, the specific heat capacity peak is still sharp and lambda-like. With further increase of pressure, the specific heat capacity peaks

4. Chapter: The glass transition and the order-disorder transition of $\text{Fe}_{50}\text{Co}_{50}$ and their relation with strong liquids

become smeared out, as shown in Fig. 4.7. These transitions at higher pressures are continuous and correspond to the crossing of the Widom line in the $P - T$ phase diagram, which is an extension of the coexistence line beyond the critical point.

The relaxation behavior of $\text{Fe}_{50}\text{Co}_{50}$ and the Jagla model near T_g exhibit a low fragility. Accordingly, the question arises, whether those strong liquids experience some kind of ordering process during cooling towards the glass transition, although an order parameter in liquids is difficult to define. If ordering/disordering proceeds in strong liquids, there may be a lambda transition at some point.

The dynamic properties of strong glasses, SiO_2 and BeF_2 , follow the Arrhenius law closely at low temperatures near T_g [6]. Strong liquids usually have a weak glass transition (small jump in specific heat capacity) at T_g [60] and a decreasing trend of specific heat capacity as T_g is approached from above (see Inset of Fig. 4.5). Numerical studies on the models of SiO_2 and BeF_2 showed that there is a specific heat capacity maximum above their respective melting temperature in the stable liquid state [87, 72]. The specific heat capacity maxima in the liquids resemble smeared out versions of a lambda peak, which suggests an underlying lambda transition or a liquid-liquid critical point in the systems. Angell and co-workers [71, 56] studied the fragility of SiO_2 above the specific heat capacity maximum and found a very high fragility. Shown in Fig. 4.8 is a comparison of specific heat capacity maxima of strong substances. Note that the nano-confined water is a strong liquid [8] near T_g although it is fragile above T_m at the room temperature.

The glass transition of strong substances can be placed into Angell's "big picture", reproduced in Fig. 4.9, which summarizes the broad spectrum of the glass transition phenomenology of various liquids. The left panel displays the specific heat capacity and the entropy of typical fragile glass-formers. The specific heat capacity is rapidly increasing during cooling approaching T_g . On the laboratory timescale, the equilibrium specific heat capacity is cut-off due to the kinetic glass transition (red line in the left panel of Fig. 4.9). But simulations with Gaussian excitations model (an extended version of two-state model described in Chapter 2) show that there is an underlying first-order thermodynamic transition below T_g in those fragile liquids, which is not accessible experimentally [63]. The middle and right figures display those of strong glass-formers (or the glass-formers which are considered being able to transform into the strong fragility around T_g). The $\text{Fe}_{50}\text{Co}_{50}$ should fit into the middle or right panel, where the glass-formers including $\text{Fe}_{50}\text{Co}_{50}$ exhibit peaks in specific heat capacity above the T_g . The peaks in specific heat capacity associated with the strong-fragile (fragility) transitions [67] are suggested by the Adam-Gibbs equation [49], $\tau = \tau_0 \exp[C/S_c T]$, where S_c is the configurational entropy; τ_0 and C are constants. According to this equation, a change in configurational entropy leads to a shift in relaxation times. As

4. Chapter: The glass transition and the order-disorder transition of $\text{Fe}_{50}\text{Co}_{50}$ and their relation with strong liquids

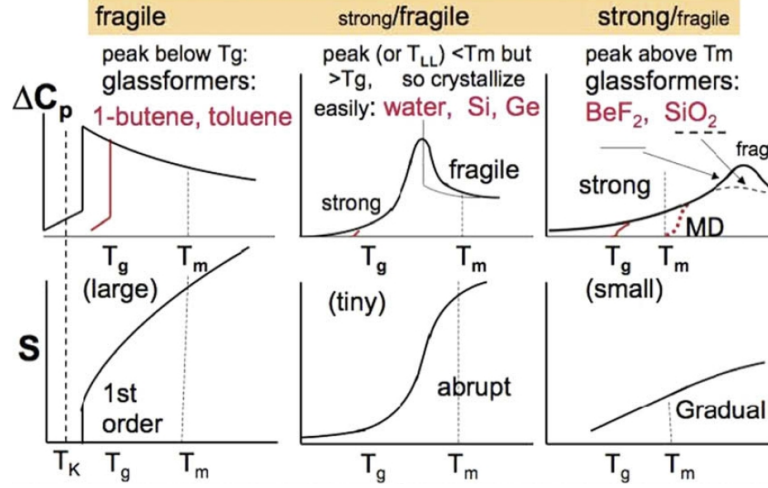


Figure 4.9: The schematic plot of excess specific heat capacity, and excess entropy for fragile molecular glasses and strong glasses are summarized by Angell [7]. T_g and T_m mark the glass transition temperature and the melting temperature, respectively. Water, Si, Ge (middle panel) and BeF_2 , SiO_2 (right panel) show a peak in specific heat capacity above T_g , which represents a strong-fragile transition (a liquid-liquid transition) (taken from ref. [7]).

a consequence, the temperature dependence of relaxation time (or fragility) is changed.

4.5 Correlation length and strong liquids

The lambda transition in $\text{Fe}_{50}\text{Co}_{50}$ is a critical phenomenon. The correlation length diverges at the critical point and the entropy and density fluctuation become infinite at this point. As T_g is approached from above, the correlation length is decreasing. This suggests that the static correlation length in strong liquids has a decreasing trend as T_g is approached from above. The decreasing correlation length behavior towards T_g is an opposite argument to the recent observations of increasing correlation length in the studies of fragile liquids. Using simulations, an increasing correlation length towards T_g in fragile liquids is found [112]. This is considered as an indication of critical-like behavior in fragile liquids and may explain the large deviation from the Arrhenius law [124].

Our analysis suggests that the correlation length behavior is opposite for strong and fragile liquids. There is an implication from the above analysis that strong liquids are distinguished from fragile liquids by occupying the opposite side of an underlying lambda transition. This scenario is shown schematically

4. Chapter: The glass transition and the order-disorder transition of $\text{Fe}_{50}\text{Co}_{50}$ and their relation with strong liquids

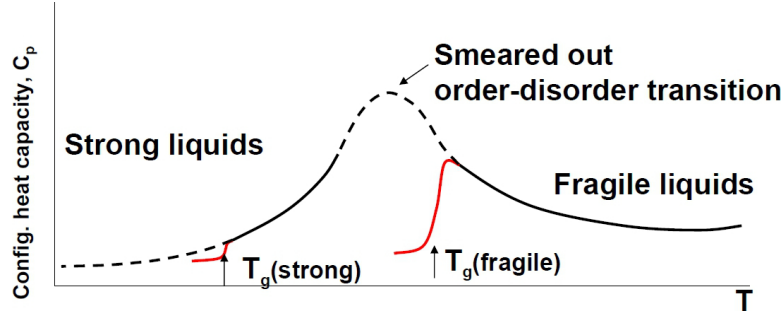


Figure 4.10: Schematic plot for strong vs. fragile behavior. The glass transition during order-disorder transition is related to strong liquid behavior in network glass-formers, which implies that strong and fragile liquids exist on opposite flanks of an underlying order-disorder transition.

in Fig. 4.10. Whether a liquid is seen to be strong or fragile depends on the observation window. For the liquid silica and BeF_2 , the observation window is on its lower temperature flank. Thus, they have decreasing specific heat capacities and decreasing correlation length towards T_g during cooling. In contrast, the observation window for fragile liquids are on the high temperature flank. Therefore, an increasing correlation length and specific heat capacity towards T_g is observed. The glass transition is just a timescale crossover during cooling, which can occur either in the strong or fragile liquid state, depending on system internal timescale, as schematically shown in Fig. 4.10. As long as a glass transition occurs, it makes the observation of the equilibrium state difficult due to the long annealing time for equilibration.

4.6 Summary

In this chapter, the glass transition phenomenon in the crystalline superlattice $\text{Fe}_{50}\text{Co}_{50}$ during an order-disorder (λ) transition is studied. It is found that the glass transition is a kinetic freezing-in of an ordering process. The temperature dependence of the structural relaxation time displays an ideal kinetically strong character in the sense of fragility. By re-scanning annealed samples, the specific heat capacity on long timescales is determined. It is shown that below the kinetic glass transition T_g there is no thermodynamic transition.

The behavior of the glass transition of $\text{Fe}_{50}\text{Co}_{50}$ is compared to the simulation results of the Jagla model for the liquid that has a liquid-liquid critical point. The similarities between $\text{Fe}_{50}\text{Co}_{50}$ and the simulated liquid with a critical point suggest that a liquid-liquid transition can be understood as an underlying λ transition, which can be a first-order, 2^{nd} -order (critical) or smeared

4. Chapter: The glass transition and the order-disorder transition of $\text{Fe}_{50}\text{Co}_{50}$ and their relation with strong liquids

out continuous transition, depending on where the pressure, at which the measurement is performed, lies with respect to the critical pressure. In light of the underlying lambda transition, explanations are provided for the anomalous specific heat capacity maximum in the simulations of liquid silica and BeF_2 . It is, therefore, argued that strong liquids have a decreasing static correlation length as T_g is approached from above, which is opposite to the findings of the increasing correlation length in fragile liquids.

This work provides an experimental parallel to the Jagla model that possesses a liquid-liquid critical point. It suggests that strong liquids may undergo a liquid phase change above T_g or even above the melting point at appropriate pressures. This stimulates our exploration for such a transition in a strong bulk metallic glass-forming liquid, presented in Chapter 7.

The behavior of the lambda transition can change with changing compositions. Chapter 5 presents the investigations on how the glass transitions can be affected by varying the lambda transition in the $(\text{FeCo})_{100-x}\text{Al}_x$ system, which will provide further insight into the thermodynamic and kinetic behavior of glass-formers.

Chapter 5

The relation between the order-disorder transition and the glass transition of $(\text{FeCo})_{100-x}\text{Al}_x$

In this chapter, the work described in Chapter 4 is continued. The thermodynamic and kinetic properties of different compositions of $(\text{FeCo})_{100-x}\text{Al}_x$ are investigated and the kinetic fragility of various compositions is derived. The cooperative effect on the specific heat capacity of the glass transition and the order-disorder transition in $(\text{FeCo})_{100-x}\text{Al}_x$ is studied and its implication for the cooperative phenomenon in glass-forming liquids are discussed.

5.1 Introduction

The binary $\text{Fe}_{50}\text{Co}_{50}$ alloy is the simplest case of ordering and disordering processes. It exhibits a 2^{nd} -order order-disorder transition (lambda transition) with a continuous enthalpy change. At the critical point of the transition, all response functions are diverging. The correlation length diverges at the critical temperature at 1003 K and ambient pressure. The glass transition in $\text{Fe}_{50}\text{Co}_{50}$ is characterized by a significant specific heat capacity (c_p) jump in the tail of the lambda peak.

With changing composition, the ordering and disordering can have a different behavior of the thermodynamics and kinetics. This raises the question how the lambda transition changes with its glass transition and whether the fragility becomes higher (more fragile) due to compositional changes. Answering these questions may shed light on the relation between the thermodynamic lambda transition and the kinetic glass transition. Moreover, the various compositions of superlattice alloys can be compared to the strong liquid systems, where an order

5. Chapter: The relation between the order-disorder transition and the glass transition of $(\text{FeCo})_{100-x}\text{Al}_x$

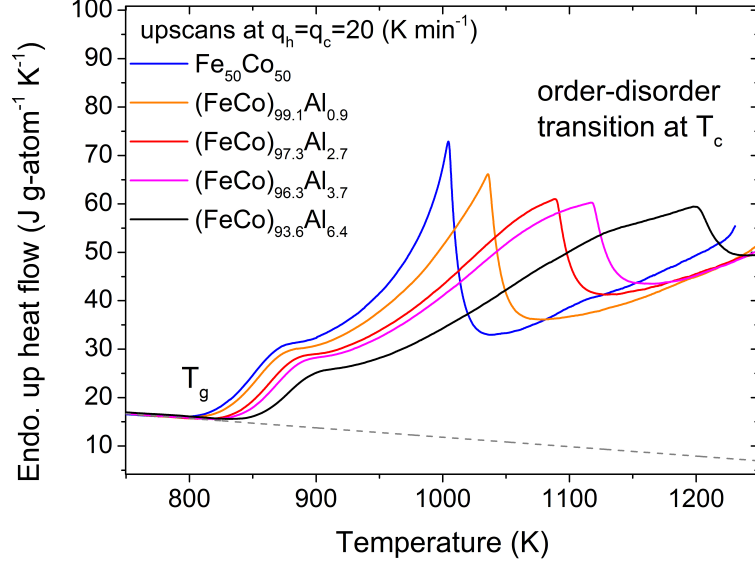


Figure 5.1: Glass transitions (T_g) and the lambda peaks (T_c) shift with aluminum concentration (in at. %) in $(\text{FeCo})_{100-x}\text{Al}_x$ upon up-scans at 20 K min^{-1} after previous down-scans at 20 K min^{-1} . The sudden jump in the heat flow at around 850 K is due to the ergodicity restoring, or glass transitions, where the systems regain thermal energy and return to their equilibrium states. The lambda-like peaks indicate the critical points of the order-disorder transitions. The dashed line is the assumed baseline, which is a linear extrapolation from the frozen-in states.

parameter is difficult to define.

In this work, the composition of the superlattice $\text{Fe}_{50}\text{Co}_{50}$ is changed by adding aluminum as a 3rd component. The superlattice structure is distorted and the lattice parameter is expanded. It is found that the shape of the specific heat capacity curve of the lambda transition changes with additional Al atoms. The cooperativity of ordering/disordering plays a key role in the variations of the lambda transition and also has a strong impact on the behavior of the glass transition, which provides a phenomenological analog to the cooperative phenomenon in strong liquids. However, the fragility of these compositions stays extremely strong, although the specific heat capacity jump at T_g is clearly weakened. This indicates that the cooperative behavior does not directly determine the kinetic fragility of the studied systems.

5. Chapter: The relation between the order-disorder transition and the glass transition of $(\text{FeCo})_{100-x}\text{Al}_x$

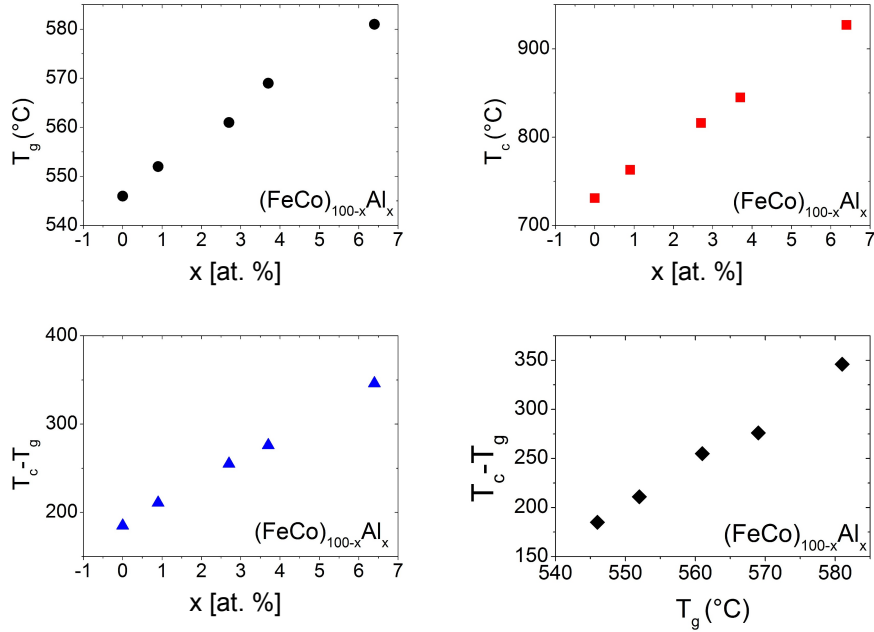


Figure 5.2: The transition temperatures vs. Al concentrations. T_g : glass transition temperature; T_c : critical temperature for the lambda transition.

5.2 Varying specific heat capacity peaks of glass transitions and order-disorder transitions

Figure 5.1 shows the heat flow of five compositions of $(\text{FeCo})_{100-x}\text{Al}_x$ where $x=0, 0.9, 2.7, 3.7$ and 6.4 , respectively. The large lambda-like peaks above 1000 K of the specific heat capacity are caused by the order-disorder transitions. The $(\text{FeCo})_{100-x}\text{Al}_x$ ($x=0$) has the sharpest lambda peak. With increasing molar fractions of Al, the lambda peaks are more and more smeared out and pushed to higher temperatures. The kinks at around 800 K are the relaxation processes of the frozen-in partially disordered structures. Upon upscans, they are unfreezings or "glass" transitions in the sense of ergodicity-restoring. As the lambda peaks are smeared out and pushed to higher temperatures, the glass transitions are also shifted to slightly higher temperatures and the magnitudes are weakened simultaneously. Figure 5.2 shows the relation between the transition temperatures and the Al concentrations. As shown in Fig. 5.3, the melting points slightly decrease while the lambda transition and glass transition temperatures increase.

Figure 5.4 shows the enthalpy changes ΔH during the lambda transitions assuming a baseline extrapolated from the heat flow of frozen-in states (see the

5. Chapter: The relation between the order-disorder transition and the glass transition of $(\text{FeCo})_{100-x}\text{Al}_x$

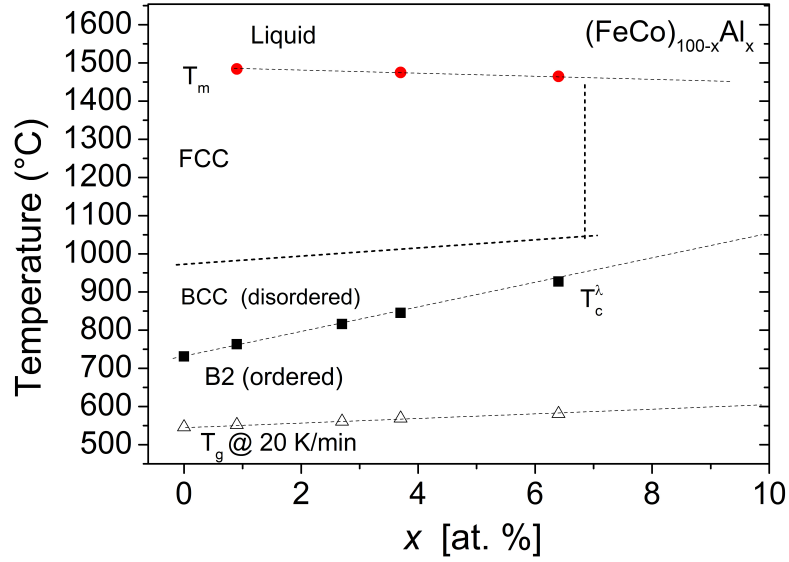


Figure 5.3: Phase diagram of $(\text{FeCo})_{100-x}\text{Al}_x$. T_m : melting temperature; T_c^λ : peak temperature of the lambda peak. T_g were measured at 20 K min^{-1}

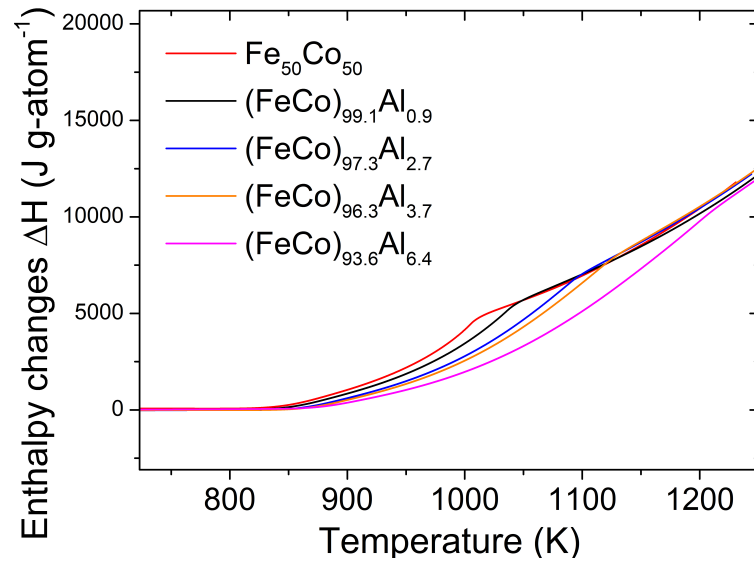


Figure 5.4: Enthalpy changes during the lambda transitions of $(\text{FeCo})_{100-x}\text{Al}_x$, assuming a linear baseline extrapolated from the frozen-in states.

5. Chapter: The relation between the order-disorder transition and the glass transition of $(\text{FeCo})_{100-x}\text{Al}_x$

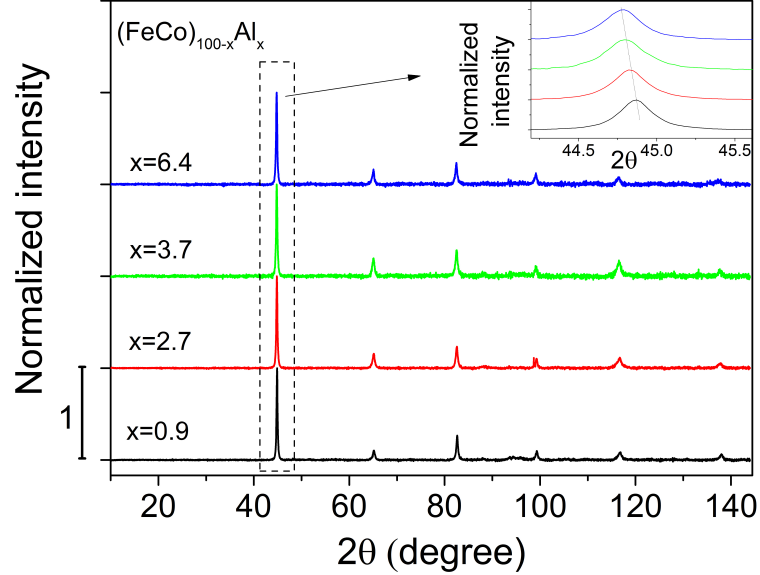


Figure 5.5: Normalized intensity for X-ray diffraction of the compositions of $(\text{FeCo})_{100-x}\text{Al}_x$. Inset: magnification of the first diffraction peaks.

dashed line in Fig. 5.1). A sharper c_p peak corresponds to a steeper increase in ΔH below the lambda transition temperature. At a high temperature around 1200 K, all ΔH converge and the enthalpy changes appear the same for all compositions. However, we note that the enthalpy increases only under the lambda peaks are different from each other. For example, at the end of the lambda peak of $\text{Fe}_{50}\text{Co}_{50}$, the enthalpy increase is around 5 kJ g-atom^{-1} , which is about only half of the enthalpy change of $11 \text{ kJ g-atom}^{-1}$, for the $(\text{FeCo})_{93.6}\text{Al}_{6.4}$ at the end of its smeared out lambda peak.

These changes in specific heat capacity are caused by the additions of Al atoms in the Fe-Co superlattice. X-ray diffraction measurements are shown in Fig. 5.5. The X-ray intensities are normalized to 1. By comparing the reflexes of the samples to databases, the reflexes of the crystalline structures are found to correspond to the body centered cubic structure. The inset shows the magnification of the first diffraction peaks at around $2\theta = 44 - 45^\circ$. We see that a system with a higher Al atoms concentration has a peak position that is shifted to a lower value of 2θ . This observation indicates the increase of the lattice parameters with increasing Al concentration in the superlattice. This suggests that Al atoms stretch and distort the lattice of the BCC or B2 structures. The systematic shift of the Bragg peaks also indicates that Al atoms are homogeneously and substitutionally distributed in the alloys.

5.3 Kinetics of the glass transitions

To investigate the kinetics of the glass transition of different compositions, we perform the so-called T_g -shift measurements in the high precision power compensated DSC. The samples are upscanned in the DSC with the same heating rate as they are cooled previously. Figure 5.6 shows that the glass transition temperature T_g is shifted to higher temperatures with increasing heating rate. The value of the fragility m from these scans can be determined based on the method, which was developed by Wang et al. [98] and applied for $\text{Fe}_{50}\text{Co}_{50}$ in Chapter 4. In their original paper, they propose to use only one selected heating rate (e.g., 20 K min^{-1}) after cooling at different cooling rates to determine the fictive temperature for each cooling rate by "area matching" with extrapolated the heat flow curves from the glassy state and the supercooled liquid state. The fictive temperatures are used to plot against the scaled heating/cooling rates to determine the fragility m . In the present work, we determine the onset temperature of the glass transitions graphically instead of determining the fictive temperature using the area matching method [98], because the latter requires the extrapolation of the heat flow to the equilibrium state below T_g and such an extrapolation needs a theoretical calculation using the Kirkwood theory for the order-disorder transition, which is difficult for complex ternary alloys, such as $(\text{FeCo})_{100-x}\text{Al}_x$. However, the $T_g(\text{onset})$ is a good approximation of the fictive temperature when the measurement is performed with $q_c = q_h$, as shown by a number of studies [3, 45]. Then, the scaled fictive temperatures, T_f , (or $T_g(\text{onset})$) vs. scaled cooling rates (in this case, $q_c = q_h$) are fitted by the linear function [98] (as derived in Chapter 3),

$$\log\left(\frac{q_c}{q_c^s}\right) = m - m\frac{T_f^s}{T_f},$$

where the standard cooling rate is $q_c^s = 0.333 \text{ K s}^{-1}$, and the standard fictive temperature T_f^s is the fictive temperature measured using the standard cooling rate. The coefficient m is the value of the steepness index of the fragility. Figure 5.7 shows the linear fits for the compositions of $(\text{FeCo})_{100-x}\text{Al}_x$ ($x = 0.9, 2.7, 3.7, 6.4$). The m values are determined and plotted against the Al concentration x , as shown in Fig. 5.8.

There is no significant influence of Al additions on the fragility. The changes of the fragility m are quite small and in the range of the experimental error. They are all close to $m = 16$, which means that they are very strong. The stretched lattice or potential distance does not seem to have a significant impact on the fragility. Therefore, the smearing-out of the lambda peak does not change the temperature dependence of structural relaxation time.

5. Chapter: The relation between the order-disorder transition and the glass transition of $(\text{FeCo})_{100-x}\text{Al}_x$

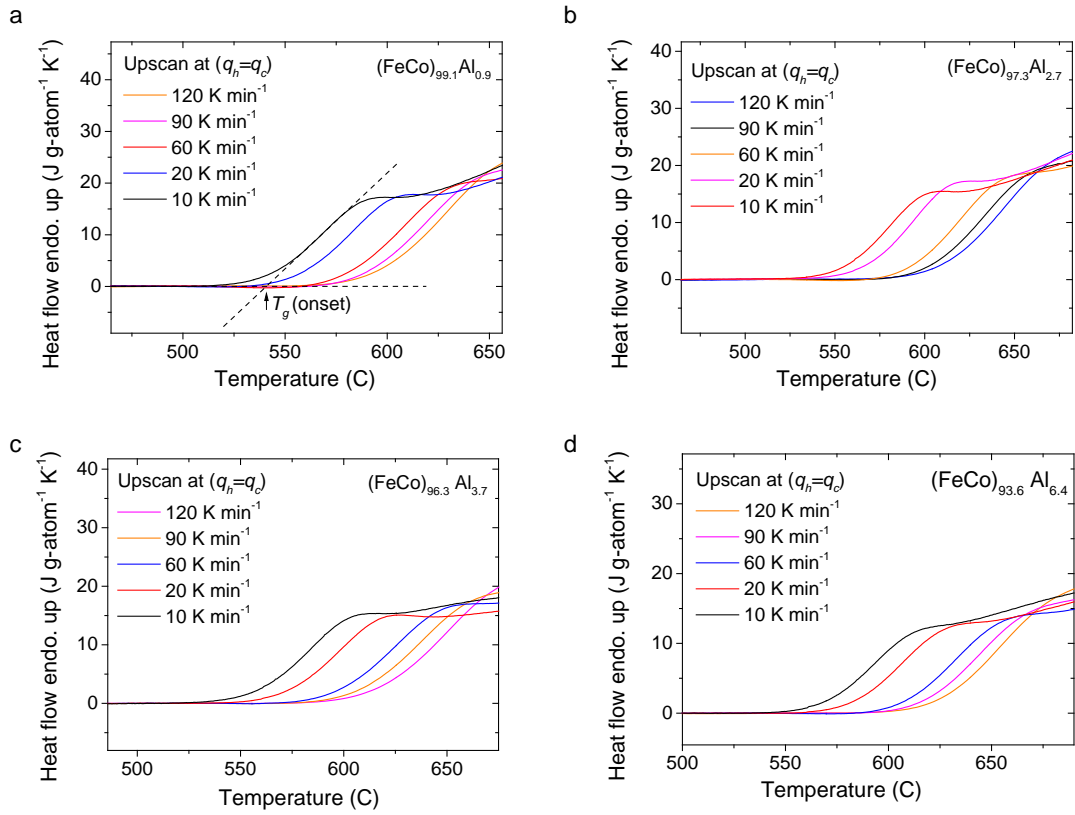


Figure 5.6: DSC upscans at the different heating rates (q_h) after cooling at the same rate (q_c) for $(\text{FeCo})_{100-x}\text{Al}_x$ ($x=0.9$ (a), 2.7 (b), 3.7 (c), 6.4 (d)). The $T_g(\text{onset})$ is determined graphically using a tangent construction, as shown in (a).

5. Chapter: The relation between the order-disorder transition and the glass transition of $(\text{FeCo})_{100-x}\text{Al}_x$

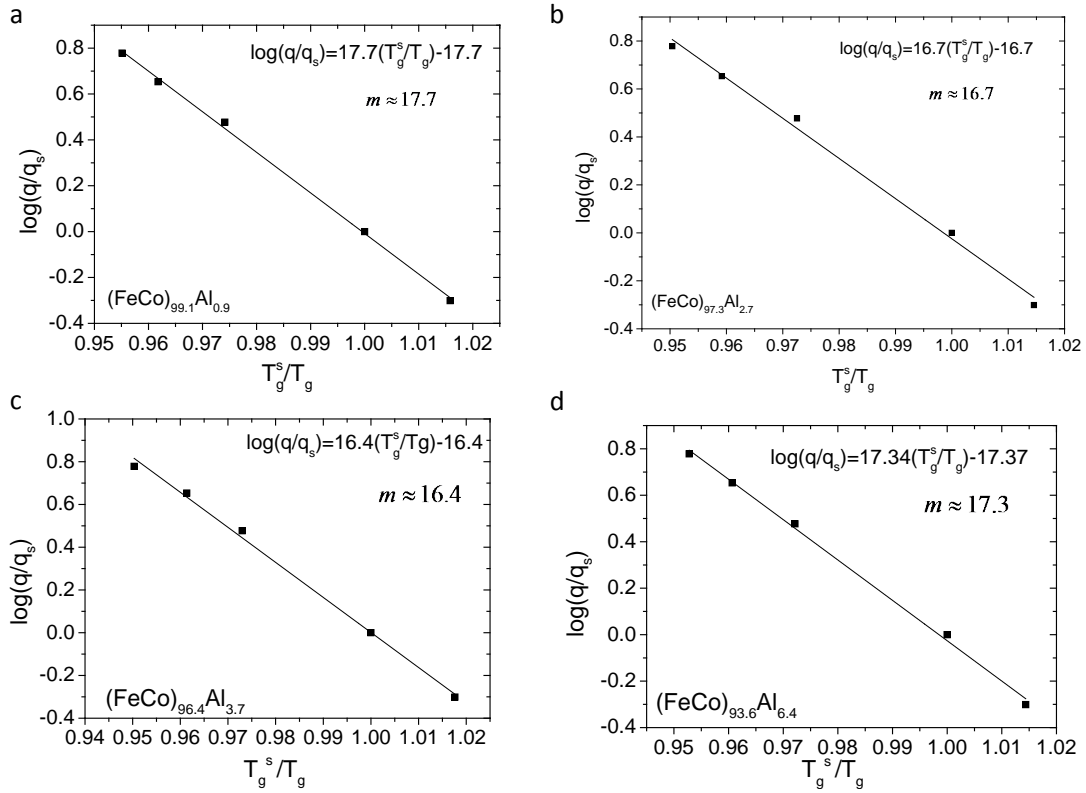


Figure 5.7: The determination of the values of the fragility m of $(\text{FeCo})_{100-x}\text{Al}_x$ ($x=0.9$ (a), 2.7 (b), 3.7 (c), 6.4 (d)) using DSC scans based on the method by Wang et al. [98]. q_s is the standard heating rate 20 K min^{-1} and T_g^s is the glass transition temperature corresponding to the standard heating rate. The values of m are around 16. Note that T_g is taken as $T_g(\text{onset})$ determined in Fig. 5.6 and is approximately equal to the fictive temperature T_f .

5. Chapter: The relation between the order-disorder transition and the glass transition of $(\text{FeCo})_{100-x}\text{Al}_x$

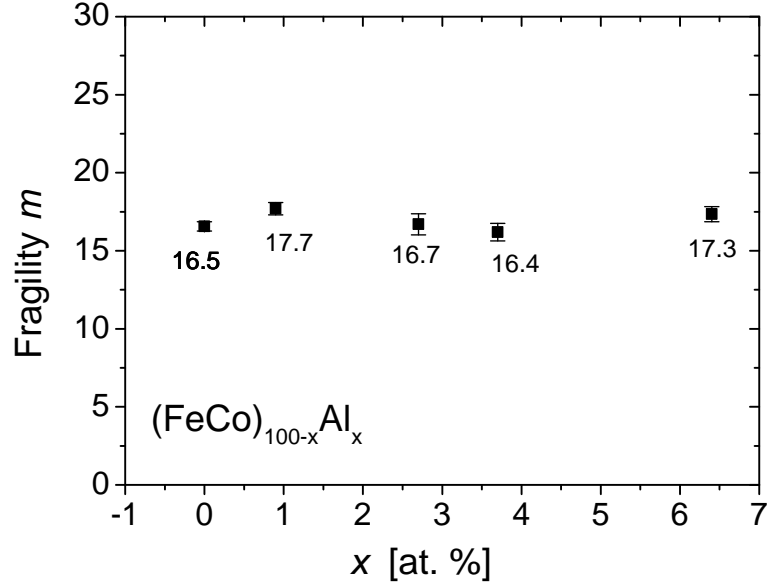


Figure 5.8: The values of the fragility m are determined using the method described in Fig. 5.7. These are plotted against the Al concentration of the $(\text{FeCo})_{100-x}\text{Al}_x$. The error bars are the standard deviations of the data fitting procedure.

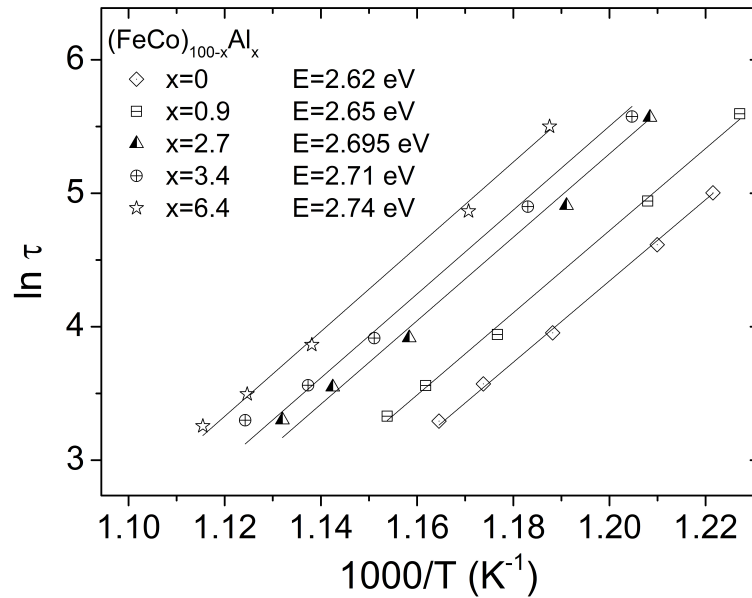


Figure 5.9: The structural relaxation time τ are fitted with the Arrhenius equation with a fixed pre-exponential factor of $\tau_0 = 1 \cdot 10^{-14}$ s. The fits yield the activation energy E for each alloy.

5. Chapter: The relation between the order-disorder transition and the glass transition of $(\text{FeCo})_{100-x}\text{Al}_x$

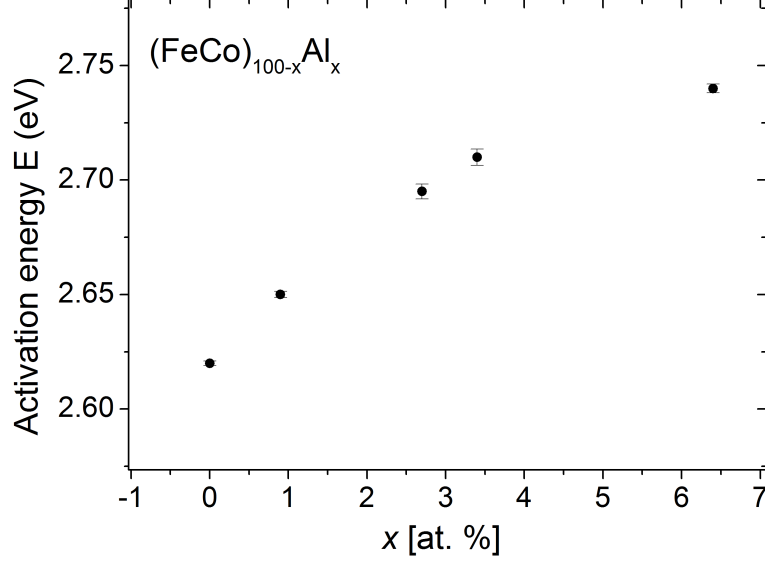


Figure 5.10: The relation between the activation energy E and the Al concentration, x . The error bars are the standard deviations of the data fitting procedure.

The characteristic structural relaxation time τ at the temperature $T_g(\text{onset})$ can be estimated using Eq. 3.4 [97]

$$\tau = (T_g^{\text{end}} - T_g^{\text{onset}})/q_h,$$

where the glass transition width $T_g^{\text{end}} - T_g^{\text{onset}}$ is divided by the heating rate q_h . The temperature dependence of the relaxation time can be fitted with the Arrhenius equation (Eq. 4.2)

$$\tau = \tau_0 \exp\left(\frac{E}{k_B T}\right),$$

where E is the activation energy and k_B Boltzmann constant. By fitting the structural relaxation time data, we obtain the activation energies for different compositions. We find that the activation energy for structural relaxation is slightly increasing with the increasing Al concentration in the $(\text{FeCo})_{100-x}\text{Al}_x$ solution. This increasing trend in activation energy is shown in the Fig. 5.10. The reason for this is probably the fact that the Al atoms stretch and distort the lattice and the Fe or Co atoms need more energy to overcome energy barriers and diffuse from their current sites to energetically favorable sites.

The high energy barriers slow down structural relaxations according to the Arrhenius equation. The rising of the activation energy is correlated with the higher glass transition temperature, because the system needs more thermal energy to overcome the higher energy barrier to reach the relaxation time of ~ 100 s at a higher temperature.

5.4 Links between the order-disorder transition, cooperativity and the liquid phase transition in strong liquids

The order-disorder transition is a typical cooperative phenomenon, where the ease of a transition increases rapidly with the extent to which it has already occurred [125]. Once some disorder is generated with increasing temperature, the additional disordering becomes much easier [126, 127]. This cooperative manner of transition can be understood based on the fact that an A-B atomic pair is energetically favored over an A-A or B-B atomic pair. Figure 5.11 shows a schematic representation of a simplified 2-D ideal superlattice of an AB alloy. It contains two sublattices labeled as α and β , respectively. All A atoms occupy the α sites and B atoms are on the β sites in the perfectly ordered state (Fig. 5.11a). Once a A atom on an α site (marked by the red circle) is replaced by a B atom, a slight disorder is generated in the system (Fig. 5.11b). Now the B atom is on the "wrong" site surrounded by β sites with B-atoms on them. However, the B-B atomic pair is less energetically favored than A-B. Therefore, it becomes now easier for one of the surrounding B atoms to be replaced by its neighboring A atom (see arrows in Fig. 5.11b). In this manner, some existed disorder promotes further disordering (Fig. 5.11c). Therefore, the increasing temperature with a constant rate causes more and more disorder, which is reflected by the more and more rapidly increased specific heat capacity before the critical point is reached. The shape of the specific heat capacity peak reflects the degree of the cooperativity of the order-disorder transition. A sharp lambda peak reflects a very cooperative manner of transition, for example, in the case of $\text{Fe}_{50}\text{Co}_{50}$. In the $(\text{FeCo})_{100-x}\text{Al}_x$ systems, the specific heat capacity peak is more smeared out with a higher Al content (Fig. 5.1), indicating a less cooperative effect in the system.

When a small amount of Al atoms is added into the $\text{Fe}_{50}\text{Co}_{50}$, the lattice is stretched and the average inter-atomic distance is increased, as verified by the XRD results shown in Fig. 5.5. Additionally, some sublattices sites are occupied by the Al atoms. The enthalpy of mixing of Fe and Al is -11 kJ mol^{-1} . For Co and Al, it is -19 kJ mol^{-1} . Both are strongly negative. Therefore, no matter if an Al atom has the neighbor Fe or Co atoms, it is on its energetically favorable "right" site. In such a system, when some disorder occurs for Fe and Co atoms, the cooperative manner of disordering is less than in the binary $\text{Fe}_{50}\text{Co}_{50}$, because there are some Fe or Co atoms surrounding Al atoms, which do not contribute to the cooperative action. As a consequence, the lambda c_p peak is smeared out and separated farther from T_g ; furthermore, the c_p jump at T_g is also weakened.

Accordingly, the anomalous behavior of the specific heat capacity of liquid

5. Chapter: The relation between the order-disorder transition and the glass transition of $(\text{FeCo})_{100-x}\text{Al}_x$

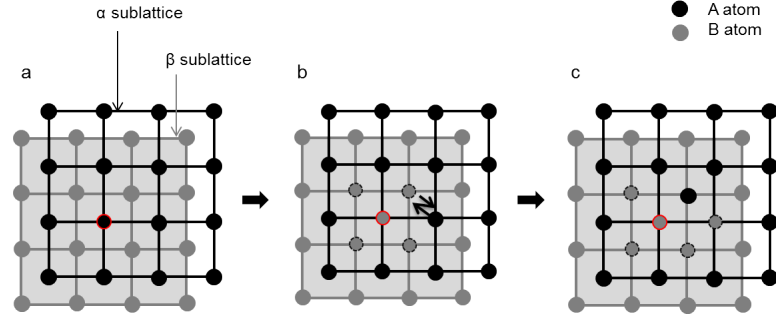


Figure 5.11: Schematics for the cooperative phenomenon in a 2-D superlattice AB alloy system. (a) A atoms and B atoms are on the α and β sublattices, respectively, in the perfectly ordered state. (b) When a A atom is replaced by a B atom (marked by the red circle), the surrounding B atoms become less energetically favorable and tend to be replaced by other neighboring A atoms. (c) The system is more disordered promoted by the initial disordering.

SiO₂ and Si may be explained by the different degree of the cooperativity of an underlying order-disorder transition. SiO₂ is found to have a smeared out specific heat capacity maximum and a strong-fragile transition at a high temperature (>4000 K [87, 71]) far above the T_g , indeed, above its melting point; while Si is reported to have a first-order liquid-liquid transition with a sharp heat capacity maximum in the supercooled liquid region (~ 1060 K at 0 pressure [80]). The distinct specific heat capacity behavior suggests that liquid SiO₂ undergoes a liquid phase change with a less cooperative action of the ordering/disordering, whereas liquid Si exhibits a highly cooperative manner of the ordering/disordering process. However, the cooperative phenomenon in liquid SiO₂ and Si is not due to "unlike" or "like" atomic pairs, as being seen in the simple case of the superlattice alloy. An understanding of the cooperative phenomenon of liquids on the atomic level has not been reached, as the order parameter in liquids is difficult to define.

Angell and coworkers [61, 64] have developed a thermodynamic model, the lattice-bonds excitation model, that incorporates the cooperative phenomenon into the thermodynamic description of glass-forming liquids. The interaction of atoms or molecules of a liquid is modeled by the excitations of quasi-lattice bonds. When a glass is heated above the glass transition, the quasi-lattice bonds are excited with increasing temperature. The mixing of the domain of the excited state and the domain of the non-excited state gives rise to a c_p level-up. The c_p may exhibit a bump-like shape, depending on the excitation enthalpy ΔH^* and the excitation entropy ΔS^* . The model has to take the cooperativity of the excitation into account to simulate the specific heat capacity of the liquid in reality. With a cooperative term in their equation, the c_p above T_g is promoted, which is more close to experimental data (see Fig. 2.13 and 2.14). Furthermore,

5. Chapter: The relation between the order-disorder transition and the glass transition of $(\text{FeCo})_{100-x}\text{Al}_x$

a strong cooperativity of the excitation may raise a sharp c_p peak and produce a singularity that is associated with a phase transition in the liquid. The lattice-bonds excitation model has been used to explain the heat capacity anomaly in water, Si, SiO_2 and BeF_2 . According to the model, the temperature of the c_p maximum depends on the ratio, $\Delta H^*/\Delta S^*$. The magnitude of the c_p maximum only depends on ΔS^* . Therefore, a weak cooperativity of the excitation raises a small magnitude of the c_p maximum and has a small ΔS^* . As a consequence, the $\Delta H^*/\Delta S^*$ is large, which leads to a high temperature of the c_p maximum. In this light, the high temperature of the c_p maximum of SiO_2 and BeF_2 is explained by the weak cooperativity of the quasi-lattice bonds excitation. In liquid Si and Ge, the relatively low temperature of the liquid-liquid transition with respect to T_g is attributed to a strong cooperativity of the excitation [80, 82]. This is consistent with the conclusion obtained by comparing the liquids having heat capacity anomalies with the phenomenological analog system, $(\text{FeCo})_{100-x}\text{Al}_x$, in which the cooperative phenomenon is well understood.

The fragility of a liquid (or, at least, fragile liquids) is considered to be related to the cooperativity of the atomic rearrangement according to the Adam-Gibbs description of liquid dynamics, in which the fragility is determined by the rate of increase of TS_c , where S_c is the configurational entropy. A rapid change of TS_c also indicates more and more cooperative motions of atoms at lower and lower temperatures as approaching T_g . Usually, the higher rate TS_c changes, the more fragile the system is [65, 53]. Analogously, a rapid change of TS_c of $(\text{FeCo})_{100-x}\text{Al}_x$ below the lambda heat capacity peak is associated with a large cooperative ordering/disordering. The c_p jumps become systematically weaker (or larger) when less (or more) cooperative behavior is involved. However, the fragility of $(\text{FeCo})_{100-x}\text{Al}_x$ does not change. This observation implies that fragility is not always correlated with cooperative effects. As found in the studies of c_p jumps at T_g for a variety of glass-formers, there is a general trend that a larger jump in c_p at T_g is associated with a more fragile liquid [6, 98, 60] in non-polymeric glass-formers. However, some exceptions from the trend do exist [60]. There must be other factors involved for the determination of the fragility.

5.5 Summary

In this chapter, we have extended our investigation from Chapter 4 to the thermodynamic and kinetic properties of different compositions of the ternary system $(\text{FeCo})_{100-x}\text{Al}_x$. We find that with increasing Al concentration, the glass transition is weakened and shifted to higher temperatures separating farther from the order-disorder transition that is even pushed to more higher temperatures, although the kinetic fragility is not changed in the studied systems. The specific

5. Chapter: The relation between the order-disorder transition and the glass transition of $(\text{FeCo})_{100-x}\text{Al}_x$

heat capacity behavior of the order-disorder transition in $(\text{FeCo})_{100-x}\text{Al}_x$ systems is explained by the cooperative phenomenon disturbed by the added Al atoms. By comparing the specific heat capacity of $(\text{FeCo})_{100-x}\text{Al}_x$ with that of SiO_2 and Si, the anomalous specific heat capacity behavior of SiO_2 and Si is attributed to different degrees of the cooperative manner of the liquid phase transition, which is consistent with the implication of the lattice-bonds excitation model.

Chapter 6

Determination of fragility from single DSC-scans

In this chapter, the glass transition of bulk metallic glasses with various fragilities as well as strong oxide glasses is studied using differential scanning calorimetry (DSC). It is found that the liquid fragility determined from viscosity measurements is correlated with the scaled maximum slope of the DSC heat flow during the glass transition. The slope reflects the rate of the change of effective free energy barriers in the potential energy landscape during the glass transition. The correlation of this slope with fragility is a manifestation that a high-fragility system has high enthalpy barriers; however, its effective free energy barriers are low above T_g and high below T_g due to the different entropy effects. A comparison is made between the correlation found in this work and those correlations with fragility from previous studies on other classes of glass-formers.

6.1 Introduction

The laboratory glass transition observed on cooling is a kinetic freezing-in of the structural relaxation process as the system's internal time scale crosses the experimental time scale. As the glass transition temperature, T_g , is approached during cooling, the relaxation time, τ , (or viscosity, η) of the undercooled liquid changes with temperature following different patterns for different liquids. This is the basis of the "fragility" concept, proposed by Angell, [6] to describe different scaling behaviors of the relaxation times of undercooled liquids with respect to temperature. For fragile liquids (e.g., o-terphenyl), the relaxation time varies in a strongly non-Arrhenius fashion; whereas strong liquids, such as GeO_2 and SiO_2 , exhibit an Arrhenius-like behavior of the relaxation time [128]. A kinetic fragility, or steepness index, m , is defined [6] as the slope of $\log_{10}\tau$ vs. T_g/T at the glass

6. Chapter: Determination of fragility from single DSC-scans

transition temperature T_g (Eq. 2.1)

$$m = \left. \frac{d \log_{10} \tau}{d(T_g/T)} \right|_{T=T_g},$$

where the scaling parameter T_g is commonly chosen at the temperature, where the structural relaxation time is around 100 s, which is the value conventionally adopted in defining the fragility m [6, 51]. This value of T_g corresponds to the onset of the glass transition measured at a heating rate of 20 K min⁻¹ using calorimetric methods [98] and has also been established to coincide with the temperature, at which the equilibrium viscosity is 10¹² Pa s [129].

Kinetically strong and fragile liquids are observed to have small and large values of m , respectively. The temperature dependence of η (or τ) can be described with the empirical Vogel-Fulcher-Tammann (VFT) equation, [35, 36]

$$\eta = \eta_0 \exp\left(\frac{D^* T_0}{T - T_0}\right), \quad (6.1)$$

where the pre-exponential factor η_0 is the theoretical infinite-temperature limit of the viscosity [130]. T_0 and D^* are fitting parameters. The VFT-fragility parameter D^* is an alternative description of the fragility of the liquid and can be related to the steepness index m by the equation [51]

$$D^* = 590/(m - 17), \quad (6.2)$$

where the constant 17 is the minimum value of m for D^* determined from viscosity data as the viscosity changes by 17 orders of magnitude for all liquids from T_g ($\eta(T_g) \sim 10^{12}$ Pa s) to the infinitely high temperature limit ($\sim 4 \times 10^{-5}$ Pa s). The constant changes to 16 for the D^* determined from relaxation time data [51].

Although efforts have been devoted toward describing the fragility using various phenomenological models [48], its origin still remains elusive. The fragility of a liquid can be determined from pure kinetic data; e.g., viscosity or relaxation time. It is, however, known to correlate with other physical properties of glass-formers [8, 53, 60, 131, 59]. The fragility has been found to be correlated with the thermodynamics of supercooled liquids [53]. The temperature dependence of the scaled excess entropy, for example, has been shown to have the similar temperature-scaling behavior as that of the relaxation time and can be used to define a thermodynamic fragility [53]. The specific heat capacity jumps ΔC_p at T_g scaled by entropy of fusion S_m are found to correlate with the fragility of 54 non-polymer glassformers [60]. Recently, an enthalpy hysteresis during cooling and heating throughout the glass transition has been reported to correlate with the fragility of molecular glass-formers [131]. However, we realize that in some metallic glass compositions the enthalpy hysteresis is difficult to establish due to

the interference of crystallization that can occur shortly after the completion of the glass transition. In such cases this can lead to an increasing uncertainty in the correlation. There is a well known relation derived by Moynihan [129] that the fragility is correlated with the reduced glass transition width, $\Delta T_g/T_g$, as measured using DSC [129, 8]; however, the extent of deviation from this relation is not trivial [8]. A theoretical approach to fragility has been taken by Mauro et al. [132], who calculate the viscosity of liquid selenium using a model that combines the enthalpy landscape approach with non-equilibrium statistical mechanics [133]. In their simulation, they manipulate the fragility of selenium while keeping a constant T_g . It is shown that a higher fragility leads to a sharper turn of the enthalpy-temperature curve of the selenium at the same T_g .

Here, we investigate how fragility relates to the DSC heat flow during the glass transition in bulk metallic glass and oxide glass systems with different T_g . We find that kinetically fragile glass-formers exhibit a steeper slope of the T_g -scaled DSC heat flow signal than kinetically stronger ones. The slope reflects the rate of the change of effective free energy barriers in the potential energy landscape during the glass transition. The correlation between this slope and fragility is a result of the difference in topology of the potential energy landscape of fragile and strong systems. This work also explains why the correlation of fragility with either $\Delta C_p(T_g)$ or $\Delta T_g/T_g$ is rather qualitative.

6.2 Fragility and T_g -scaled slope of DSC scans

The preparations of amorphous samples of $Zr_{41.2}Ti_{13.8}Cu_{12.5}Ni_{10}Be_{22.5}$ (Vit.1), $Zr_{44}Ti_{11}Ni_{10}Cu_{10}Be_{25}$ (Vit.1b), $Zr_{46.75}Ti_{8.25}Cu_{7.5}Ni_{10}Be_{27.5}$ (Vit.4), $Zr_{58.5}Cu_{15.6}Ni_{12.8}Al_{10.3}Nb_{2.8}$ (Vit.106a), $Au_{49}Cu_{26.9}Si_{16.3}Ag_{5.5}Pd_{2.3}$ (Au₄₉-BMG) and $Pd_{43}Cu_{27}Ni_{10}P_{20}$ (Pd₄₃-BMG) as well as B_2O_3 and GeO_2 are described in Chapter 3. The calorimetric measurements are performed in a power-compensated Perkin-Elmer Diamond DSC in aluminum or gold pans under a constant flow of high-purity argon. The glass transition temperature T_g is defined as the onset of the endothermic DSC event observed upon heating throughout the glass transition at a constant rate which is kept identical to the previous cooling rate.

Amorphous samples are upscanned in the DSC at 60 K min^{-1} throughout the glass transition after an initial cooling at the same scanning rate of 60 K min^{-1} from the supercooled liquid. The heating rate is kept the same as the preceding cooling rate ($q_h = q_c$) in order to avoid the uncertain influence of the thermal history. For each up-scan of the amorphous alloy sample, a scan of the crystallized sample is also performed to serve as the corresponding baseline. For amorphous B_2O_3 and GeO_2 , the crystalline baselines are estimated by linear extrapolations from the values of the glassy states due to the difficulty to crystallize these samples

6. Chapter: Determination of fragility from single DSC-scans

<i>materials</i>	$T_g(K)$ at 60 K min ⁻¹	$\left. \frac{d\Delta C_p^{l-x}}{d(T/T_g)} \right _{max}$	VFT D^*	fragility m
Pd ₄₃ -BMG	583	591	12	65 ^a
Au ₄₉ -BMG	403	464	16.9 ^b	51.9
Vit.106a	671	410	21.7 ^c	44.2
Vit.4	626	345	22.1 ^d	43.7
Vit.1b	624	360	25.4 ^e	40.2
Vit.1	631	288	26 ^f	39.7
B ₂ O ₃	575	260	36	32 ^g
GeO ₂	839	50	163	20 ^g

Table 6.1: Glass transition, maximum slope of T_g -scaled DSC scans and fragility parameters. The calorimetric glass transition temperatures T_g are measured at 60 K min⁻¹ after preceding cooling at 60 K min⁻¹ from the supercooled liquid region. The T_g -scaled maximum slopes are obtained by taking the maximum derivative of the heat flow during the glass transition multiplied by the respective absolute T_g (K). The conversion between m and the VFT parameter D^* is done using Eq. 6.2 from ref. [3]. ^aFan et al. [134] (2004). ^bEvenson et al. [135] (2013). ^cEvenson et al. [97] (2010). ^dBusch et al. [136] (2001). ^eEvenson et al. [137] (2011). ^fWay et al. [68] (2007) (The fragility of Vit.1 was first determined to be $D^* = 18.5$ by Waniuk et al. [138] and $D^* = 23.8$ by Mukherjee et al [139]. But recently Way et al. [68] measured the high-temperature viscosity and a VFT fit of combined viscosity data of both temperature ranges gives a larger value of $D^* = 26$.). ^gBöhmer et al. [128] (1993).

6. Chapter: Determination of fragility from single DSC-scans

in the DSC. The relatively high heating/cooling rate (60 K min^{-1}) is selected here so as to avoid crystallization due to the limited thermal stability of certain BMG compositions.

After subtracting the crystalline baselines, the DSC up-scan output, $d\Delta Q/dt$ ($\text{J g-atom}^{-1} \text{ s}^{-1}$) is divided by the rate, dT/dt , yielding $(d\Delta Q/dt)/(dT/dt) = d\Delta Q/dT$, which is the heat flow in a dimension of $\text{J g-atom}^{-1} \text{ K}^{-1}$; in other words, it is the heat difference in Joules between liquid and crystal per g-atom per Kelvin; this is proportional to the apparent excess specific heat capacity, $d\Delta Q/dT = \kappa \Delta C_p^{l-x}$, where $l-x$ represents the difference between liquid and crystal. As the sensitivity of the DSC is calibrated [95], the constant κ is assumed to be 1 in the following discussion. In Fig. 6.1, the heat flow is plotted against the absolute temperatures scaled by the measured values of the respective onset of T_g . The maximum values of the slopes on the T_g -scaled heat flows during glass transitions are then determined as the characteristic slopes for the glass transitions. Table 6.1 summarizes the maximum slopes $d(\Delta C_p^{l-x})/d(T/T_g)|_{max}$.

In Fig. 6.2, the metastable equilibrium viscosity data of these bulk metallic glass-formers measured using three-point beam bending are displayed in a T_g -scaled Arrhenius plot (also called fragility-plot). The solid lines represent the VFT fit, yielding the VFT fragility parameter, D^* . All multicomponent Zr-based bulk metallic glass-formers show similar strong behavior ($D^* \sim 20-26$), while the Au_{49} -BMG ($D^* = 16.9$) and Pd_{43} -BMG ($D^* = 12$) are somewhat more fragile.

Figure 6.3 shows the relation between the maximum slope of the T_g -scaled DSC heat flow during the glass transition and the inverse VFT-fragility parameter, $1/D^*$. The slope for the very fragile four-component Pd_{43} -BMG is greater than the less fragile five-component Au_{49} -BMG, both of which have greater slopes than the relatively stronger Zr-based BMGs. Moreover, we include the calorimetric measurements for the network oxide glass-formers B_2O_3 and GeO_2 . The results extend the correlation towards the further strong extreme of the strong-fragile pattern; i.e., to larger values of D^* . Clearly, a system with a higher fragility exhibits a greater slope of the T_g -scaled DSC heat flow signal during the glass transition. We find the relation between the slope of the T_g -scaled heat flow and $1/D^*$ can be described by a simple proportional function (see the dashed line in Fig. 6.3),

$$\left. \frac{d\Delta C_p^{l-x}(T)}{d(T/T_g)} \right|_{max} = \frac{a}{D^*}, \quad (6.3)$$

with a proportional coefficient $a = 7803 \pm 290 \text{ J g-atom}^{-1} \text{ K}^{-1}$.

We wish to emphasize that the scaling parameter, T_g , is essential to the demonstrated correlation, because the fragility concept is defined in such a way that the deviation of the dynamic properties from the Arrhenius law from the infinitely

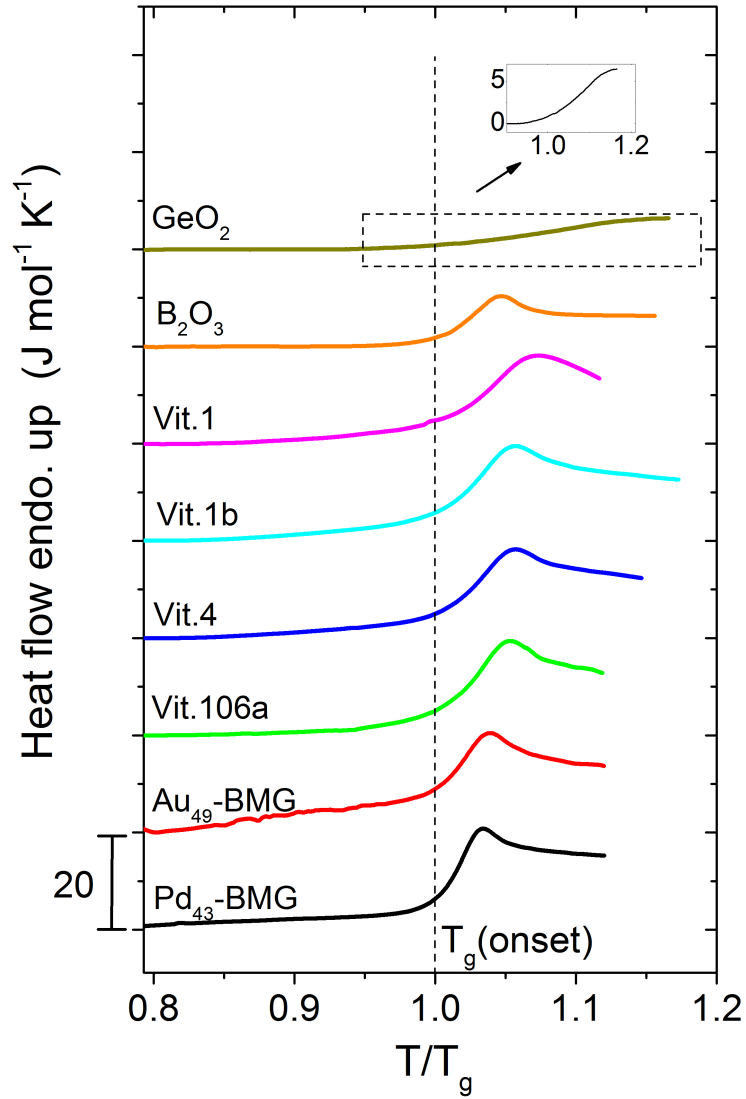


Figure 6.1: Heat flow after subtracting baselines (per mole of atoms) measured by DSC up-scans at 60 K min^{-1} after a preceding cooling at 60 K min^{-1} ($q_h = q_c$) for BMGs as well as oxide glasses. The curves are vertically shifted by $20 \text{ J mol}^{-1} \text{ K}^{-1}$ for clarity. The GeO2 curve displays a very weak glass transition that is almost invisible on the regular scale.

6. Chapter: Determination of fragility from single DSC-scans

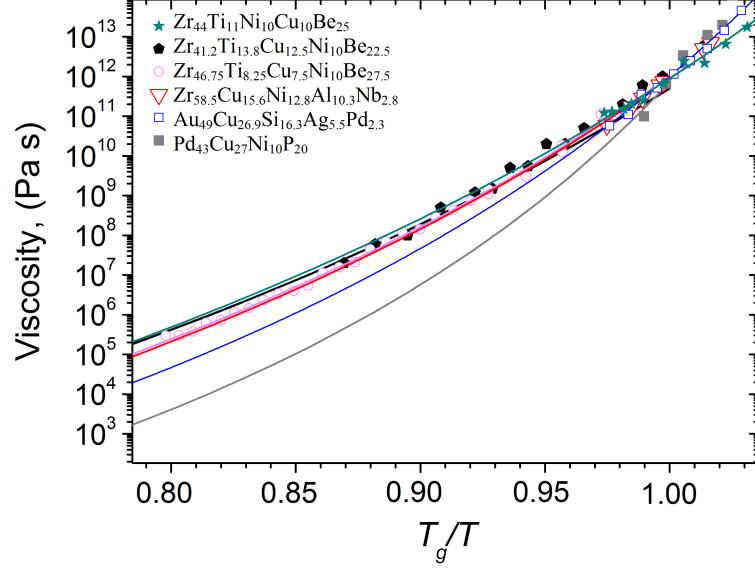


Figure 6.2: Fragility-plot of the studied BMG-forming systems. The viscosity data are obtained from three-point beam bending measurements from various sources (see Tab. 6.1). The solid curves are calculated via the VFT equation using the parameters given by literatures (see ref. in Tab. 6.1). The glass transition temperature T_g is defined as the temperature where the viscosity value is $\sim 10^{12}$ Pa s.

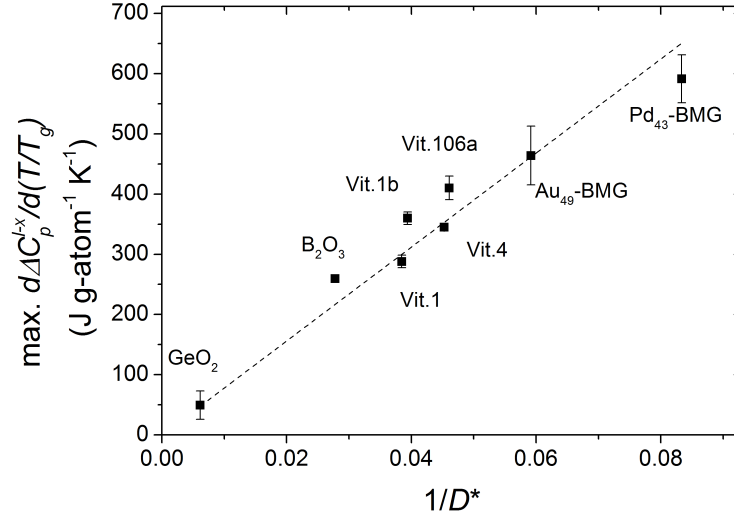


Figure 6.3: Correlation between the inverse fragility parameter, $1/D^*$, and the maximum slope of the T_g -scaled DSC heat flow during the glass transitions in bulk metallic and network glasses. The error bars indicate the experimental uncertainty in determining the maximum slope.

6. Chapter: Determination of fragility from single DSC-scans

high temperature down to T_g . Accordingly, the T_g -scaled temperature allows us to compare the properties of various systems near different T_g to reflect their extents of deviation from the Arrhenius law. Although T_g in this work is obtained at a scanning rate of 60 K min^{-1} , any other scanning rate should yield a similar linear correlation as long as the same rate is applied for all materials. In such a case, the value of the proportional coefficient a may slightly change. Zheng et al. [140] have recently reported on the fragility of a series of sodium borosilicate glasses, in which it was noticed that there is an increasing trend of the values of m with the increasing slope of the rising C_p at the inflection point during the glass transition. However, T_g was not taken into account in their work. If the values of T_g do not change much for similar compositions, neglecting T_g is a first approximation of the correlation in Eq. 6.3.

Even though we are comparing two different classes of structural glasses (BMGs and network glass-formers), we nevertheless see that they can be described using the method introduced. The question arises why the slope of the heat flow versus T/T_g appears to correlate so well with the liquid fragility in these cases. The apparent excess specific heat capacity, ΔC_p^{l-x} , is the derivative of the excess enthalpy, ΔH^{l-x} , with respect to temperature, $\Delta C_p^{l-x} = d(\Delta H^{l-x})/dT$. Then, Eq. 6.3 can be rewritten

$$\left. \frac{d^2(\Delta H^{l-x})}{dT^2} \cdot T_g \right|_{max} \propto \frac{1}{D^*}, \quad (6.4)$$

where $d^2(\Delta H^{l-x})/dT^2$ is the maximum curvature of the temperature dependence of the excess enthalpy during the glass transition. A larger curvature or sharper turn of the ΔH^{l-x} vs. T curve during the glass transition would indicate a higher fragility of the system for the same T_g .

The above described relation can be explained using the theoretical model of Mauro et al. [133, 132] developed for the glass transition of selenium based on the enthalpy landscape approach [46], in which the viscosity of a glass-former can be calculated. Mauro et al. have found that the viscosity as well as fragility depends on the effective transition rate $K_{\beta\gamma}$ from basin β to basin α in the potential energy landscape. $K_{\beta\gamma}$ is dominated by the exponential changes in the enthalpy barriers and the degeneracy values of the inherent structures (configurational entropy) [133, 132]. A high-fragility system has high enthalpy barriers and a high configurational entropy before ergodicity-breaking. Above T_g , the system is free to visit a large number of available transition states. Thus, the configurational entropy dominates the contribution to the effective free energy barrier for structural relaxation. As a consequence, a high-fragility system with the high configurational entropy has a low effective free energy barrier for relaxation. Therefore, the system can more closely follow the equilibrium properties of the supercooled liquid

above T_g [132].

However, below T_g , the system is trapped in a subset of the overall phase space, a so-called "metabasin", and the total number of available transition states is small. Hence, the entropy effect does not play a main role and the effective free energy barrier for structural relaxation is now dominated by enthalpy barriers [132]. A high-fragility system has high enthalpy barriers and, thus, its effective free energy barrier below T_g is also higher as compared to a strong system. Therefore, properties like enthalpy and volume exhibit a sharper departure from the equilibrium properties of the supercooled liquid as long as the system is trapped in metabasin at T_g . Although this explanation is based on the simulation of selenium [132], the same phenomenon found in the metallic and oxide glasses suggests that the two mechanisms (i.e., enthalpy barriers and entropy) of determining fragility should also apply to the present systems.

6.2.1 Comparison with other fragility-related correlations

In Fig. 6.4a, the specific heat capacity difference at glass transition temperatures [$\Delta C_p(T_g) = C_p^l(T_g) - C_p^{gl}(T_g)$] scaled by the entropies of fusion, $\Delta C_p(T_g)/\Delta S_m$, are plotted ¹ against inverse VFT-fragility parameters $1/D^*$. We note that the discrepant values of entropy of fusion are reported for Au₄₉-BMG and Pd₄₃-BMG. This leads to different values of $\Delta C_p(T_g)/\Delta S_m$ for these two alloys in the plot. Wang et al. [60] studied 54 non-polymer glassformers and found a proportional relation between $\Delta C_p(T_g)/\Delta S_m$ and m :

$$\frac{\Delta C_p(T_g)}{\Delta S_m} = \frac{m}{40}. \quad (6.5)$$

In the above relation, the term on the left side has been shown [60] to be approximately equal to the slope of the $\Delta S(T)/\Delta S_m$ vs. T/T_m plot (also called Kauzmann plot [47]) at T_g in the supercooled liquid region, assuming a constant $T_g/T_m = 2/3$ [60]. The Kauzmann plot can be viewed as a thermodynamic equivalent of the kinetic fragility [60, 8]. In Fig. 6.4b, the non-polymer glassformers studied by Wang et al. [60] are compared with the substances investigated in this work. It is noticed that the Zr-BMGs appear to have the higher values of $\Delta C_p(T_g)/\Delta S_m$ by around 200% than expected from the linear relation proposed by Wang et al [60].

¹Note that $\Delta C_p(T_g)$ and ΔT_g of Vit.1 is difficult to determine graphically from the heat flow in Fig. 6.1 because Vit.1 crystallizes immediately above the glass transition, leaving no overshoot and no stable supercooled liquid region on the upscan. This introduces error in the extrapolation from the supercooled liquid states. Therefore, the case of Vit.1 is not considered in Figs. 6.4 and 6.5.

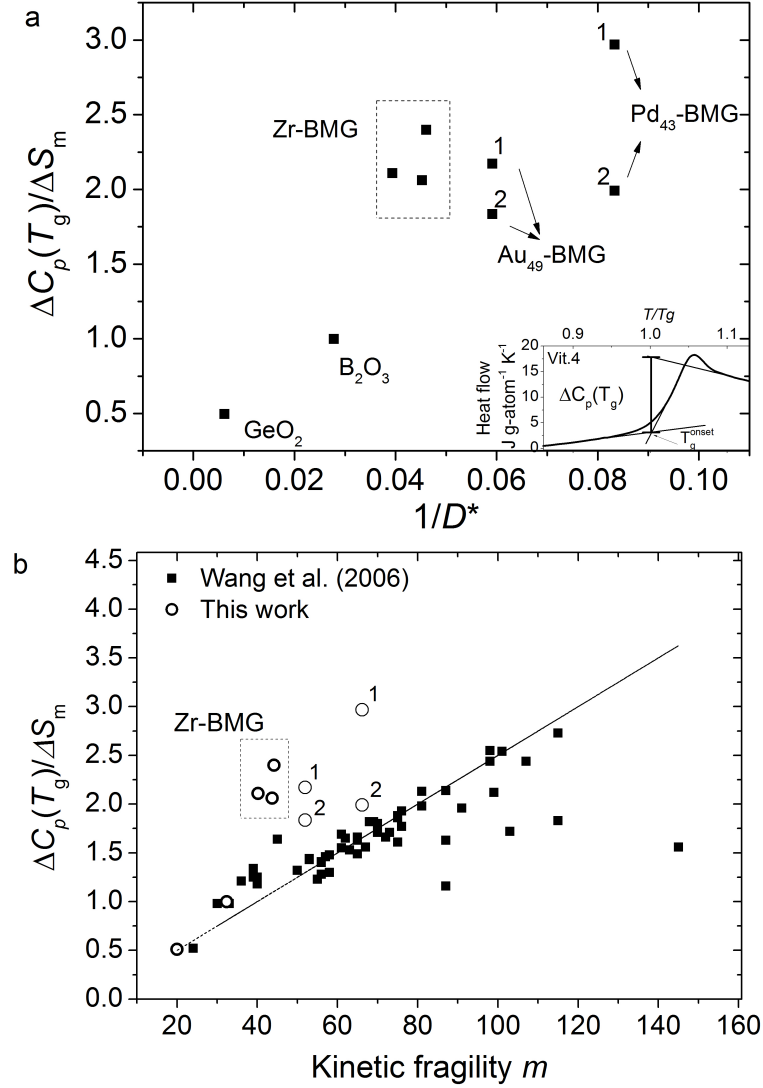


Figure 6.4: Fragility vs. $\Delta C_p(T_g)$ scaled by ΔS_m . (a) $1/D^*$ is the inverse VFT-fragility parameter obtained from viscosity measurements (Fig. 6.2). The numbers (1,2) represent the discrepant data for Au_{49} -BMG and Pd_{43} -BMG, respectively, due to the different ΔS_m values reported by different sources (Au_{49} -BMG (1): [141]; Au_{49} -BMG (2): [135]; Pd_{43} -BMG(1): [142]; Pd_{43} -BMG(2): [134]). (b) Comparison between the substances studied by Wang et al. [60] (solid symbols) and this work (open symbols). The values of m of studied metallic glasses is converted from D^* using Eq. 6.2. Zr-BMGs appear to have larger values than expected from the linear fit for 54 non-polymer substances studied by Wang et al. [60].

6. Chapter: Determination of fragility from single DSC-scans

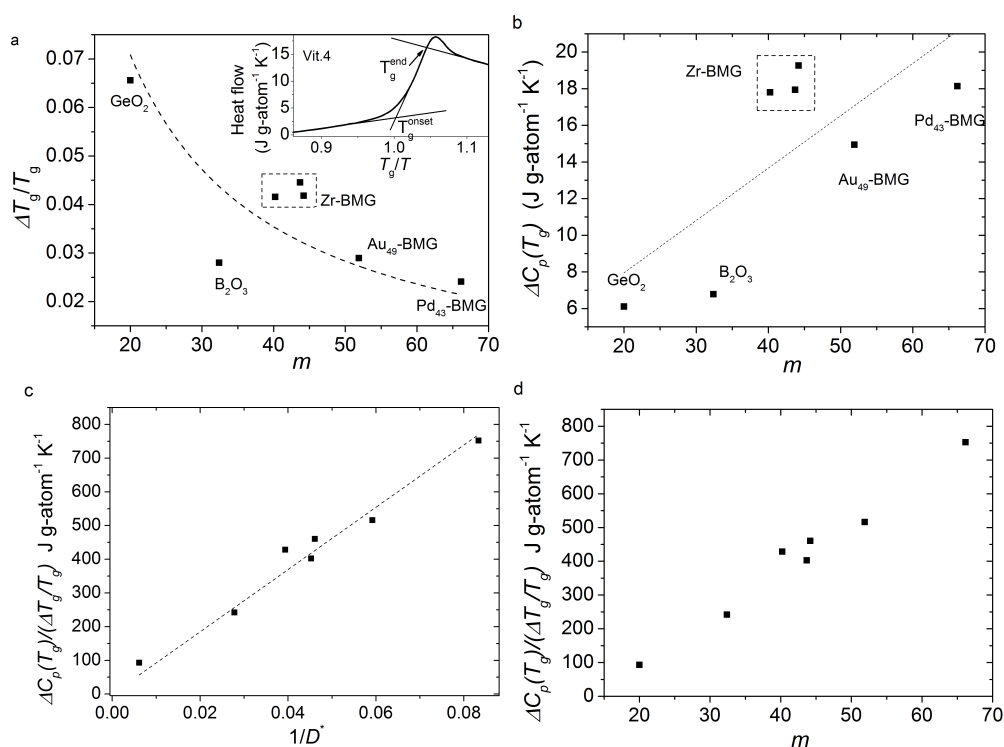


Figure 6.5: (a) $\Delta T_g/T_g$ vs. m . The dashed curve is a fit using Moynihans equation (Eq. 6.6). (b) $\Delta C_p(T_g)$ vs. m . The dashed line is a linear fit. (c, d) The ratio $\Delta C_p(T_g)/(\Delta T_g/T_g)$ vs. fragility $1/D^*$ and vs. m , respectively. The dashed line is a linear fit.

6. Chapter: Determination of fragility from single DSC-scans

Moynihan [129] proposed an alternative correlation between m and the reduced glass transition width, $\Delta T_g/T_g$, assuming that the relaxation time changes by 2.3 orders of magnitude for all glass-formers from the onset of glass transition T_g^{onset} to the end of glass transition, T_g^{end} :

$$\frac{T_g^{end} - T_g^{onset}}{T_g} = \frac{\Delta T_g}{T_g} = \frac{B}{m}, \quad (6.6)$$

where B is a constant. Note that T_g^{end} is originally defined by Moynihan at the temperature where the overshoot of the DSC curve ends. Here T_g^{end} is defined in an alternative way as shown in the inset of Fig. 6.5. In such a way, $\Delta T_g/T_g$ can be related to the average slope of the heat flow, as shown later. The fragilities and $\Delta T_g/T_g$ for the systems investigated in the present work are shown in Fig. 6.5. The dashed curve is the fit by Moynihan's equation (Eq. 6.6), yielding a constant $B = 1.42 \pm 0.13$ with an adjusted $R^2 \approx 0.52576$. Figure 6.5b shows $\Delta C_p(T_g)$ versus m with an adjusted $R^2 \approx 0.45716$ by a linear fit. Both of the correlations displayed in Figs. 6.5a, b are rather qualitative.

Interestingly, we find that the ratio, $\Delta C_p(T_g)/(\Delta T_g/T_g)$, is, however, well correlated with fragility, as shown in Fig. 6.5c. A linear fit by

$$\frac{\Delta C_p(T_g)}{\Delta T_g} \cdot T_g = \frac{a'}{D^*} \quad (6.7)$$

yields the constant $a' = 9239 \pm 287$ J g-atom⁻¹ K⁻¹ with an adjusted $R^2 \approx 0.99327$. The ratio is better correlated with fragility than either $\Delta C_p(T_g)$ or $\Delta T_g/T_g$. In fact, $\Delta C_p(T_g)/(\Delta T_g/T_g)$ is approximately equal to the averaged slope of the heat flow during the glass transition. The correlation displayed in Fig. 6.5c is equivalent to that shown in Fig. 6.3.

The reason for this better correlation is that either $\Delta C_p(T_g)$ or $\Delta T_g/T_g$ only partially reflects the curvature of the $H - T$ curve at T_g ; while the ratio of the two quantities directly describe the curvature (Eq. 6.4), which reflects the rate of the change of the effective free energy barriers in the potential energy landscape. And the the effective free energy barriers are contributed by the enthalpy barriers and configurational entropy, which intrinsically determine the fragility.

6.3 Summary

In summary, the liquid fragility is found to correlate with the T_g -scaled slope of the DSC-scans during the glass transition of the investigated bulk metallic and network oxide glasses. The slope can be expressed as the ratio, $\Delta C_p(T_g)/(\Delta T_g/T_g)$, which reflects the rate of the change of effective free energy barriers in the potential energy landscape during the glass transition. The enthalpy barriers and the

6. Chapter: Determination of fragility from single DSC-scans

number of available transition states (configurational entropy) determine both the effective free energy barriers and fragility, which is the basis of the correlation between $\Delta C_p(T_g)/(\Delta T_g/T_g)$ and fragility. However, either $\Delta C_p(T_g)$ or $\Delta T_g/T_g$ only partially reflects the rate of the change of effective free energy barriers and, therefore, the correlation between either of them and fragility is rather qualitative.

Chapter 7

The liquid-liquid transition in Vit.1

This chapter presents the experimental work in exploring a liquid-liquid transition (LLT) in the bulk metallic glass-forming system $\text{Zr}_{41.2}\text{Ti}_{13.8}\text{Cu}_{12.5}\text{Ni}_{10}\text{Be}_{22.5}$ (Vit.1). This work is motivated by the anomalous viscosity hysteresis observed in the high-temperature viscosity measurement in the melt. The high-temperature specific heat capacity is measured in the equilibrium liquid state. The relation between the thermodynamic and kinetic properties are discussed within the Adam-Gibbs theory. The local structural changes of electrostatically levitated droplets are investigated in real-time using synchrotron X-ray diffraction in containerless environment to access the deeply undercooled liquid region. The temperature dependence of liquid volume is also studied.

The links between the specific heat capacity, structure and viscosity are discussed and a weak first-order liquid-liquid transition is proposed to explain the experimental results. This chapter ends with a discussion about the possibility of the existence of a liquid-liquid transition in other strong bulk metallic glass-forming systems and the challenges for experimental investigations.

This work has been published in the following articles. Figures and texts are reused with copyrights permissions.

- Shuai Wei, Fan Yang, Jozef Bednarcik, Ivan Kaban, Olga Shuleshova, Andreas Meyer and Ralf Busch. Liquid-liquid transition in a strong bulk metallic glass-forming liquid. *Nature Communications*. DOI: 10.1038/ncomms3083 (2013).
- Shuai Wei, Fan Yang, Jozef Bednarcik, Ivan Kaban, Andreas Meyer and Ralf Busch. Polyamorphous Transformation in Bulk Metallic Glass-forming Liquid and its Implication to Strong Liquids. *AIP Conference Proceedings*. 1518, 260 (2013).

7.1 Introduction

There is growing experimental and simulation evidence for the existence of an entropy- (or density-) driven liquid-liquid transition (LLT) between two liquid forms with different structures and properties, for example, in water [67], $\text{Al}_2\text{O}_3\text{-Y}_2\text{O}_3$ [77], SiO_2 [71], BeF_2 [72], metallic glass Ce-Al [11, 78] and even in single-component systems, such as molten phosphorus (P) [79]. However, there has been a long-standing debate regarding the nature of the LLT and even its existence due to the difficulties of experimental observations, as crystallization happens before the access to the desired supercooled regime, or it is located at high temperature and high (or negative) pressure beyond the normal measurement range.

To this end, computer simulations were usually employed to investigate the elusive LLT [71, 70, 72, 11]. In a parallel approach, the lambda (order-disorder) transition phenomena [1] have been studied and compared to the liquid-liquid critical point (LLCP) simulations using Jagla model [92]. It is found that a LLT on a LLCP is reminiscent of a lambda transition characterized by a divergence in the correlation length with a λ -shape heat capacity peak. LLCP is a pressure-temperature combination where the difference between two phases disappears and the phase transition becomes continuous as crossing the point. In an experiment or simulation, measurements are usually carried out in the first-order transition region crossing a phase boundary [77] or in the supercritical region where the lambda transition is smeared out [143]. The underlying LLCP is often located by an extrapolation of the equilibrium phase boundary, known as the coexistence line or tracing back the response function (e.g., specific heat capacity) maximum, the Widom line [122]. One important approach to explore a LLT is to study the specific heat capacity behavior that characterizes the entropy change of the system. The specific heat capacity of supercooled water exhibits a large and increasing value at 240 K and a small value at 150 K between which experimental data are not available due to crystallization [67]. Simulations and experiments [74] on nanoconfined water suggest a lambda-like specific heat capacity peak between the two temperatures that separates a high density liquid near the melting temperature T_m from a low density liquid near its T_g . In analogy to water, specific heat capacity maxima have been also found at high temperature far above the melting point in simulations of the network glass-forming liquids SiO_2 [87, 71] and BeF_2 [72]. More interestingly, the suggested transitions in these systems are found to correlate with anomalous changes in the dynamic properties of liquids, known as a strong-fragile crossover or transition [71, 72, 67, 144, 7, 8]. This is associated with a drastic change in the temperature dependence of relaxation processes (e.g., viscosity) between an Arrhenius-like (strong) and a non-Arrhenius (fragile) behavior. Strong or fragile describes the degree of dynamic fragility, which is a classification scheme for liquids proposed by Angell [6], but its origin has been

a long-standing puzzle. The understanding of the strong-fragile crossover may decipher the origin of the fragility that is of great fundamental and practical importance to glasses and liquids. Recently, a hypothesis has been proposed that the strong liquids differ from fragile liquids by occupying opposite flanks of an underlying lambda transition [1, 7]. It has an important implication that strong liquids are such systems where a LLT can be observed above (not below) its glass transition temperature, T_g , at appropriate pressure, as implied in the studies of water, SiO_2 and BeF_2 .

In contrast to network glass-formers, metallic glass-formers are characterized by non-(or weak) directional bonds in the melt [20]. However, there is direct and indirect evidence of the existence of a strong-fragile crossover [68, 69] in bulk metallic glass (BMG)-forming liquids. This makes them of great interest to be studied to test the hypothesis of underlying lambda transitions that was originally based on simulations and network glass-formers. We choose the BMG-forming system, $\text{Zr}_{41.2}\text{Ti}_{13.8}\text{Cu}_{12.5}\text{Ni}_{10}\text{Be}_{22.5}$ (Vit.1) as a model system for experimental investigations of a possible LLT, because it is a typical strong BMG system and exhibits a change in the viscosity of about two orders of magnitude in the equilibrium melt, which has been attributed to a reversible, temperature induced strong-fragile crossover [68]. In the Vit.1 system, the strong-fragile crossover upon heating takes place above the melting point, which provides a unique opportunity for thermodynamic studies using conventional calorimetric methods.

Thus, we carry out high-temperature calorimetric experiments and observe an anomalous lambda-like specific heat capacity peak in the stable liquid state. Furthermore, we investigate the structural changes corresponding to the thermodynamic and dynamic anomalies with the in-situ synchrotron X-ray scattering experiments in contactless environment using an electrostatic levitation (ESL) [104]. We show thermodynamic and structural evidence that is consistent with the observations in viscosity, suggesting that there is a LLT from one liquid phase to another with different entropy, local structure and fragility in the Vit.1 system.

7.2 Specific heat capacity maxima of the liquid

Figure 7.1, 7.2 shows the specific heat capacity (c_p) of Vit.1. A specific heat capacity peak is observed on heating between around 1100 and 1200 K, above the reported liquidus temperature 1026 K. The area of the c_p peak is proportional to the heat gain, which is determined to be $\Delta H_{LL} = 1.0 \pm 0.1$ kJ g-atom⁻¹, about 10% of the enthalpy of fusion ($\Delta H_f = 9.7 \pm 0.7$ kJ g-atom⁻¹). The inset shows the zoom-in of the peak (solid circles) and a separate scan (open squares), in which the main peak is reproduced (1100-1200 K). We notice that a small subpeak on the left shoulder of the broad peak is also reproducible. By lowering

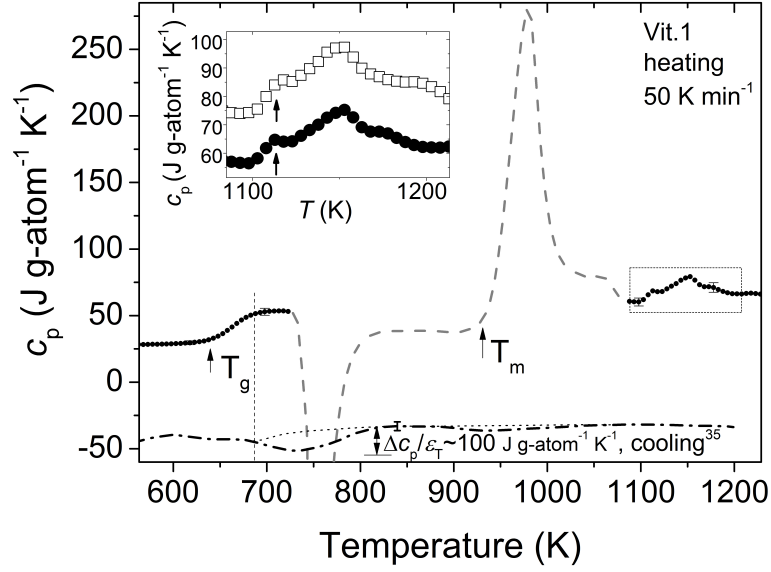


Figure 7.1: Specific heat capacity, c_p , of Vit.1. c_p of an amorphous sample is measured upon heating at 50 K min^{-1} in reference with sapphire. The solid circles represent the glassy, supercooled liquid and stable liquid states; the dashed curve indicates the crystallization and melting processes. Note that there is a specific heat capacity peak at around 1100-1200 K, which occurs in the molten liquid according to the in-situ XRD taken at a 10 times higher heating rate ($\sim 9 \text{ K s}^{-1}$) (see Fig. 7.3). Inset shows the magnification of the c_p peak (1100-1200 K), where the solid circles and open squares represent two separate measurements (vertically shifted for clarity). The arrows indicate that there is a small subpeak on the left shoulder of the main peak. In the lower part of the figure, the dash-dot curve shows the specific heat capacity during cooling of Vit.1 taken from c_p/ε_T in Ohsaka et al. [145] (assuming the emissivity [145] $\varepsilon_T = 0.18$), which is here plotted as negative values to indicate the exothermic event around 700-800 K in the supercooled liquid region in reference to the baseline (dotted curve) (see Section 7.8) (taken from ref. [2]).

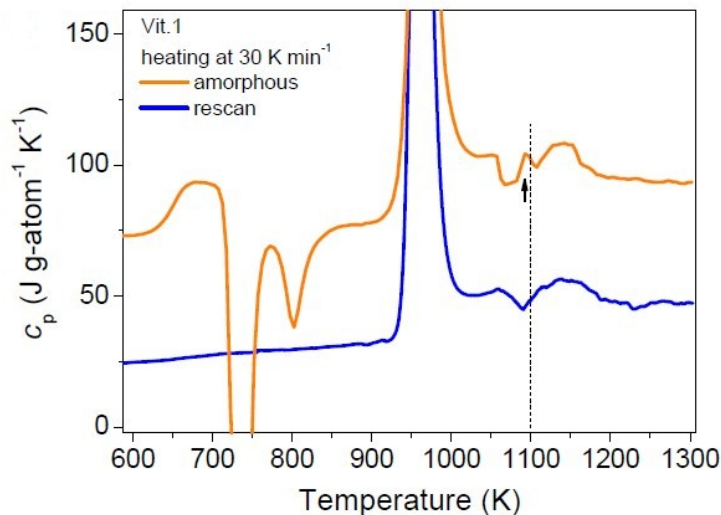


Figure 7.2: Specific heat capacity c_p of Vit.1 measured upon heating at 30 K min^{-1} for the amorphous sample (upper) and once-melted crystallized sample (lower) (vertically shifted for clarity). The arrow shows the small subpeak separated from the main peak to a lower temperature (taken from ref. [2]).

the heating rate down to 30 K min^{-1} , this small subpeak can be separated to a lower temperature $<1100 \text{ K}$ from the main broad peak (see the upper curve in Fig. 7.2). And during a rescan of the once-melted crystallized sample, the subpeak disappears while the main peak remains (lower curve in Fig. 7.2). This observation suggests that this small subpeak probably comes from a small portion of remaining crystalline phases. The first scan apparently reduces the inhomogeneity and thus diminishes the small subpeak and ruggedness of the measured specific heat capacity curve. However, we show in the next section that the broad main peak cannot be explained by melting of crystals and should be regarded as a consequence of an intrinsic change in the liquid.

7.3 Monitoring the melting process using in-situ synchrotron X-ray diffraction

Although the liquidus temperature was determined [146] to be 1026 K using calorimetry, it needs to be investigated here whether the c_p peak ($1100\text{-}1200 \text{ K}$) upon heating occurs in the stable liquid state or is due to melting of some remaining crystalline phases. We perform in-situ X-ray diffraction (XRD) experiment on levitated Vit.1 droplets. The XRD patterns of Vit.1 recorded upon continu-

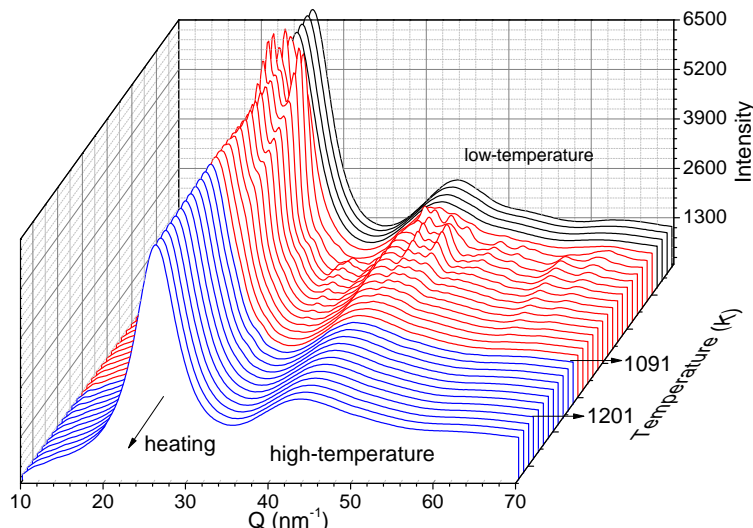


Figure 7.3: In-situ synchrotron X-ray diffraction integral patterns of Vit.1 upon heating. As the temperature increases, the amorphous sample crystallizes and the Bragg peaks become pronounced. When the melting sets in, these sharp peaks become smaller and disappear. The blue colour highlights the patterns corresponding to the temperature range, where the c_p peak is observed (1100-1200 K) (taken from ref. [2]).

ous heating at a rate of about 9 K s^{-1} are shown in Fig. 7.3. It is seen that the sharp Bragg peaks first appear due to the partial crystallization of the amorphous sample and then disappear during melting. As the temperature increases up to around 1091 K, the sharp peaks disappear in both the 1st and 2nd maxima of diffraction curves, indicating that the crystals are molten. This corresponds to the pronounced endothermic melting peak observed between 939 and 1080 K on the c_p curve in Fig. 7.1. It is possible that there still remains a small portion of crystalline particles that melt above 1100 K. However, for the broad c_p peak in the temperature range $\sim 1100 - 1200 \text{ K}$, if it was due to melting of remaining crystals, the crystalline volume fraction would be around 10% of the liquid according to the ratio of the enthalpy change by this c_p peak to the heat of fusion ($\Delta H_{LL}/\Delta H_f \approx 10\%$). This amount of crystals would be well within the detection limit and should be clearly seen as pronounced sharp Bragg peaks in XRD patterns over the entire range of the c_p peak. In contrast, according to the integral diffraction patterns between 1091 and 1200 K in Fig. 7.3, it is unlikely that there (1100-1200 K) still remained 10% crystals of the system. If the crystals would be very small, such as nano-crystalline particles, there is a possibility that only broad maxima rather than sharp Bragg peaks appear in the diffraction patterns. However, our volume measurements show no indication of the presence

of a nano-crystalline or crystalline phase (see Section 7.8).

The c_p peak is observed in the same temperature range (1100-1200 K), where the viscosity drops anomalously by approximately two orders of magnitude [68]. During the drastic viscosity change, there is a large change in the temperature dependence of viscosity, which can be described by the Vogel-Fulcher-Tammann equation [35, 36] $\eta = \eta_0 \exp[D^*T_0/(T - T_0)]$, where η is viscosity and η_0 is constant [3]. The fitting parameter D^* characterizes the fragility of the liquid, which changes significantly from $D^* = 26.5$ below 1100 K to $D^* = 12$ above 1200 K in the present liquid [68]. This indicates a crossover of dynamics from the strong to fragile liquid (see Fig. 7.4). It appears that the specific heat capacity peak is associated with this crossover of liquid dynamics, which, by a semi-quantitative estimation, also leaves out the alternative explanation of a viscosity hysteresis based on crystalline particles. If we assume that there were remaining about 10% crystals melted throughout the c_p peak, the crystalline particles in the liquid can be modeled as concentrated suspensions of solid spheres. According to the models [147, 148] for the viscosity behavior of suspensions of solid spheres based on extensive experimental data, for the melting of 10% crystals, the viscosity change of the entire system would be around 150% (see Fig. 1 of Thomas [147] and Fig. 4 of Frankel and Acrivos [148]), which cannot explain the measured change in viscosity of approximately two orders of magnitude, that is, 10,000% in the present system.

7.4 The relation between specific heat capacity and viscosity

The Adam-Gibbs theory [49] provides a link between the kinetics and thermodynamics of a liquid. Thus, viscosity can be calculated given the configurational entropy using

$$\eta = \eta_0 \exp\left(\frac{C}{S_c \cdot T}\right), \quad (7.1)$$

where the C is a constant, containing an enthalpy barrier per particle for cooperative rearrangements. The pre-exponential factor, $\eta_0 = 4 \cdot 10^{-5}$ Pa·s, is the viscosity of liquids at infinite high temperature [149].

A drastic change of viscosity is correlated to a large change in the configurational entropy, which would be reflected by a specific heat capacity maximum. To simulate the specific heat capacity shape during heating and cooling, we use a simple model, where the specific heat capacity of the liquid is approximated using the equation of Kubaschewski et al. [150]

7. Chapter: The liquid-liquid transition in Vit.1

$$c_p = 3R + b \cdot T + c \cdot T^{-2}, \quad (7.2)$$

with the experimental data fitted parameters $b = 7.5 \cdot 10^{-3}$, $c = 8.17 \cdot 10^6$ from ref. [15]. Moreover, in the temperature range where the drastic viscosity changes take place, the specific heat capacity maximum shape is simplified as a right triangle (see Fig. 7.5), because it is close to the shape of a lambda (λ) peak that is assumed to be the specific heat capacity shape of a liquid-liquid transition. Figure 7.5 shows the simulated specific heat capacity upon heating (solid line) with an endothermic peak 1100-1200 K and during cooling (dashed line) with an exothermic peak 840-940 K. With this simulated specific heat capacity, if we assume that the vibrational specific heat capacity is a constant $25 \text{ J g-atom}^{-1} \text{ K}^{-1}$ (Dulong-Petit law) for simplicity, one can calculate the configurational entropy using

$$S_c = S_0 + \int_{T_g}^T \frac{\Delta c_p^{liq-vib}(T')}{T'} dT'. \quad (7.3)$$

Inserting S_c into Eq. 7.1, the viscosity can be calculated. To obtain a good match between the calculated and measured viscosity, one can adjust the three parameters simultaneously, the height of the c_p peaks, the constants S_0 and C .

The calculated viscosity is shown in Fig. 7.4. The solid curve on heating and the dashed curve during cooling reproduces approximately the experimental data of the viscosity hysteresis, with the parameters of the height of the c_p peaks, 250 and -220 $\text{J g-atom}^{-1} \text{ K}^{-1}$ for heating and cooling respectively; $S_0 = 15 \text{ J g-atom}^{-1} \text{ K}^{-1}$, and $C = 352 \text{ kJ g-atom}^{-1}$. Shown in Fig. 7.5 is the corresponding specific heat capacity with pronounced peaks and the calculated configurational entropy (Inset of Fig. 7.5) on heating and cooling. On this account, the specific heat capacity peaks in Fig. 7.5 would be expected for the strong-fragile crossover according to the Adam-Gibbs theory.

However, the question is if such pronounced specific heat capacity peaks are realistic and how the theory matches experimental results. There have been reports [145] of an exothermic event around 700-800 K by studying the temperature-time profile of the Vit.1 liquid during undercooling from above 1200 K in an electrostatic levitator (ESL) (also shown in the lower part of Fig. 7.1). This exothermic event corresponds to a specific heat capacity maximum which is qualitatively consistent with the calculated specific heat capacity peak from the Adam-Gibbs theory, although it was previously interpreted as a result of a possible chemical decomposition. Ohsaka et al. [145] estimated the heat release during the exothermic event to be around 900 J mol^{-1} , which corresponds to a much weaker specific heat capacity peak and locates at a lower temperature by $\sim 100 \text{ K}$ than the simulated peak (dashed line in Fig. 7.5). The temperature difference between the

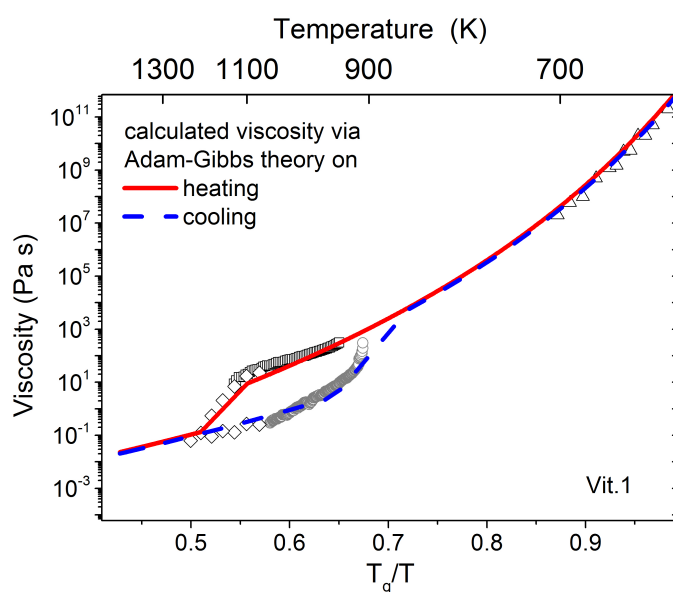


Figure 7.4: Calculated viscosity (solid and dashed line) is compared with the measured viscosity data points (taken from ref. [68]) of Vit.1. The data points are plotted against T_g/T for combined isothermal (\diamond) and viscosity measured on cooling at 2 K s^{-1} from 1125 K (\square) and 1225 K (\circ). Triangles (\triangle) represent viscosity near T_g measured by three-point-beam bending. A viscosity hysteresis path was observed upon heating and cooling. Note that there is a strong-to-fragile crossover on heating between 1100 K and 1200 K, whereas fragile-to-strong crossover during undercooling around 900 K for a cooling rate of 2 K s^{-1} (taken from ref. [151]).

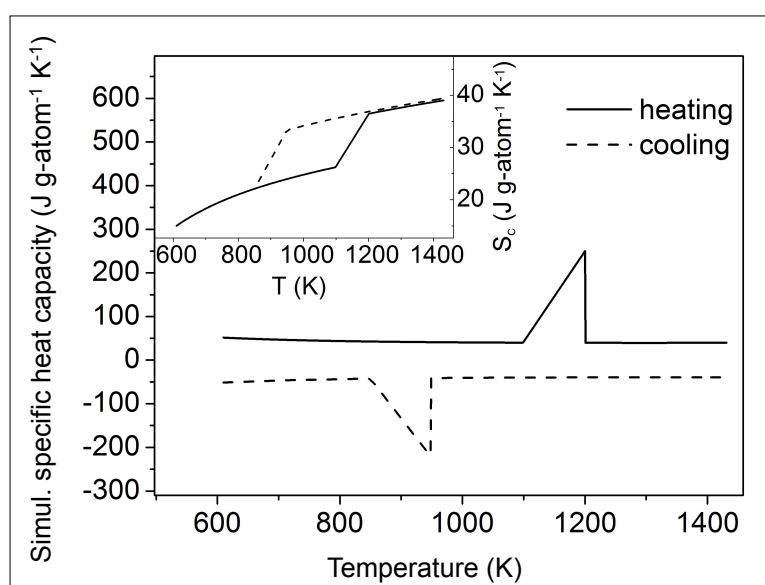


Figure 7.5: Simulated liquid specific heat capacity with the peaks on heating (solid line) and on cooling (dash line, shown in negative values to indicate the exothermic character) using the Adam-Gibbs theory and the viscosity data in Fig. 7.4. The peaks corresponding to the abrupt viscosity changes are simplified as a positive right triangle (heat gain) and a negative right triangle (heat release). The Inset shows the calculated configurational entropy S_c (taken from ref. [151]).

measured and simulated peaks could be due to the much faster cooling rate ($\sim 17 \text{ K s}^{-1}$) in the undercooling experiment with ESL than that in viscometer ($\sim 2 \text{ K s}^{-1}$). However, the much weaker peak measured ($\sim 900 \text{ J g-atom}^{-1}$) than simulated ($11 \text{ kJ g-atom}^{-1}$) shows that the Adam-Gibbs theory, under the assumption of an unchanged parameter C , only works qualitatively rather than quantitatively during the liquid-liquid transition. This shows that the Adam-Gibbs theory is invalid at a transition point because the entropy is discontinuous during a first-order transition. Consequently, the specific heat capacity peak on heating would be also much weaker than the simulated and correspond to an enthalpy change in the same order of magnitude as that on cooling ($900 \text{ J g-atom}^{-1}$), which is the value that is measured, shown in Fig. 7.1, 7.2.

7.5 Investigation of the local structure using synchrotron radiation

Besides monitoring the melting in the vicinity of liquidus temperature, in-situ synchrotron XRD combined with ESL enable us to study the structural changes with temperature (700-1300 K) during continuous cooling and reheating of the sample as well as at different constant temperatures. One particular advantage of ESL is the ability to access the deeply undercooled regime due to the absence of heterogeneous nucleation sites e.g., container walls. Thus, it allows us to explore a possible structural transition in the undercooled state which is usually hidden by crystallization and difficult to detect with conventional methods [104].

Electrostatically levitated droplets are cooled from above 1300 K down to below 700 K. The XRD patterns are recorded and the total structure factor $S(Q)$ is extracted from the diffraction intensity data. An example of a dataset of $S(Q)$ on cooling is shown in Fig. 7.6. The first peak position of the structure factors, Q_1 , is obtained by cubic spline interpolations, which is found to be the most reliable method to determine the peak position in the present multicomponent system. In Fig. 7.8, the 3^{rd} power of the inverse of Q_1 [$1/Q_1^3$ in the volume dimension (\AA^3)] on cooling is plotted as open symbols (diamonds and squares) against temperature. As expected, Q_1 shifts to higher momentum transfers Q with decreasing temperature. However, it is clearly observed that a sudden change in the temperature dependence of $1/Q_1^3$ occurs around 830 K (arrow in Fig. 7.8). During undercooling, the data (open diamonds and squares) deviate from its original high- Q_1 state (lower line) and shift suddenly (see arrow) to a low- Q_1 state (upper line) between around 830 K and 760 K. With further decreasing temperature, the data retain their low- Q_1 state. For Vit.1, there are 15 different pairs of partial structure factors, which contribute to the measured total structure factor $S(Q)$, weighted by their corresponding X-ray scattering cross sections. However, Zr has

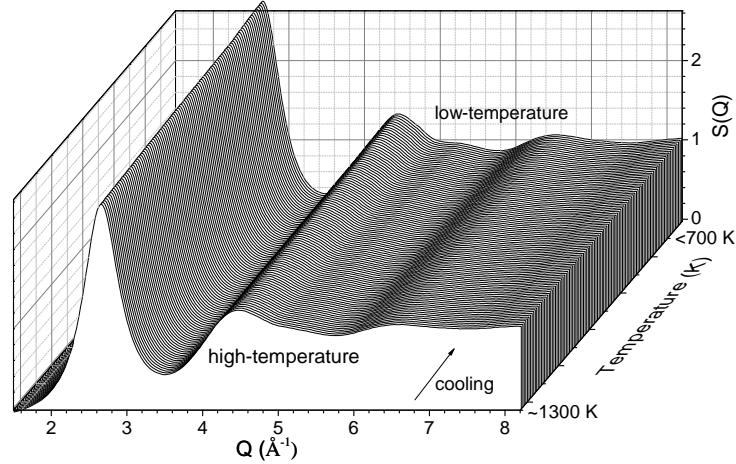


Figure 7.6: The complete data set of structure factor $S(Q)$ during cooling from ~ 1300 K down to < 600 K (upper: low temperatures; lower: high temperatures). These XRD integral patterns show the perfect liquid or amorphous feature and no Bragg peak is present, indicating clearly that there is no crystallization during cooling. Thus, the sudden change observed in Q_1 and FWHM (Fig. 7.8, 7.9 in the main text) cannot be attributed to the crystallization process (taken from ref. [2]).

the highest concentration and the largest atomic number. Therefore, the Zr-X (X=Zr, Cu, Ti, Ni) spatial correlations dominate the contribution to the first peak of $S(Q)$. The discontinuity in $1/Q_1^3$ observed in Fig. 7.8 suggests an abrupt change in the Zr-dominant inter-atomic correlations in real space. Note that T_g of Vit.1 is located at a much lower temperature [15] (< 700 K taken the rate effect into account [15]). Therefore, the discontinuity observed at around 830 K cannot be attributed to approaching the glass transition.

The X-ray diffractogram is recorded further upon reheating of the sample (see structure factors in Fig. 7.7). The solid circle symbols from 700 K to 780 K and from 1105 K to 1350 K in Fig. 7.8 represent $1/Q_1^3$ on reheating. The values of $1/Q_1^3$ upon reheating reproduce the values during cooling for each respective temperature range, except for the range from 780 to 1105 K. In this temperature interval 780-1105 K, the sample (re-)crystallizes from the undercooled liquid, and measurements on a liquid sample are not possible. The crystallization upon reheating beginning at 780 K is expected if the (re-)heating rate of the undercooled liquid is not fast enough to avoid the crystallization altogether (< 200 K s^{-1}), according to the time-temperature-transformation diagram of Schroers et al. [34]. It should be pointed out that a discontinuity in $1/Q_1^3$ upon reheating is not obvious in the temperature range, where the c_p peak is observed around 1100-1200

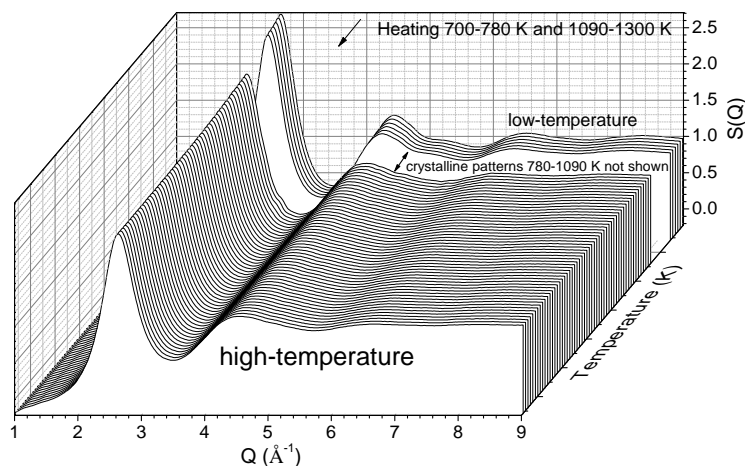


Figure 7.7: Total structure factor $S(Q)$ upon reheating the liquid Vit.1. Note that only the XRD patterns for the liquid states are shown here. There is a gap in the temperature range 780-1090 K where the amorphous sample crystallizes on reheating and the measurement on the liquid state is not possible (taken from ref. [2]).

K, from the limited data points collected, due to the narrow time-window of the detection. Nevertheless, it appears that once the sample is molten at 1105 K, it recovers its high- Q_1 state (lower line), distinct from its low- Q_1 state (upper line).

Figure 7.9 shows the full width at half maximum (FWHM) of the first peak of $S(Q)$ as a function of temperature during cooling and reheating. It is clearly observed that an abrupt change of the FWHM during cooling (open symbols) around 760-830 K, below which the data shift to a distinct upper track while returned to the decreasing trend. This is the exactly same feature as the sudden change observed in $1/Q_1^3$ in Fig. 7.8). Furthermore, on reheating, the data points (solid cycles) trace back the cooling data in the temperature range of ~ 700 -760 K. As expected, a data gap is left due to interference of crystallization and re-melting on reheating. After the system returns to the liquid state at high temperature (~ 1100 K), the data points exhibit a clear change of slope at around ~ 1150 K, which corresponds to the temperature range where the c_p peak is observed in the calorimeter (Fig. 7.1). It is striking that the changes on cooling and reheating appear as a reversible phenomenon and the data in Fig. 7.9 display a form of three quarters of a hysteresis when the missing data gap is extrapolated as the dashed line from the lower temperature data. Apparently, FWHM is a parameter for characterizing the diffraction peak shape and shows a lower degree of scatter of data points than Q_1 because for determining Q_1 the error may rise by the cubic

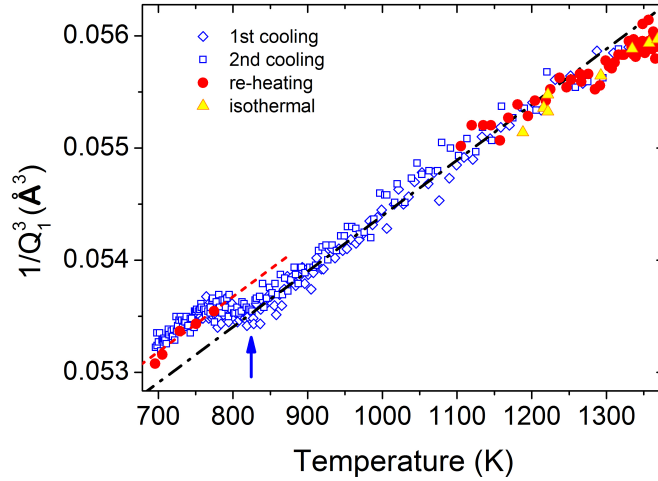


Figure 7.8: Temperature dependence of $1/Q_1^3$ (\AA^3) on cooling (open symbols) and on heating (solid symbols). Filled triangles are isothermal measurements during stepwise-heating. The arrow points at a clear discontinuity of $1/Q_1^3$ upon cooling at around 830 K. The lower and upper lines are the data fittings with Yavari's equation (see text) for two liquid states (taken from ref. [2]).

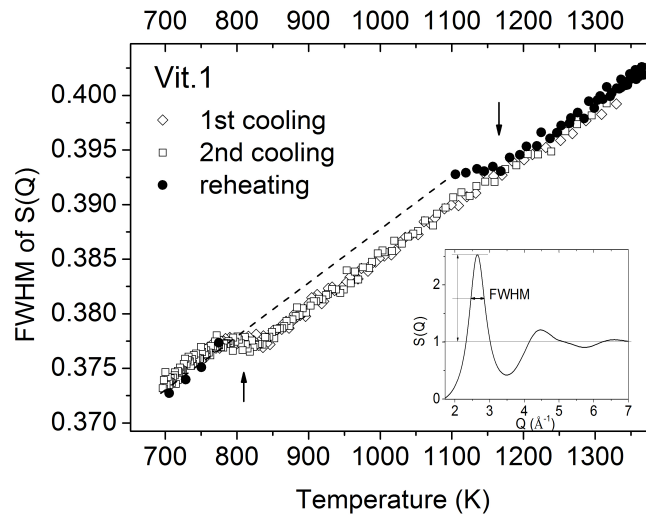


Figure 7.9: The full width at half maximum (FWHM) of the 1st peak of $S(Q)$ (see Inset) obtained by fitting the peak with the Gaussian function as a function of temperature. The arrows point at the clear slope changes in the temperature range 760-830 K during cooling and 1100-1200 K upon reheating. The dashed line is the assumed heating data trace if crystallization could be avoided on reheating (taken from ref. [2]).

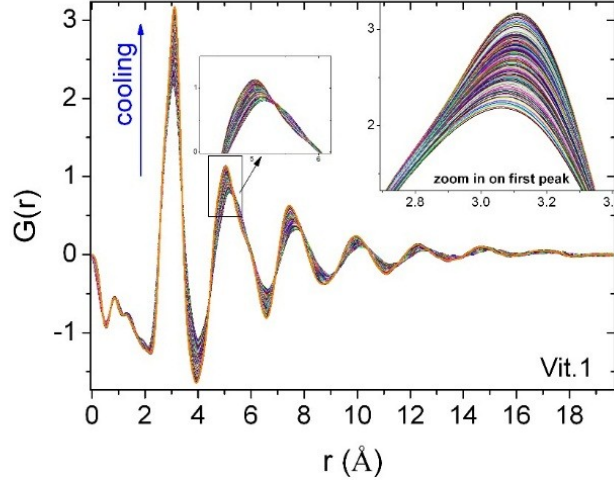


Figure 7.10: Reduced pair distribution function $G(r)$ of Vit.1 during cooling from 1300 K to 700 K by Fourier transformation from $S(Q)$ in Fig. 7.6. Inset (right): zoom-in on the first peak.

spline analysis procedure. The FWHM provides a more accurate characterization of the local structural changes and thus allows us to see the sudden change at high temperature (1150 K) as expected from c_p and the viscosity measurements.

7.6 Real space analysis with pair distribution functions

To obtain real space structural information, the reduced total pair distribution functions $G(r)$ are calculated from the structural factor $S(Q)$ by Fourier transform according to the equation [100]

$$G(r) = \frac{2}{\pi} \int_0^{\infty} Q[S(Q) - 1] \sin(Qr) dQ. \quad (7.4)$$

$G(r)$ provides the information about the probability of finding two atoms separated by a certain distance r . This allows us to study the relative positions of the atoms in the system and offers important structural information.

Figure 7.10 and 7.11 show the reduced pair distribution function, $G(r)$, during cooling and heating, respectively. The peaks of $G(r)$ give the structural information about the respective coordination shells. The first peak is located at around 3.1 Å, which corresponds to the nearest neighbor distance between two atoms. This distance is likely the Zr-Zr atoms distance because the radius of Zr atom is

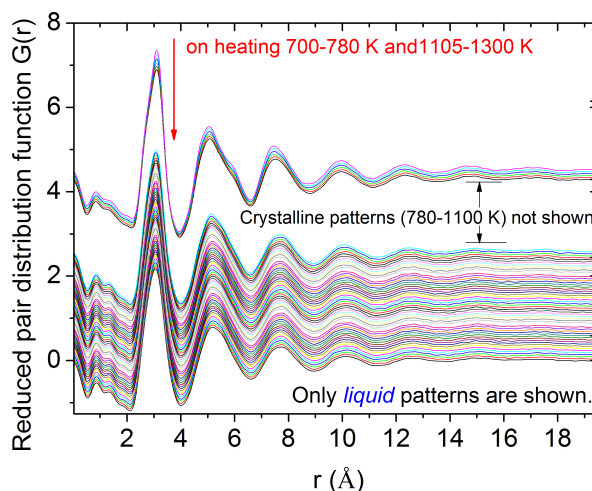


Figure 7.11: Reduced pair distribution function $G(r)$ of Vit.1 for reheating (vertical shifted for clarity) by Fourier transformation from $S(Q)$ in Fig. 7.7.

1.55 Å and the separation of two Zr atoms is 3.1 Å that is consistent with the first peak position of $G(r)$. The 2nd, 3rd and 4th peak positions reveal the distance of the 2nd, 3rd and 4th coordination shells, respectively.

As shown in Fig. 7.12, the 1st, 2nd, 3rd and 4th coordination shell radii behave differently on their respective length scales with varying temperature, as shown in Fig. 7.12 (a), (b), (c) and (d), respectively. The 1st coordination shell radius r_1 increases anomalously with decreasing temperature. r_1 displays an opposite behavior to r_2 , r_3 and r_4 which decrease with lowering temperature. Additionally, r_1 , r_2 and r_3 do not show a sudden change around 800 K in contrast to what is observed in Q_1 of $S(Q)$ in Fig. 7.8. For the 4th and larger coordination shells r_n (for $n \geq 4$) include too much noise to provide conclusive structural information due to statistic errors and the termination errors during the Fourier transformation from the $S(Q)$ to the $G(r)$. Therefore, the length scale of the structural transformation in the undercooled state is likely no less than the 4th shell distance (~ 1 nm). This suggests that the structural changes observed on the first peak of $S(Q)$ in the reciprocal space have occurred on the medium-range order length scale ≥ 1 nm. The fact that the first peak of $S(Q)$ gives mainly the information about the medium-range order structural correlation has been demonstrated in the literature, for instance, by Bednarcik et al. [152].

There is a noticeable slope change in trace of $r_3(T)$ on reheating between 1100 and 1200 K, which is the similar temperature range where the anomalies in specific heat capacity, viscosity and FWHM are observed, although the data points are scattered to some extent. However, no reversible phenomenon of this

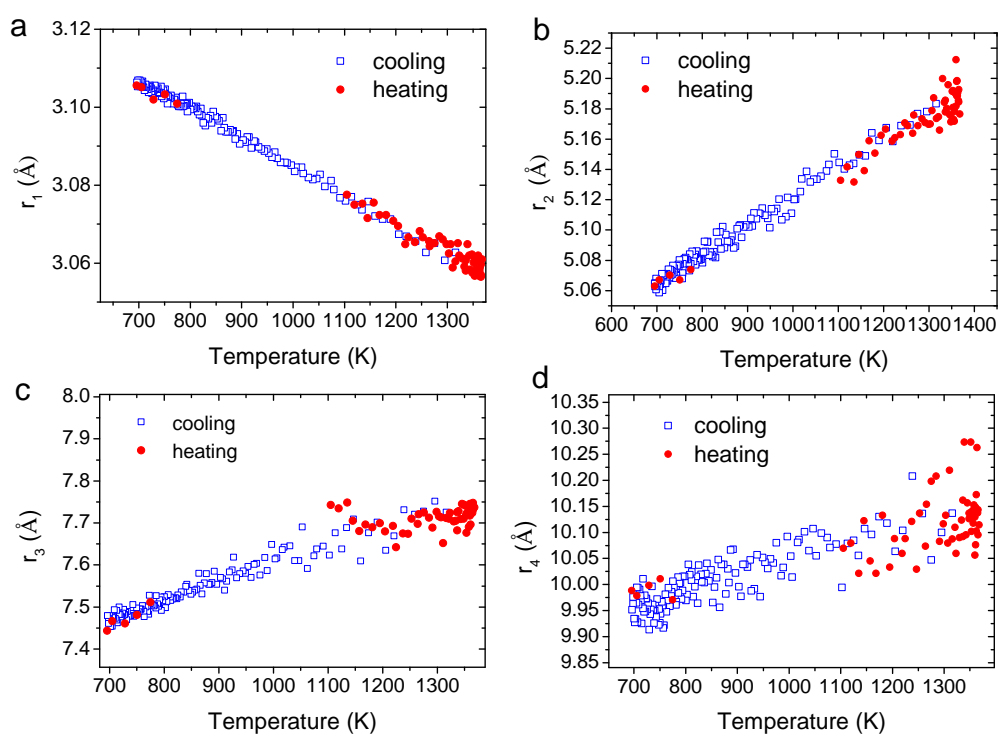


Figure 7.12: The 1st (a), 2nd (b), 3rd (c), and 4th (d) peak positions of $G(r)$ during cooling (open symbols) and reheating (solid symbols) for the liquid state.

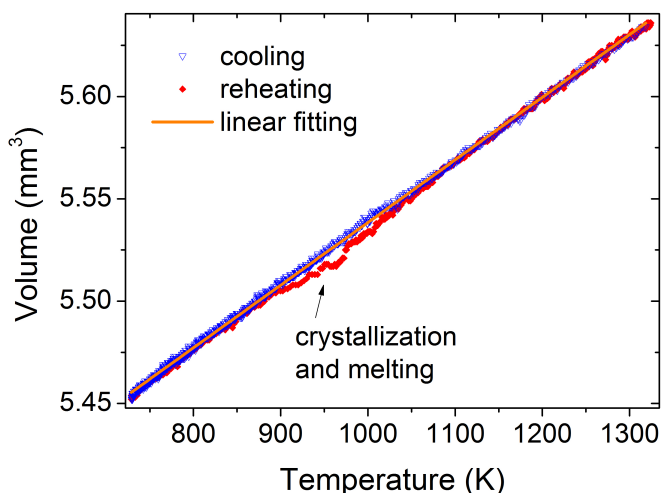


Figure 7.13: Macroscopic liquid volume measured in ESL during cooling and reheating. The deviation of the macroscopic volume (density) data on reheating (arrow) from the data on cooling is due to the process of partial crystallization and re-melting around 800-1100 K, which is the temperature range where the XRD data for the liquid state are not available on reheating, seen as a data-gap between the solid circles in Fig. 7.8 and 7.9 (taken from ref. [2]).

slope change on r_3 is observed during cooling at around 800 K, suggesting that this structural change on r_3 is not reversible with respect to temperature.

7.7 Liquid volume

Figure 7.13 shows the macroscopic volume of Vit.1 during cooling and reheating. We find that the transition in structure on the atomic scale is not reflected in the macroscopic liquid volume (or density) measured in the ESL. The volume data appear as a continuous function of temperature and no anomaly is observed in the temperature range 760-830 K during cooling (blue triangles) or 1105-1200 K on heating (red diamond). This phenomenon can be understood by considering that liquids are distinct from amorphous solids by the fact that liquids are not rigid and the atomic structure of a liquid behave differently on different length scales. The increase of the local volume observed on one length scale can be accompanied by a decrease on the other length scale, which, however, may be out of our observation window. Thus, the local volume change does not necessarily result in an overall liquid volume (density) change which averages over a macroscopic volume ($\sim 5 \text{ mm}^3$).

One must emphasize that the deviation of the volume data on heating (see arrow) is due to partial crystallization, as demonstrated by the XRD results in

Fig. 7.3. The volume hysteresis is irrelevant to the LLT, although it has been previously confused [153] with a strong-fragile hysteresis. By a linear fitting, the volume measurement reveals a constant volume thermal expansion coefficient $\alpha_{mac} = 5.56 \cdot 10^{-5} \text{ K}^{-1}$, which is remarkably smaller than $\alpha_{XRD} = 9.2 \cdot 10^{-5} \text{ K}^{-1}$ on the microscopic scale obtained from the XRD measurement when applying Yavari's equation [154].

According to the hypothesis of Yavari et al., Q_1 is associated with the change of mean atomic volume V and the temperature dependence of $Q_1(T)$ could be described by:

$$\left(\frac{Q_1(T_0)}{Q_1(T)}\right)^3 = \frac{V(T)}{V(T_0)} = 1 + \alpha_{XRD} \cdot (T - T_0), \quad (7.5)$$

where α_{XRD} is the volume thermal expansion coefficient as determined by X-ray diffraction. The best fit of the data (Fig. 7.13) in the temperature range 850-1300 K is given by $\alpha_{XRD} \approx 9.2 \cdot 10^{-5} \text{ K}^{-1}$.

In light of their result for the amorphous state, the thermal expansion coefficient obtained from the XRD is the same as that measured in a dilatometer. However, for the liquid state of Vit.1, the thermal expansion coefficient from the XRD is different from that determined from a macroscopic volume measurement. This difference is expected for the supercooled and stable liquid states ($T > T_g$), because the Yavari's approach is based on the underlying assumption that the structural change at $T < T_g$ is negligible, which is no longer valid in the cases of the liquid state ($T > T_g$), as discussed in ref. [155]. In liquids, the thermal expansion coefficient is varying on different length scales.

7.8 First-order liquid-liquid transition by nucleation and growth

The c_p peak shown in Fig. 7.1 is measured upon heating using a calorimeter. It should be noted that the c_p measurement of deeply supercooled liquid is not possible in the calorimeter, because the crucible walls act as potent heterogeneous nucleation sites for the liquid. Thus, containerless techniques such as electrostatic levitation are necessary to access the deep supercooled region. The dash-dot line in the lower part of Fig. 7.1 is the deep supercooled c_p data from c_p /emissivity extracted from a temperature-time profile measured in an ESL by Ohsaka et al. [145]. An exothermic peak is reported around 700-800 K corresponding to an enthalpy release of about $900 \text{ J g-atom}^{-1}$ estimated by the authors, which, by the following analysis alternative to the authors', should be associated with the c_p peak on heating (1100-1200 K) when taking the viscosity hysteresis and structural

7. Chapter: The liquid-liquid transition in Vit.1

measurements into account. Both c_p peaks correspond to a similar enthalpy change (~ 1 kJ g-atom⁻¹) and form a hysteresis with respect to temperature, which is comparable to the viscosity hysteresis that characterizes the strong-fragile crossover [68]. The correlation between thermodynamics and kinetics is suggested by Adam-Gibbs theory [49], at least, qualitatively. This hysteresis is consistent with the hysteresis-like behavior in $1/Q_1^3$ and FWHM of the structure factor $S(Q)$ (Fig. 7.8 7.9) where two different local structures correspond to the different properties. These findings suggest that there exists a reversible LLT between two liquid phases with different entropies, liquid dynamic fragilities and local structures in the investigated system.

Alternative explanations to the LLT could be crystallization or chemical decomposition (phase separation) for the anomalies in the supercooled multicomponent liquid Vit.1. If we assume the sudden changes in $S(Q)$ (Fig. 7.8, 7.9) during cooling are due to crystallization, we should be able to see Bragg peaks in the XRD patterns. However, the complete XRD data set during cooling from ~ 1300 K show no crystalline reflexes during the entire cooling process, indicating that no crystallization has occurred. Furthermore, the Bragg diffraction peaks would keep increasing as the crystals grow. However, the sudden changes observed in $S(Q)$ take place only in a certain temperature range 760-830 K and clearly ends at around 760 K. This is very different behavior from crystallization. It could be also assumed that the anomalies are due to the respective formation and melting of nano-crystals, which are so small that they do not raise sharp Bragg diffraction peaks but only broad diffuse maxima in the scattering patterns. In such a case, it is not clear how the drastic viscosity change in the liquid could be caused by such a small portion of nano-crystals. Moreover, according to literature values [145], the volume change for the transformation from the liquid to the crystalline state of Vit.1 can be calculated to be 1.29% at ~ 800 K and 1.82% at ~ 1150 K by linear extrapolation. From the rule of mixing, $\rho_{mix} = \rho_{liq}(1-x) + \rho_{cry}x$ where ρ is density and x is (nano-) crystalline volume fraction, one can derive the equation for volume change $(V_{liq} - V_{mix})/V_{liq} = 1 - 1/\{1 + x[(V_{liq} - V_{cry})/V_{cry}]\}$. The values of the ratio $V_{liq}/V_{cry} = \rho_{cry}/\rho_{liq}$ can be obtained from Ohsaka et al.[145], and the density of nano-crystals is approximated to that of crystals. Consequently, the system volume changes by 10% nanocrystalline volume fraction, estimated by the c_p peaks area ratio, would be around 0.13% at 800 K and 0.19% at 1150 K, which would correspond to the values of changes in Fig. 7.13, approximately 0.007 and 0.010 mm³, respectively. However, no such change is observed around these temperatures (Fig. 7.13), which is contrary to the nano-crystal or crystal scenario.

Phase separation is a common phenomenon in multicomponent systems, during which the system decomposes into two (or more) immiscible phases with different compositions, which is in contrast to a LLT where one liquid phase

7. Chapter: The liquid-liquid transition in Vit.1

transforms into another completely. Vit.1 has been extensively studied near T_g by Löffler et al. [156] and Schneider et al. [87] using small-angle neutron scattering (SANS). They reported interference maxima in the scattering intensity, giving evidence for spinodal decomposition on the nanometre scale in the amorphous phase upon annealing near T_g , which is followed by nanocrystallization. These results have been later challenged by Hono and coworkers [157] by showing that no evidence for decomposition before crystallization of an icosahedral phase was observed using transmission electron microscopy, small-angle X-ray scattering and high-resolution three dimensional atom probe. Interpretations of these results appear controversial. For the case reported by Hono and coworkers, crystallization seeded from a single amorphous phase rather than immiscible separated phases, indicating that no decomposition occurs in the supercooled liquid. For the case reported by Löffler et al. and Schneider et al., we note that the intensity maximum in SANS occurred from room temperature up to a critical temperature $T_c \sim 670$ K, above which no maximum was observed. In addition, the reported decomposition triggered nanocrystallization after an incubation time, which was a decreasing function with increasing temperatures (2.8 s at 661 K) according to Löffler and Johnson's model [158]. In contrast, the sudden change in $S(Q)$ observed in the present study, as well as the exothermic c_p peak reported by Ohsaka et al. [145], is well above the critical temperature for decomposition, and no crystallization is detected by in situ XRD. Therefore, the LLT suggested in this work is not related to the decomposition, which might occur at lower temperatures near T_g as suggested in Löffler et al. [156] and Schneider et al. [87]. If we assume a scenario including a phase separation, one would expect the presence of two glass transitions corresponding to two separated phases; however, no such indication has been observed in the present calorimetric measurements or reported studies to the best of our knowledge.

What's more, the fragility of the Zr-based bulk metallic glass-forming liquids is shown to be not sensitive to a compositional change [69]. For five different compositions of Zr-based glass-forming alloys, the VFT parameter D^* is all around 20 near T_g at low temperature, while D^* is all about 10 in the equilibrium melt far above the melting point [69]. This suggests that the fragility change of Vit.1 between $D^* = 26$ and $D^* = 12$ is unlikely due to a compositional change resulted from a chemical decomposition.

At last, we emphasize that the LLT is not a phenomenon that excludes phase separation. Both phenomena can occur simultaneously when the composition of the system is not right on the critical composition for a pure polyamorphic transition. In this case, it is conceivable that the high-temperature fragile phase separates into two phases. One is strong and the other remains fragile. A slight compositional change does not affect the intrinsic liquid structural change, which is the real origin of the drastic viscosity and fragility change of the liquid. This

7. Chapter: The liquid-liquid transition in Vit.1

is analogous to the first-order order-disorder transition system Cu_3Au where the order-disorder transition and the phase separation occur simultaneously with decreasing temperature when the composition of Cu-Au is slightly off the ratio 3:1. For Vit.1, the volume data obtained by cooling from the high-temperature liquid (Fig. 7.13) are fitted well by a linear function, yielding a constant thermal expansion coefficient, which indicates that the compositional change must be so small (if not zero) that it cannot result in a detectable change in thermal expansion coefficient. Thus, the fragility crossover should not be explained by a demixing but is more likely caused by intrinsic changes in short- and/or medium-range order atomic configurations of the liquid.

According to the above analysis, it is plausible to consider the LLT that involves the intrinsic structural changes of the liquid itself for a reasonable explanation of the anomalies in Vit.1. The hysteresis phenomena pronounced in viscosity [68] (Fig. 7.4), the specific heat capacity peaks (Fig. 7.1), and the changes in structure factor $S(Q)$ (Fig. 7.8 and 7.9) suggest a weak first-order character of the LLT between the two liquids, in which the high temperature liquid needs to be undercooled and the low temperature liquid needs to be overheated to nucleate the respective other liquid. We propose a homogeneous nucleation scenario for the mechanism of the LLT reported on here. On heating, the fragile droplet nucleates homogeneously in the strong liquid matrix at 1100 K. On cooling the reversible transition occurs at ~ 830 K through the homogeneous nucleation of strong liquid droplets in the fragile liquid matrix. Apparently, there is considerable undercooling and overheating involved, where a faster cooling rate may cause a lower structural transition temperature. According to the classic nucleation theory, the homogeneous nucleation rate depends on both the diffusion (viscosity) and the energy barrier for the critical nucleus, $\Delta G^* \propto \gamma_{LL}^3 / \Delta T_c^2$, where $\gamma \propto \Delta S_{LL}$ is the fragile/strong liquid interfacial energy, ΔS_{LL} the entropy difference across the interfaces and ΔT_c is either the critical undercooling ΔT_c^u or overheating ΔT_c^o . In this scenario, if the critical temperature T_c for the first-order LLT ($\Delta G_{LL} = 0$) is assumed to be located approximately in the middle between 830 K and 1100 K at 965 K (with $\Delta T_c^u = \Delta T_c^o = 135$ K), the entropy difference between strong and fragile liquid can be estimated as $\Delta S_{LL} \sim 1 \text{ J g-atom}^{-1} \text{ K}^{-1}$.

A schematic plot of such a first-order LLT is shown in Fig. 7.14. It is at first surprising that large undercooling (overheating) is necessary to overcome this barrier. However, it needs to be emphasized here that Vit.1 exhibits a very sluggish liquid kinetics, which results in both slow nucleation and growth kinetics of the respective other liquid phase even with a rather small barrier for homogeneous nucleation. One fundamental difference compared to a first-order liquid-crystalline transition has to be pointed out. During melting of a crystalline solid the liquid forms spontaneously at internal interfaces, such as grain boundaries and at the surface by heterogeneous nucleation of the melt and virtually

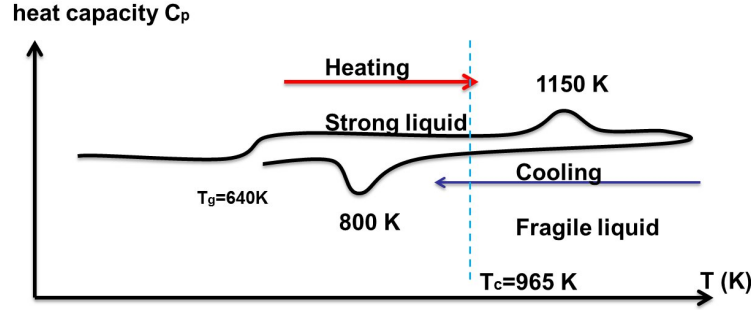


Figure 7.14: A schematic plot of specific heat capacity for the weak first-order liquid-liquid transition in Vit.1.

no overheating is observed. In contrast, in the strong liquid that transforms into the fragile liquid, no interfaces exist and heterogeneous nucleation is improbable, leading to overheating in this case.

In the pressure-temperature ($P - T$) phase diagram, the slope of the liquid-liquid phase equilibrium line between the strong and fragile phases can be determined by the Clausius-Clapeyron relation, $dP/dT = \Delta S_{LL}/\Delta V_{LL}$. As shown in Fig. 7.13, no abrupt density change (i.e., $\Delta V_{LL} \approx 0 \text{ mm}^3$) is observed during the LLT. This suggests an infinite slope of tangent of the coexistence line at $P = 1 \text{ atm}$ (i.e., $dP/dT = \Delta S_{LL}/\Delta V_{LL} \text{ K GPa}^{-1}$) that separates two phases. If the $P - T$ phase diagram of Vit.1 resembles that of water [70], silica [81] and $\text{Al}_2\text{O}_3\text{-Y}_2\text{O}_3$ [77], where the coexistence line terminates at a hypothesized LLCPP with decreasing pressure (sometimes to negative pressure), the LLCPP for Vit.1 is expected below 1 atm or at negative pressure. In contrast, the Jagla model [92] displays an opposite trend of the coexistence line, which terminates at the LLCPP with increasing pressure. Vit.1, if having the same characteristic as the Jagla model, would have a LLCPP at higher pressures above 1 atm. In an experimental detection, a first-order phase transition may not occur at the coexistence line because one phase can remain supercooled or overheated metastable state until a stability limit (spinodal) is approached. In the present case, the hysteresis in the c_p peak and changes of $S(Q)$ suggests that the spinodals for strong and fragile phases lie at temperatures $\sim 1100 \text{ K}$ and $\sim 830 \text{ K}$, respectively.

The enthalpy change for the LLT of Vit.1, around $1.0 \text{ kJ g-atom}^{-1}$, is about 10 % of enthalpy of fusion. Comparing to LLT in Si which has an enthalpy change [159] of 5.5 kJ/g-atom for the Stillinger-Weber potential (or 6 kJ g-atom^{-1} from ab initio calculation), both LLT have the similar fraction of enthalpy of fusion i.e., $\sim 10\text{-}11 \%$. (Enthalpy of fusion of silicon [160]: $\sim 50.6 \text{ kJ g-atom}^{-1}$). Comparing to the liquid-crystal transition, the enthalpy and entropy changes for the LLT are quite small. This leads to the fact that the energy barrier for the LLT is much

smaller than that for the liquid-crystal transition. In such a case, the strong liquid phase as an intermediate state between the fragile liquid and the crystalline phase can stay stably in a considerable temperature range after the LLT rather than crystallize immediately, which is one important reason (another is kinetics) why Vit.1 can be readily deeply undercooled to the region where a strong phase can be observed without the interference of crystallization. The enthalpy difference for the LLT of $\text{Al}_2\text{O}_3\text{-Y}_2\text{O}_3$ is about 35-55% of enthalpy of fusion [77], suggesting that the low-temperature liquid phase is relatively vulnerable to crystallization. That is probably why crystallization was finally not avoidable during cooling even in a containerless environment [77].

7.9 Liquid-liquid transition of Vit.1 in a big picture

Liquid Vit.1 apparently fits into the strong class of Angell's fragility pattern [6] and is comparable to the archetypal strong liquids, SiO_2 and BeF_2 as well as water that are involved in a LLT [161, 81, 162, 72]. Liquid SiO_2 is an extreme case of a strong liquid in the "strong/fragile" pattern [6]. Saika-Voivod et al.[81] revealed a fragile-to-strong transition associated with a specific heat capacity anomaly above the melting temperature T_m by studying static and dynamic properties of liquid silica using numerical simulations. Analogous to SiO_2 , molten BeF_2 studied by Hemmati et al.[72] using the ion dynamics simulations also exhibits a fragile-to-strong crossover as a result of a specific heat capacity maximum above T_m . The experiments available for measuring the specific heat capacity maximum were carried out by Oguni and co-workers [144, 163], using the supercooled water confined within silica gel nanopores to avoid crystallization. A pronounced specific heat capacity peak is observed at about 225 K above T_g and below T_m and is accompanied by a fragile-to-strong transition as revealed in a number of studies [74, 8]. In another case of strong liquid As_2Se_3 , a "semiconductor-metal" transition was reported at high temperatures [164], which are reminiscent of the LLT in SiO_2 and BeF_2 .

The c_p peak in Vit.1 with the strong-fragile crossover exhibits the similar behavior to that of simulated SiO_2 and BeF_2 above T_m and is comparable to water below T_m . For comparison, c_p vs. T_g -scaled temperature for Vit.1, SiO_2 , BeF_2 and nanoconfined water are plotted in Fig. 7.15, also with the c_p of a non-liquid superlattice system $\text{Fe}_{50}\text{Co}_{50}$ which discloses a glass transition (kinetic freezing-in) during the lambda transition [1]. It was demonstrated that the anomalous c_p peak of these substances resembles a system with a lambda transition that is driven into off-critical behavior, for example by increasing the pressure (see Inset in Fig. 7.15). This is reminiscent of the c_p behavior found in the simulations with

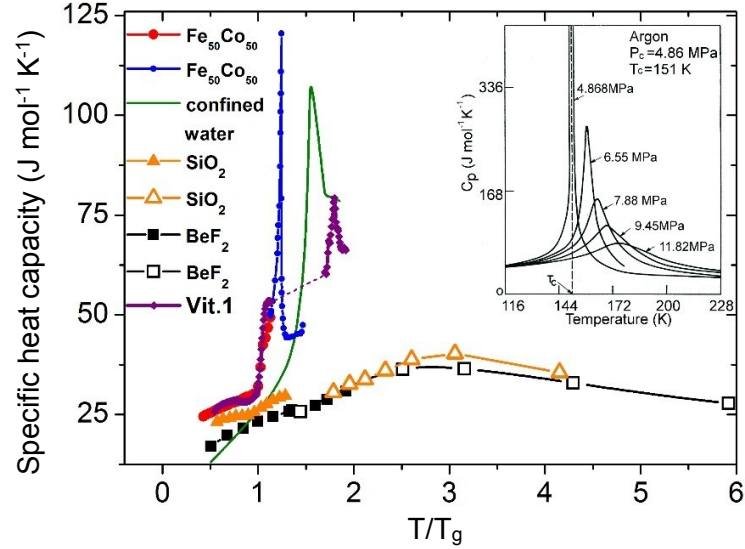


Figure 7.15: Comparison of the specific heat capacity maxima between the liquid Vit.1 and other glass-formers. Solid and open symbols represent experimental and simulation data, respectively (the last data point of SiO_2 is extracted [1] from Fig. 3 of Scheidler et al. [87]). The specific heat capacity values are plotted against the T_g -scaled temperature. For both SiO_2 and BeF_2 , the specific heat capacity maxima with the dynamic crossover are located beyond the normal measurement range, far above T_m , suggesting that the continuous liquid-liquid transitions occur in the stable liquid state at high temperatures. In the case of water, the suggested liquid-liquid transition is in the supercooled liquid regime, where the c_p peak is observed in the water confined by nanopores to avoid crystallization. The liquid-liquid transition of Vit.1 upon heating is located above T_m and has a sharper c_p peak than that of SiO_2 and BeF_2 . These liquid-liquid transitions are considered as off-critical phenomena, compared to the critical phenomenon during the lambda transition in the non-liquid system $\text{Fe}_{50}\text{Co}_{50}$ with a very sharp lambda c_p peak. Inset: the specific heat capacity of argon [1, 165] appears in various forms around its liquid-gas critical point at different pressures (reproduced from Wei et al. [2]).

the Jagla model including a LLCP that provides a mechanism for the LLT [92]. It has been hypothesized that LLT are indeed underlying lambda transitions that separate a strong liquid below the transition temperature from a fragile liquid above it [1]. Consequently, strong liquids are expected to experience such a transition above T_g , which can be observed when the observation window is appropriate and crystallization is avoided. This hypothesis is supported by the study of the present system where the kinetically strong system experiences a first order transition corresponding to isobarically crossing a coexistence line with a possible underlying LLCP.

7.10 Interpretation of liquid structure changes

The sudden change in structure factors observed around 830K during continuous cooling in Fig. 7.8 can be interpreted as the transition from a smaller to a larger length scale state (high- Q_1 state to low- Q_1 state) of Zr-dominant correlations. If we assume that the number and species of atoms on the measured length scale stay constant, a transition from a smaller to larger length scale state implies the change in local atomic packing from a denser to a looser state. To obtain the real space structural information, the reduced total pair distribution functions $G(r)$ are calculated from the structural factor $S(Q)$ by Fourier transform [107]. The n^{th} peak position of $G(r)$ reflects the n^{th} coordination shell distance r_n . No kink is observed around 800 K in the first three coordination shell distances from $G(r)$ during cooling, and the data for the 4^{th} (or $n^{\text{th}} \geq 4^{\text{th}}$) shell include too much noise to make any conclusion. Thus, the length scale of the structural transformation in the supercooled state is likely not less than the 4^{th} shell distance (≥ 1 nm) and can be reflected in by Q_1 of $S(Q)$ in reciprocal space (Fig. 7.8, 7.9), which is demonstrated to be more sensitive to medium/long range correlations [152]. It is hardly a coincidence that the length of the ideal face-centered-cubic (FCC)-like cluster-unit-cell for the medium-range order of Miracle's efficient cluster packing model [38] is calculated to be around 1.0-1.3 nm. The FWHM of $S(Q)$ (Fig. 7.9) is a complementary parameter for the structural characterization to Q_1 (Fig. 7.8). The anomaly of FWHM (slope change 1100-1200 K) upon heating was well reproduced reversely (760-830 K) during cooling, which implies the reversible structural changes. The hysteresis-like feature of the FWHM is reminiscent of the hysteresis in viscosity and heat capacity peaks. For a single-component system, FWHM reflects the degree of ordering of the system where larger width indicates a more disordered state. However, in the multicomponent Vit.1, the anomalies observed at 760-830 K and 1100-1200 K are probably not due to the behavior of the width of a single peak but are more likely due to the shift of multiple underlying peaks, which is consistent with the behavior of Q_1 and suggests that

medium-range order atomic reconfiguration has occurred. Besides, from the $G(r)$ data, we noticed that the thermal behavior for the higher-order coordination shell distances, r_2 , r_3 and r_4 , differ in an opposite way from the 1st shell distance r_1 which notably increases with decreasing temperature. The behavior of r_1 suggests the increasing size of the short-range order clusters with decreasing temperature. A possible scenario is that when the size of the clusters approaches a critical value, this triggers the reconfiguration of the clusters packing on the medium-range order length scale, which might be related to the LLT.

At last, we point out that the structural changes we observe using XRD are mainly contributed by Zr-dominant correlation. There are other atomic correlations that are difficult to be detected due to their much lower X-ray scattering cross-section. It is possible that the structural changes in Fig. 7.8, 7.9 are related to positioning (or chemical) order-disordering processes. The Zr-atoms exchange positions with other atoms. Only the changes associated with Zr-atoms are observed while the position changes associated with other atoms may be not seen. This may be the reason that the liquid local structural changes are not reflected in the macroscopic volume change (Fig. 7.13) in the liquid .

7.11 Polyamorphism in other metallic glass-forming systems

It is realized that polyamorphic transitions are not limited to a few particular glass-forming systems, such as water and silica, but have to be considered to hide in many liquids [143]. Anomalous properties have been observed in a number of liquids, which may hint the existence of a LLT. In the viscosity measurements of bulk metallic glass-forming liquids, Vit.106, Vit.106a, Vit.105 and Vit.101, Evenson et al. [69] observed the strong and fragile discrepancy between low and high temperatures and suggested that there are viscosity hysteresis hidden by crystallization in the supercooled regime of those liquids. Similar phenomena in other systems were also claimed by Zhang et al. [166]. Wessels et al. [167] observed a sudden change in chemical and topological ordering of the supercooled liquid of $\text{Cu}_{46}\text{Zr}_{54}$ samples using in-situ X-ray scattering. This rapid ordering was considered to contribute to the specific heat capacity peak observed during undercooling using ESL. The authors suggest that these observations might be linked to a strong-fragile transition. Sheng et al. [11] and Zeng et al. [78] show evidence of a polyamorphic transition in the Ce-Al metallic glasses, where an abrupt change of the first diffraction peak position Q_1 during decompression is observed with a transformation from a high-density state with shortened Ce-Ce bonds to a low-density state with lengthened Ce-Ce bonds. By ab initio modeling, Sheng et al. [11] attributed this pressure-induced polyamorphism to the f-electron localization

or delocalization, which leads to the length change in the nearest Ce-Ce bonds and accordingly the change in the short-range atomic structure. The authors thus speculate that the polyamorphism in metals is possibly a general feature, when there is an abrupt change in the underlying electronic interactions. This would be a different mechanism of the polyamorphic transition, compared to the network glass-formers, where the polyamorphism is related to an open local environment [168] (e.g., tetrahedral) that may transform into a more densely packed structure. Nevertheless, it is so far still unclear what structural mechanism may underlie the possible polyamorphic transitions of multicomponent bulk metallic glass-forming systems.

7.12 Summary

In summary, we have observed a specific heat capacity peak in the molten liquid of the bulk metallic glass-forming system Vit.1 using calorimetry. With in-situ X-ray diffractions, we have observed the anomalous structural changes upon heating and during undercooling in the liquid. The experimental results suggest that the local structure changes are sufficient to cause a strong-fragile crossover in the dynamics without a detectable macroscopic density anomaly. The thermodynamic, structural and dynamics anomalies suggest that liquid Vit.1, as a typical strong BMG-forming liquid in Angell's fragility scheme, undergoes a weak first-order LLT at temperatures above T_g , which is comparable to the network glass-forming liquids, SiO_2 and BeF_2 as well as water, regardless of distinct atomic bonding. Our findings provide experimental support for the hypothesis [1] that the strong kinetics (low-fragility) of a liquid arises from an underlying lambda LLT above T_g . Thus, we expect to observe LLT also in other strong BMG-forming liquids [69, 166] above their respective T_g , if crystallization is avoided. Our study provides an important approach to experimental explorations of the LLT in metallic glass-forming systems and the LLT correlated properties.

Chapter 8

Summary and conclusions

This thesis addresses the questions on the origin of fragility and the relation between the fragility, thermodynamic properties and the structure of glass-forming systems. In this chapter, the primary experimental results and conclusions are summarized.

8.1 The glass transition and the fragility of order-disorder alloys

The glass transition of $\text{Fe}_{50}\text{Co}_{50}$ and $(\text{FeCo})_{100-x}\text{Al}_x$ solid systems during the ordering/disordering process is studied. The glass transition observed upon DSC upscans is a kinetic unfreezing of the structural order that is arrested at T_g during previous cooling. Below T_g , there is no thermodynamic transition. The fragility of $\text{Fe}_{50}\text{Co}_{50}$ near T_g is determined to be extremely strong ($m \approx 16$) using DSC scans. At a high temperature above T_g , the $\text{Fe}_{50}\text{Co}_{50}$ system undergoes an order-disorder (λ) transition with a sharp λ specific heat capacity peak. The critical point of the transition is located at 1003 K and ambient pressure, at which the ordered phase and the disordered phase become indistinguishable. At the critical point, the correlation length of the order parameter fluctuation is diverging.

The thermodynamic and kinetic behavior of $\text{Fe}_{50}\text{Co}_{50}$ mimics the liquid with a critical point simulated using the Jagla model. The liquid of the Jagla model is strong near T_g . The glass transition occurs at the low-temperature side of a λ -shape specific heat capacity peak. This peak is related to a liquid-liquid critical point. Compared with the simulated liquid, the glass transition and the order-disorder transition of $\text{Fe}_{50}\text{Co}_{50}$ appear to exhibit the parallel behavior in the solid state. The glass transition of $\text{Fe}_{50}\text{Co}_{50}$ is characterized by a static correlation length that decreases when approaching the transition temperature

T_g from above.

In light of the phenomenological analogy between the kinetically strong $\text{Fe}_{50}\text{Co}_{50}$ and the liquids of simulations, a unified picture of the behavior of strong and fragile liquids is proposed. Strong liquids differ from fragile liquids by occupying opposite sides of an underlying order-disorder transition, which can be continuous, critical or weakly first order. Therefore, strong liquids are expected to undergo a liquid phase change at a high temperature above the glass transition temperature, or even above the melting point, at appropriate pressures. Accordingly, the anomalous specific heat capacity maximum in strong liquids SiO_2 and BeF_2 is attributed to a continuous smeared out order-disorder transition, as the observation is carried out in the supercritical region where an extension of the coexistence line beyond the liquid-liquid critical point is crossed. The smeared out specific heat capacity peak of liquid SiO_2 and BeF_2 is reminiscent of the specific heat capacity of argon near its liquid-gas critical point. When the system is in the supercritical region, pressure may smear out the specific heat capacity peak. For fragile liquids, the system is frozen-in at the glass transition during cooling and falls out of equilibrium before it accesses the deeply undercooled region, where a thermodynamic (first-order) transition might occur near the Kauzmann temperature. Since the thermodynamic transition is hidden below T_g , it is difficult to be observed in experiments, although simulations show evidence of such a transition in very fragile liquids. This study sheds light on the relation between the glass transition and its related underlying thermodynamic transition and provides insight into the origin of liquid fragility.

Besides the simple binary $\text{Fe}_{50}\text{Co}_{50}$ system, the thermodynamics and kinetics of the ternary $(\text{FeCo})_{100-x}\text{Al}_x$ alloy are studied. Adding aluminum as the 3rd component, the specific heat capacity of the ternary compositions changes systematically with increasing aluminum concentrations. The glass transition exhibits a weakened specific heat capacity jump at T_g . The magnitude and the slope of the specific heat capacity are smaller and the T_g is shifted to a higher temperature in $(\text{FeCo})_{100-x}\text{Al}_x$ with more aluminum content. Moreover, the order-disorder transition is found to occur at a higher temperature, which is more separated from T_g with a higher aluminum concentration. However, the specific heat capacity peak of the order-disorder transition is smeared out. These are explained by the cooperative phenomenon of the order-disorder transition undermined by a small amount of aluminum atoms. The cooperativity of the order-disorder transition in the ternary $(\text{FeCo})_{100-x}\text{Al}_x$ alloys presents a phenomenological analogy to the cooperative liquid phase transition in strong glass-forming liquids. The fragility of the ternary system $(\text{FeCo})_{100-x}\text{Al}_x$ is determined by DSC down- and up-scans throughout the glass transition region. All of the studied compositions exhibit kinetically strong behavior with a fragility parameter m of around 16. This shows that aluminum additions do not have a significant influence on the

kinetic fragility. It appears that the specific heat capacity jump as well as the cooperativity do not directly correlate with the kinetic fragility of the studied systems.

8.2 The relation between the fragility, thermodynamics and the structure of a bulk metallic glass-forming liquid

The multicomponent alloy $\text{Zr}_{41.2}\text{Ti}_{13.8}\text{Cu}_{12.5}\text{Ni}_{10}\text{Be}_{22.5}$ (Vit.1) is a good bulk metallic glass-former with sluggish kinetics. The viscosity of liquid Vit.1 exhibits strong liquid behavior near its T_g and appears fragile far above the liquidus temperature at high temperature. There appears to be two dynamic states, a high-temperature fragile liquid state and a low-temperature strong liquid state. During the strong-to-fragile crossover, the viscosity changes anomalously by about 2 orders of magnitude upon heating above the liquidus temperature. The kinetic strong-fragile transition resembles the dynamic crossover in water and network glass-formers.

To study the thermodynamic and structural origin of the strong-fragile crossover, high-temperature calorimetric experiments are carried out and the in-situ synchrotron X-ray scattering in contactless environment using an electrostatic levitator (ESL) is performed. A specific heat capacity peak is observed on heating between 1100 K and 1200 K, above the reported liquidus temperature 1026 K. The heat gain of the specific heat capacity peak is around 1 kJ g-atom^{-1} , about 10% of the enthalpy of fusion. The in-situ X-ray diffraction (XRD) results and the volume measurement indicate that the specific heat capacity peak occurs in the liquid state and cannot be explained by melting of crystals.

Synchrotron X-ray scattering combined with ESL allows us to study the structural changes of liquids in the deeply supercooled regime due to the absence of heterogeneous nucleation sites. The total structure factors $S(Q)$ are extracted from the diffracted intensity data. A sudden change in the temperature dependence of the first peak position of $S(Q)$ is observed at around 830 K. The sudden shift suggests a medium-range-order change in the Zr-dominant interatomic correlations in real space. Moreover, an abrupt change of the FWHM during cooling is observed around 760-830 K. This is the same feature as the sudden change observed in $S(Q)$. On reheating, after the system returns to the liquid state at high temperature ($\sim 1100 \text{ K}$), the data points exhibit a clear change of slope at around 1150 K, which corresponds to the temperature range where the specific heat capacity peak is observed in the calorimeter. The changes on cooling and reheating appear as a reversible phenomenon and the data that reflect structural changes display a form of three quarters of a hysteresis when the missing data

gap is extrapolated linearly from the lower temperature data.

Furthermore, the volume measurements using ESL show no anomalous change at the temperature range of 750-830 K and 1100-1200 K. This indicates that the entropy fluctuation is the dominant term in the liquid-liquid transition instead of a density fluctuation in terms of the Clausius-Clapeyron equation.

These experimental findings suggest that there is a weak first-order liquid-liquid transition in the system. The possibility of a liquid-liquid critical point in this system is discussed. There are indications that such a transition may be a general behavior of Zr-based bulk metallic glass-forming liquids. This work presents a novel approach to explore the polyamorphic transition in metallic glass-forming liquids in the deeply undercooled state. Searching for a unified picture for polyamorphism in different systems will be the next challenge.

Copyright permissions

Copyright permissions in this thesis for reused published materials.

Figure	License Number
2.1	3211920232105
2.2-2.4	3211921001828
2.5	3211921436638
2.6	3211930069418
2.7	3211930302287
2.8	*
2.11	3211951079377
2.12	3211951275053
2.13	3211960582347
2.14	3212090973189
2.15	3212091151071
2.16	3212091273384
2.18	3212100698109
2.19	3212100199869
2.21	3212100698109
2.22	3212110158893
4.7	3212110158893
4.9	3212110299329
7.4-7.5	3212380050239
Part of text in Chap. 7	3212371464456

*Reprinted (adapted) with permission from DOI: 10.1021/cr000689q. Copyright (2002) American Chemical Society.

Molar mass of substances

Name	Composition (atomic %)	Atomic weight (g g-atom ⁻¹)*
Vit.1	Zr _{41.2} Ti _{13.8} Cu _{12.5} Ni ₁₀ Be _{22.5}	60.032
Vit.1b	Zr ₄₄ Ti ₁₁ Ni ₁₀ Cu ₁₀ Be ₂₅	59.881
Vit.101	Cu ₄₇ Ti ₃₄ Zr ₁₁ Ni ₈	60.872
Vit.105	Zr _{52.5} Cu _{17.9} Ni _{14.6} Al ₁₀ Ti ₅	72.928
Vit.106a	Zr _{58.5} Cu _{15.6} Ni _{12.8} Al _{10.3} Nb _{2.8}	76.172
Vit.106	Zr ₅₇ Cu _{15.4} Ni _{12.6} Al ₁₀ Nb ₅	76.522
Vit.4	Zr _{46.75} Ti _{8.25} Cu _{7.5} Ni ₁₀ Be _{27.5}	59.710
AMZ4	Zr _{59.3} Cu _{28.8} Al _{10.4} Nb _{1.5}	76.597
Au ₄₉ -BMG	Au ₄₉ Cu _{26.9} Si _{16.3} Ag _{5.5} Pd _{2.3}	126.566
Pd ₄₃ -BMG	Pd ₄₃ Cu ₂₇ Ni ₁₀ P ₂₀	74.982
	B ₂ O ₃	13.924
	SiO ₂	20.028
	GeO ₂	34.879
	Fe ₅₀ Co ₅₀	57.389
	(FeCo) _{99.1} Al _{0.9}	57.115
	(FeCo) _{97.3} Al _{2.7}	56.568
	(FeCo) _{96.3} Al _{3.7}	56.264
	(FeCo) _{93.7} Al _{6.4}	55.443

*The atomic weight is given in the unit of gram per mole of atoms (g g-atom⁻¹).

Abbreviations

BMG: bulk metallic glass
DSC: differential scanning calorimeter
DTA: differential thermal analyzer
ESL: electrostatic levitator
FWHM: full width at half maximum
HDL: high-density liquid
HDA: high-density amorphous
LDL: low-density liquid
LDA: low-density amorphous
LLT: liquid-liquid transition
LLCP: liquid-liquid critical point
PDF: pair distribution function
SANS: small angle neutron scattering
SAXS: small angle X-ray scattering
TTT: time-temperature-transformation
VFT: Vogel-Fulcher-Tammann
WAXS: wide angle X-ray scattering
XRD: X-ray diffraction

Bibliography

- [1] Wei, S., Gallino, I., Busch, R. and Angell, A. *Nature Phys.*, **7**, pp. 178–182 (2011).
- [2] Wei, S., Yang, F., Bednarcik, J., Kaban, I., Shuleshova, O., Meyer, A. and Busch, R. *Nat. Commun.*, **4** (2013).
- [3] Angell, C. A. *Chem. Rev.*, **102**, pp. 2627–2650 (2002).
- [4] Debenedetti, P. G. and Stillinger, F. H. *Nature*, **410**, pp. 259–267 (2001).
- [5] Angell, C. A. *J. Non-Cryst. Solids*, **131**, pp. 13–31 (1991).
- [6] Angell, C. A. *Science*, **267**, pp. 1924–1935 (1995).
- [7] Angell, C. A. *J. Non-Cryst. Solids*, **354**, pp. 4703–4712 (2008).
- [8] Ito, K., Moynihan, C. T. and Angell, C. A. *Nature*, **398**, pp. 492–495 (1999).
- [9] Mishima, O., Calvert, L. D. and Whalley, E. *Nature*, **314**, pp. 76–78 (1985).
- [10] Mishima, O. and Stanley, H. E. *Nature*, **396**, p. 329 (1998).
- [11] Sheng, H. W., Liu, H. Z., Cheng, Y. Q., Wen, J., Lee, P. L., Luo, W. K., Shastri, S. D. and Ma, E. *Nature Mater.*, **6**, pp. 192–197 (2007).
- [12] Klement, W., Willens, R. and Duwez, P. *Nature*, **187**, pp. 869–870 (1960).
- [13] Wang, W.-H., Dong, C. and Shek, C. *Mater. Sci. Eng. R*, **44**, pp. 45–89 (2004).
- [14] Greer, A. L. *Science*, **267**, pp. 1947–1953 (1995).
- [15] Busch, R., Kim, Y. J. and Johnson, W. L. *J. Appl. Phys.*, **77**, pp. 4039–4043 (1995).

BIBLIOGRAPHY

- [16] Busch, R., Schroers, J. and Wang, W. H. *MRS Bull.*, **32**, pp. 620–623 (2007).
- [17] Lin, X. and Johnson, W. *J. Appl. Phys.*, **78**, pp. 6514–6519 (1995).
- [18] Schroers, J. and Johnson, W. L. *Phys. Rev. Lett.*, **93**, p. 255506 (2004).
- [19] Ashby, M. and Greer, A. *Scr. Mater.*, **54**, pp. 321 – 326 (2006).
- [20] Greer, A. L. and Ma, E. *MRS Bull.*, **32**, pp. 611–619 (2007).
- [21] Johnson, W. *JOM*, **54**, pp. 40–43 (2002).
- [22] Schroers, J. *Adv. Mater.*, **22**, pp. 1566–1597 (2010).
- [23] Liu, Y. H., Wang, G., Wang, R. J., Pan, M. X., Wang, W. H. et al. *Science*, **315**, pp. 1385–1388 (2007).
- [24] Das, J., Tang, M. B., Kim, K. B., Theissmann, R., Baier, F., Wang, W. H. and Eckert, J. *Phys. Rev. Lett.*, **94**, p. 205501 (2005).
- [25] Schuh, C. A., Hufnagel, T. C. and Ramamurty, U. *Acta Mater.*, **55**, pp. 4067–4109 (2007).
- [26] Argon, A. *Acta Metall. Mater.*, **27**, pp. 47–58 (1979).
- [27] Hays, C., Kim, C. and Johnson, W. *Phys. Rev. Lett.*, **84**, p. 2901 (2000).
- [28] Spaepen, F. *Acta Metall. Mater.*, **25**, pp. 407–415 (1977).
- [29] Yavari, A. R., Lewandowski, J. J. and Eckert, J. *MRS Bull.*, **32**, pp. 635–638 (2007).
- [30] Conner, R., Li, Y., Nix, W. and Johnson, W. *Acta Mater.*, **52**, pp. 2429–2434 (2004).
- [31] Li, Y., Poon, S. J., Shiflet, G. J., Xu, J., Kim, D. H. and Löffler, J. F. *MRS Bull.*, **32**, pp. 624–628 (2007).
- [32] Hofmann, D. C., Suh, J.-Y., Wiest, A., Duan, G., Lind, M.-L., Demetriou, M. D. and Johnson, W. L. *Nature*, **451**, pp. 1085–1089 (2008).
- [33] Busch, R., Bakke, E. and Johnson, W. L. *Mater. Sci. Forum*, **235-238**, pp. 327–335 (1997).
- [34] Schroers, J., Masuhr, A., Johnson, W. L. and Busch, R. *Phys. Rev. B*, **60**, p. 11855 (1999).

- [35] Vogel, H. *Phys. Z.*, **22**, p. 645 (1921).
- [36] Tammann, G. and Hesse, W. *Z. Anorg. Allgem. Chem.*, **156**, p. 245 (1926).
- [37] Cheng, Y. and Ma, E. *Prog. Mater. Sci.*, **56**, pp. 379 – 473 (2011).
- [38] Miracle, D. B. *Nature Mater.*, **3**, pp. 697–702 (2004).
- [39] Bernal, J. D. *Proc. R. Soc. Lond. A*, **280**, p. 299322 (1964).
- [40] Sheng, H. W., Luo, W. K., Alamgir, F. M., Bai, J. M. and Ma, E. *Nature*, **439**, pp. 419–425 (2006).
- [41] Miracle, D. *Acta Mater.*, **54**, pp. 4317–4336 (2006).
- [42] Cheng, Y. Q., Ma, E. and Sheng, H. W. *Appl. Phys. Lett.*, **93**, pp. 111913–3 (2008).
- [43] Cheng, Y. Q. and Ma, E. *Prog. Mater. Sci.*, **56**, pp. 379–473 (2011).
- [44] Hodge, I. M. *J. Non-Cryst. Solids*, **169**, pp. 211–266 (1994).
- [45] Moynihan, C. T., Easteal, A. J., BOLT, M. A. and Tucker, J. *Journal of the American Ceramic Society*, **59**, pp. 12–16 (1976).
- [46] Stillinger, F. H. *J. Chem. Phys.*, **88**, pp. 7818–7825 (1988).
- [47] Kauzmann, W. *Chem. Rev.*, **43**, pp. 219–256 (1948).
- [48] Angell, C. A. *J. Res. Natl. Inst. Stand. Technol.*, **102**, pp. 171–185 (1997).
- [49] Adam, G. and Gibbs, J. H. *J. Chem. Phys.*, **43**, pp. 139–146 (1965).
- [50] Goldstein, M. *J. Chem. Phys.*, **51**, p. 3728 (1969).
- [51] Angell, C. A. and Borick, S. *J. Non-Cryst. Solids*, **307**, pp. 393–406 (2002).
- [52] Goldstein, M. *J. Chem. Phys.*, **64**, pp. 4767–4774 (1976).
- [53] Martinez, L. M. and Angell, C. A. *Nature*, **410**, pp. 663–667 (2001).
- [54] Bauer, T., Köhler, M., Lunkenheimer, P., Loidl, A. and Angell, C. *J. Chem. Phys.*, **133**, p. 144509 (2010).
- [55] Brand, R., Lunkenheimer, P. and Loidl, A. *J. Chem. Phys.*, **116**, pp. 10386–10401 (2002).
- [56] Angell, C. and Hemmati, M. *AIP Conf. Proc.*, **1518**, pp. 9–17 (2013).

BIBLIOGRAPHY

- [57] Angell, C. A. et al. *Pure Appl. Chem.*, **63**, pp. 1387–1392 (1991).
- [58] Xia, X. and Wolynes, P. G. *Proc. Natl. Acad. Sci.*, **97**, pp. 2990–2994 (2000).
- [59] Huang, D. and McKenna, G. B. *J. Chem. Phys.*, **114**, pp. 5621–5630 (2001).
- [60] Wang, L.-M., Angell, C. A. and Richert, R. *J. Chem. Phys.*, **125**, p. 074505 (2006).
- [61] Angell, C. A. and Rao, K. J. *J. Chem. Phys.*, **57**, p. 470 (1972).
- [62] Angell, C. A., Richards, B. E. and Velikov, V. *J. Phys.: Condens. Matter*, **75** (1999).
- [63] Matyushov, D. V. and Angell, C. A. *J. Chem. Phys.*, **126**, p. 94501 (2007).
- [64] Angell, C. A., Moyniha, C. T. and Moynihan, C. T. *Metall. Mater. Trans. B*, **31**, pp. 587–596 (2000).
- [65] Sastry, S. *Nature*, **409**, pp. 164–167 (2001).
- [66] Angell, A. *Nature*, **393** (1998).
- [67] Angell, C. A. *Science*, **319**, pp. 582–587 (2008).
- [68] Way, C., Wadhwa, P. and Busch, R. *Acta Mater.*, **55**, pp. 2977–2983 (2007).
- [69] Evenson, Z., Schmitt, T., Nicola, M., Gallino, I. and Busch, R. *Acta Mater.*, **60**, pp. 4712–4719 (2012).
- [70] Xu, L., Kumar, P., Buldyrev, S. V., Chen, S.-H., Poole, P. H., Sciortino, F. and Stanley, H. E. *Proc. Natl. Acad. Sci.*, **102**, pp. 16558–16562 (2005).
- [71] Saika-Voivod, I., Poole, P. H. and Sciortino, F. *Nature*, **412**, pp. 514–517 (2001).
- [72] Hemmati, M., Moynihan, C. T. and Angell, C. A. *J. Chem. Phys.*, **115**, pp. 6663–6671 (2001).
- [73] Angell, C. A. *J. Phys. Chem.*, **97**, pp. 6339–6341 (1993).
- [74] Chen, S. H., Zhang, Y., Lagi, M., Chong, S. H., Baglioni, P. and Mallamace, F. *J. Phys. Condens. Matter*, **21**, p. 504102 (2009).
- [75] Tanaka, H., Kurita, R. and Mataka, H. *Phys. Rev. Lett.*, **92**, p. 025701 (2004).

BIBLIOGRAPHY

- [76] Aasland, S. and McMillan, P. F. *Nature*, **369**, pp. 633–636 (1994).
- [77] Greaves, G. N., Wilding, M. C., Fearn, S., Langstaff, D., Kargl, F., Cox, S., Van, Q. V., Majrus, O., Benmore, C. J., Weber, R., Martin, C. M. and Henet, L. *Science*, **322**, pp. 566–570 (2008).
- [78] Zeng, Q.-s., Ding, Y., Mao, W. L., Yang, W., Sinogeikin, S. V., Shu, J., Mao, H.-k. and Jiang, J. *Phys. Rev. Lett.*, **104**, p. 105702 (2010).
- [79] Katayama, Y., Mizutani, T., Utsumi, W., Shimomura, O., Yamakata, M. and Funakoshi, K.-i. *Nature*, **403**, pp. 170–173 (2000).
- [80] Sastry, S. and Austen Angell, C. *Nature Mater.*, **2**, pp. 739–743 (2003).
- [81] Saika-Voivod, I., Sciortino, F. and Poole, P. H. *Phys. Rev. E*, **63**, p. 011202 (2000).
- [82] Bhat, M. H., Molinero, V., Soignard, E., Solomon, V. C., Sastry, S., Yarger, J. L. and Angell, C. A. *Nature*, **448**, pp. 787–790 (2007).
- [83] Poole, P. H., Sciortino, F., Essmann, U. and Stanley, H. E. *Nature*, **360**, pp. 324–328 (1992).
- [84] Liu, L., Chen, S.-H., Faraone, A., Yen, C.-W. and Mou, C.-Y. *Phys. Rev. Lett.*, **95**, p. 117802 (2005).
- [85] Woodcock, L., Angell, C. and Cheeseman, P. *J. Chem. Phys.*, **65**, p. 1565 (1976).
- [86] Van Beest, B., Kramer, G. and Van Santen, R. *Phys. Rev. Lett.*, **64**, p. 1955 (1990).
- [87] Scheidler, P., Kob, W., Latz, A., Horbach, J. and Binder, K. *Phys. Rev. B*, **63**, p. 104204 (2001).
- [88] McMillan, P. F., Wilson, M., Daisenberger, D. and Machon, D. *Nature Mater.*, **4**, pp. 680–684 (2005).
- [89] McMillan, P. F., Wilson, M., Wilding, M. C., Daisenberger, D., Mezouar, M. and Greaves, G. N. *J. Phys.: Condens. Matter*, **19**, p. 415101 (2007).
- [90] Rapoport, E. *J. Chem. Phys.*, **46**, p. 2891 (1967).
- [91] McMillan, P. F. *J. Mater. Chem.*, **14**, pp. 1506–1512 (2004).

- [92] Xu, L., Buldyrev, S. V., Giovambattista, N., Angell, C. A. and Stanley, H. E. *J. Chem. Phys.*, **130**, p. 054505 (2009).
- [93] Luo, J., Xu, L., Angell, C. A., Stanley, H. E. and Buldyrev, S. V. <http://arxiv.org/abs/1204.6107>, p. 133 (2012).
- [94] Haines, P. J. *Principles of Thermal Analysis and Calorimetry*. The Royal Society of Chemistry (2002).
- [95] Gray, A. P. *A simple generalized theory for the analysis of dynamic thermal measurement*. Springer (1995).
- [96] Busch, R., Liu, W. and Johnson, W. L. *J. Appl. Phys.*, **83**, pp. 4134–4141 (1998).
- [97] Evenson, Z., Gallino, I. and Busch, R. *J. Appl. Phys.*, **107**, p. 123529 (2010).
- [98] Wang, L.-M., Velikov, V. and Angell, C. A. *J. Chem. Phys.*, **117**, pp. 10184–10192 (2002).
- [99] Busch, R. and Johnson, W. L. *Appl. Phys. Lett.*, **72**, pp. 2695–2697 (1998).
- [100] Egami, T. and Billinge, S. J. L. *Underneath the Bragg Peaks, Structural Analysis of Complex Materials*. Pergamon Materials Series. Pergamon, Oxford (2003).
- [101] Cheng, Y. Q., Ma, E. and Sheng, H. W. *Phys. Rev. Lett.*, **102**, p. 245501 (2009).
- [102] Reimers, W., Pyzalla, A. R., Schreyer, A. and Clemens, H. *Neutrons and synchrotron radiation in engineering materials science*, vol. 42. Wiley Online Library (2008).
- [103] Flegel, I. and Jena, T. *Deutsches Elektronen-Synchrotron DESY A Research Centre of the Helmholtz Association* (2007).
- [104] Kordel, T., Holland-Moritz, D., Yang, F., Peters, J., Unruh, T., Hansen, T. and Meyer, A. *Phys. Rev. B*, **83**, p. 104205 (2011).
- [105] Hammersley, A., Svensson, S., Hanfland, M., Fitch, A. and Husermann, D. *High Pressure Res.*, **14**, pp. 235–248 (1996).
- [106] Hammersley, A. *ESRF internal Report FIT2D V9.129 Reference Manual V3.1*. ESRF (1998).

- [107] Qiu, X., Thompson, J. W. and Billinge, S. J. L. *J. Appl. Crystallogr.*, **37**, p. 678 (2004).
- [108] Ruland, W. *Br. J. Appl. Phys.*, **15**, p. 1301 (1964).
- [109] Thijsse, B. J. *J. Appl. Crystallogr.*, **17**, pp. 61–76 (1984).
- [110] Angell, C. *J. Phys. Cond. Matter*, **12**, p. 6463 (2000).
- [111] Mattsson, J., Wyss, H. M., Fernandez-Nieves, A., Miyazaki, K., Hu, Z., Reichman, D. R. and Weitz, D. A. *Nature*, **462**, pp. 83–86 (2009).
- [112] Berthier, L., Biroli, G., Bouchaud, J.-P., Cipelletti, L., El Masri, D., L'Hôte, D., Ladieu, F. and Pierno, M. *Science*, **310**, pp. 1797–1800 (2005).
- [113] Sausset, F. and Tarjus, G. *Phys. Rev. Lett.*, **104**, p. 065701 (2010).
- [114] Kaya, S. and Sato, H. *Proc. Phys. Math. Soc. Jap.*, **25**, pp. 261–273 (1943).
- [115] Nix, F. C. and Shockley, W. *Rev. Mod. Phys.*, **10**, p. 1 (1938).
- [116] Gschwend, K., Sato, H. and Kikuchi, R. *J. Chem. Phys.*, **69**, pp. 5006–5019 (1978).
- [117] Gschwend, K., Sato, H., Kikuchi, R., Iwasaki, H. and Maniwa, H. *J. Chem. Phys.*, **71**, pp. 2844–2852 (1979).
- [118] Busch, R., Bakke, E. and Johnson, W. L. *Appl. Phys. Lett.*, **68**, pp. 2945–2947 (1996).
- [119] Kirkwood, J. G. *J. Chem. Phys.*, **6**, pp. 70–75 (1938).
- [120] Girifalco, L. A. *Statistical Mechanics of Solids*. Oxford University Press US (2000).
- [121] Bragg, W. and Williams, E. *Proc. Roy. Soc. London*, **145A**, p. 699 (1934).
- [122] Xu, L., Buldyrev, S. V., Angell, C. A. and Stanley, H. E. *Phys. Rev. E*, **74**, p. 031108 (2006).
- [123] Kumar, P., Buldyrev, S., Becker, S., Poole, P., Starr, F. W. and Stanley, H. *Proc. Natl Acad. Sci.*, **104**, pp. 9575–9579 (2007).
- [124] Tanaka, H., Kawasaki, T., Shintani, H. and Watanabe, K. *Nature Mater.*, **9**, pp. 324–331 (2010).

- [125] Girifalco, L. A. *Statistical Mechanics of Solids*. Oxford University Press US (2000).
- [126] Zernike, F. *Physica*, **7**, pp. 565–585 (1940).
- [127] Domb, C. *Adv. Phys.*, **9**, pp. 245–361 (1960).
- [128] Bohmer, R., Ngai, K. L., Angell, C. A. and Plazek, D. J. *J. Chem. Phys.*, **99**, pp. 4201–4209 (1993).
- [129] Moynihan, C. T. *J. Am. Ceram. Soc.*, **76**, pp. 1081–1087 (1993).
- [130] Fulcher, G. S. *J. Am. Chem. Soc.*, **8**, p. 339 (1923).
- [131] Wang, L.-M. *J. Phys. Chem. B*, **113**, pp. 5168–5171 (2009).
- [132] Mauro, J. C. and Loucks, R. J. *Phys. Rev. E*, **78**, p. 021502 (2008).
- [133] Mauro, J. C. and Loucks, R. J. *Phys. Rev. B*, **76**, p. 174202 (2007).
- [134] Fan, G. J., Fecht, H. J. and Lavernia, E. J. *Appl. Phys. Lett.*, **84**, pp. 487–489 (2004).
- [135] Evenson and et al. *unpublished* (2013).
- [136] Busch, R., Masuhr, A. and Johnson, W. L. *Mater. Sci. Eng. A*, **304**, pp. 97–102 (2001).
- [137] Evenson, Z. and Busch, R. *Acta Mater.*, **59**, pp. 4404–4415 (2011).
- [138] Waniuk, T. A., Busch, R., Masuhr, A. and Johnson, W. L. *Acta Mater.*, **46**, pp. 5229–5236 (1998).
- [139] Mukherjee, S., Schroers, J., Zhou, Z., Johnson, W. L. and Rhim, W. K. *Acta Mater.*, **52**, pp. 3689–3695 (2004).
- [140] Zheng, Q., Potuzak, M., Mauro, J. C., Smedskjaer, M. M., Youngman, R. E. and Yue, Y. *J. Non-Cryst. Solids*, **358**, pp. 993–1002 (2012).
- [141] Schroers, J. *Acta Mater.*, **56**, pp. 471–478 (2008).
- [142] Gallino, I., Schroers, J. and Busch, R. *J. Appl. Phys.*, **108**, pp. 063501–8 (2010).
- [143] Angell, C. A. *MRS Bull.*, **33**, pp. 544–555 (2008).

BIBLIOGRAPHY

- [144] Maruyama, S., Wakabayashi, K. and Oguni, M. *AIP Conf. Proc.*, **708**, pp. 675–676 (2004).
- [145] Ohsaka, K., Chung, S. K., Rhim, W. K., Peker, A., Scruggs, D. and Johnson, W. L. *Appl. Phys. Lett.*, **70**, pp. 726–728 (1997).
- [146] Masuhr, A., Busch, R. and Johnson, W. L. *J. Non-Cryst. Solids*, **250-252**, pp. 566–571 (1999).
- [147] Thomas, D. G. *J. Coll. Sci. Imp. U. Tok.*, **20**, pp. 267–277 (1965).
- [148] Frankel, N. A. and Acrivos, A. *Chem. Eng. Sci.*, **22**, pp. 847–853 (1967).
- [149] Glasstone, S., Laidler, K. and Eyring, H. *The theory of rate processes: the kinetics of chemical reactions, viscosity, diffusion and electrochemical phenomena*. McGraw-Hill Book Company, inc., New York; London (1941).
- [150] Kubaschewski, O., Alcock, C. B. and Spencer, P. J. *Materials Thermochemistry*. Pergamon, New York (1993).
- [151] Wei, S., Yang, F., Bednarcik, J., Kaban, I., Meyer, A. and Busch, R. **1518**, p. 260 (2013).
- [152] Bednarcik, J., Michalik, S., Sikorski, M., Curfs, C., Wang, X. D., Jiang, J. Z. and Franz, H. *J. Phys. Condens. Matter*, **23**, p. 254204 (2011).
- [153] Li, J. J. Z., Rhim, W. K., Kim, C. P., Samwer, K. and Johnson, W. L. *Acta Mater.*, **59**, pp. 2166–2171 (2011).
- [154] Yavari, A. R., Moulec, A. L., Inoue, A., Nishiyama, N., Lupu, N., Matsubara, E., Botta, W. J., Vaughan, G., Michiel, M. D. and Kvik, A. *Acta Mater.*, **53**, pp. 1611–1619 (2005).
- [155] Mattern, N., Stoica, M., Vaughan, G. and Eckert, J. *Acta Mater.*, **60**, pp. 517–524 (2012).
- [156] Loffler, J., Thiyagarajan, P. and Johnson, W. *J. Appl. Crystallogr.*, **33**, pp. 500–503 (2000).
- [157] Martin, I., Ohkubo, T., Ohnuma, M., Deconihout, B. and Hono, K. *Acta Mater.*, **52**, pp. 4427–4435 (2004).
- [158] Loffler, J. F. and Johnson, W. L. *Appl. Phys. Lett.*, **76**, pp. 3394–3396 (2000).
- [159] Jakse, N. and Pasturel, A. *Phys. Rev. Lett.*, **99**, p. 205702 (2007).

BIBLIOGRAPHY

- [160] Hull, R. *Properties of crystalline silicon*. EMIS datareviews series, no.20. INSPEC, London (1999).
- [161] Poole, P. H., Hemmati, M. and Angell, C. A. *Phys. Rev. Lett.*, **79**, p. 2281 (1997).
- [162] Stanley, H. E. e. a. *J. Phys. Condens. Matter*, **22**, p. 284101 (2010).
- [163] Oguni, M., Maruyama, S., Wakabayashi, K. and Nagoe, A. *Chem-asian J*, **2**, pp. 514–520 (2007).
- [164] Shinya, H. and Kozaburo, T. *J. Phys. Condens. Matter*, **16**, p. R1465 (2004).
- [165] Kim, K. Y. *Calorimetric Studies on Argon and Hexafluoro Ethane and a Generalized Correlation of Maxima in Isobaric Heat Capacity*. Tech. rep., Michigan University, Department of Chemical Engineering, <http://deepblue.lib.umich.edu/handle/2027.42/6003>. (1974).
- [166] Zhang, C., Hu, L., Yue, Y. and Mauro, J. C. *J. Chem. Phys.*, **133**, pp. 014508–7 (2010).
- [167] Wessels, V., Gangopadhyay, A. K., Sahu, K. K., Hyers, R. W., Canepari, S. M., Rogers, J. R., Kramer, M. J., Goldman, A. I., Robinson, D., Lee, J. W., Morris, J. R. and Kelton, K. F. *Phys. Rev. B*, **83**, p. 094116 (2011).
- [168] Stanley, H. E., Kumar, P., Franzese, G., Xu, L., Yan, Z., Mazza, M. G., Buldyrev, S. V., Chen, S. H. and Mallamace, F. *Eur. Phys. J-Spec. Top.*, **161**, pp. 1–17 (2008).